Polymers confined in lyotropic lamellar mesophases

Laure Herrmann

Université de Strasbourg

École Doctorale de Physique et Chimie-Physique

Institut Charles Sadron

Thèse présentée par

Laure HERRMANN

soutenue le 20 septembre 2013

pour obtenir le grade de Docteur de l'Université de Strasbourg

Discipline : Physique

Polymères confinés dans des mésophases lamellaires lyotropes

Directeur de thèse

M. KÉKICHEFF Patrick	Directeur de Recherches, Institut Charles Sadron

Rapporteurs

M. LIGOURE Christian	Professeur, Laboratoire Charles Coulomb
M. FREYSSINGEAS Eric	Maître de Conférences, École Normale Supérieure de Lyon

Président du Jury

M. JOHNER Albert	Directeur de Recherches, Institut Charles Sadron

Polymers confined in lyotropic lamellar mesophases

Laure Herrmann

Supervisor: Patrick Kékicheff

Acknowledgements

Je tiens à remercier Eric Freyssingeas et Christian Ligoure, qui m'ont fait l'honneur d'être membres de mon jury et qui ont accepté d'être les rapporteurs de ce travail. Vos remarques, critiques et suggestions m'ont permis d'améliorer ce manuscrit.

Je remercie tout particulièrement Patrick Kékicheff mon directeur de thèse. Grâce à toi Patrick j'ai pu travailler dans d'excellentes conditions au laboratoire. Je te remercie pour ta gentillesse, ton attention et ta compréhension au cours de ces trois années (qui n'ont pas toujours été faciles!). Merci aussi pour la grande confiance que tu m'as accordée.

Je voudrais aussi remercier Albert Johner, qui m'a fait l'honneur de présider le jury de ma thèse. Merci pour vos précieux éclairages sur les aspects théoriques développés dans ce travail. Je garde un très bon souvenir de nos nombreuses discussions au cours desquelles, grâce à votre patience, j'ai pu découvrir et apprendre.

Un grand merci à Jean Iss, notre ingénieur aux mains en or. De la préparation des échantillons aux diverses expériences de SFA, rayons X et FRAP, ton aide m'a été très précieuse et d'un grand secours. A tout problème, il y a une solution!

Je remercie également Thierry Charitat, pour notre collaboration sur les expériences de FRAP: c'est toujours un plaisir de travailler avec toi Thierry! Je te remercie également pour ton soutien/suivi au cours du monitorat. Je voudrais remercier aussi Michel Rawiso et Guillaume Fleith pour l'accès aux expériences de rayons X ainsi que pour leur aide, leurs explications et leur sympathie. Merci Michel pour le bon vin, caviar et autres que vous nous avez fait découvrir. Merci aussi à Joseph Selb, pour sa clarté, sa sympathie et son accompagnement dans la réalisation des mesures de rhéologie. Je remercie également Damien Favier, pour sa patience et sa gentillesse dans la réalisation de manips de scratch détournées; mais aussi pour son soutien logistique, pratique et sans faille auprès du BJC dans l'organisation d'événements au laboratoire.

Merci aussi à mes collègues de bureau, Philippe, Lila, Martin et Natasha pour leur bonne humeur, leur gentillesse et leur discrétion, et avec qui il a donc été un plaisir de "cohabiter". Enfin, un très grand merci aux BJCiennes et BJCiens, les "très" anciens pour m'y avoir entraînée dans leur bonne humeur, les moins anciens pour y avoir été avec moi au cours de ces trois années, dans la bonne humeur aussi. Je pense tout

particulièrement aux Tortues Ninja, Gladys, Andru et Arnaud ainsi qu'à Joseph. Merci à Georges pour ses "on va grailler?" au bout du fil à midi pétante, et, bien évidemment, je ne pourrai finir ce paragraphe sans remercier spécialement Andreas pour sa compagnie et les nombreuses discussions intéressantes que nous avons eues ensemble au cours de ces trois ans. Thanks Andreas!

Un grand merci aussi à ma famille et tout particulièrement à mes parents, dont le soutien infaillible à tous points de vue m'impressionne toujours autant. Vous êtes incroyables! Merci aussi à mes frères, qui (qu'ils le veuillent ou non) contribuent aussi à ce que je fais et deviens. Je remercie également la famille d'Ambroise pour leur gentillesse, leur soutien, et qui savent si bien nous requinquer quand il le faut. Merci aussi à nos adorables grands-parents, pour nous avoir fait, entre autres, l'immense plaisir d'être présents à nos soutenances de thèse. Enfin, MERCI à mon Ambroise.

Contents

Foreword

Solutions of surfactant and cosurfactant in water exhibit a very rich phase polymorphism. Depending on the concentration, provided that it is higher than the micellar concentration, the amphiphilic molecules aggregate and divide up the solution forming micelles, or long-range organised structures, like cylinders in the hexagonal phase, membranes in the cubic and lamellar mesophases. In the 60's-80's, much interest has been devoted to study diluted solutions of surfactants and polymers, showing that the polymer and the surfactant may interact to build aggregates like the necklace-type structures evidenced by Cabane and Duplessix in 1982 [15].

In the 80's, the interest moved towards more concentrated mixtures and particularly the lamellar mesophases that are able to incorporate macromolecules. The first study combining a polymer and a lamellar mesophase was carried out by Kékicheff *et al.* in 1984 [60]. The effect of the incorporation of a polymer in a lamellar phase has been then widely studied in the 90's in Montpellier [70, 10, 81, 17] and Bordeaux [34, 57].

The properties exhibited by these polymer-doped lamellar phases are indeed very interesting, for industrial applications (coatings, paints, detergents, cosmetics, pharmacology, food industry...) as well as for fundamental research, and are often unexpected. Depending on the system that we consider, the polymer can be entirely or partially located in the membrane, dissolved in the solvent or even totally or partially adsorbed on the membranes. These specific interactions between the surfactant and the polymer are at the origin of the exciting properties of these mixtures. To optimize the required properties and applications, a fundamental study is often necessary. These systems are also relevant for fundamental issues, related to biophysics and biology, or because they allow to create several interesting situations (polymer coil confinement for instance).

Nevertheless, due to the diversity of situations that can be encountered with such systems, there are still some phase behaviors that are not understood. Often, the key to obtain information about the properties of these systems consist in understanding the inter-membranes interactions mediated by the macromolecules. This is why the investigations are often directed towards the measurement and modelling of the elastic constants.

In this thesis, we focus on the system studied by Ficheux [34] SDS (sodium dodecylsulfate)/octanol/water/PEG (poly(ethylene glycol)). This work is thus directly in line with the studies lead by Kékicheff, Ficheux, Javierre [57] and Freyssingeas [40].

In the first chapter, some basics about lamellar phases and polymer-doped lamellar

phases are presented. Then, a non-exhaustive review of previous studies carried out on similar systems is done. We focus finally on the considered system.

In the second chapter, the materials and methods are presented.

The experimental results are presented in the third chapter.

The fourth chapter focuses on theoretical aspects. The first section deals with the elastic compressibility modulus $\bar{B}$, the fundamental theories are briefly recalled, then we present our contribution. The second section deals with the calculation of the dislocation nucleation radius and energy.

The fifth chapter is dedicated to the discussion and confrontation of the experimental results and theoretical considerations.

Notations

d	smectic periodicity
$\bar{d}$	interlayer spacing
δ	membrane thickness
n	number of layers in the confinement gap
l, D	surface separation
z	piezoelectric device position
$\bar{B}$, B	elastic compressibility modulus at constant chemical potential (B in the graphs, note also that "Pi" in the graphs means π)
K	normal curvature elastic constant
$\bar{K}$	gaussian curvature elastic constant
κ	normal bending elastic modulus
$\bar{\kappa}$	gaussian bending elastic modulus
Φ_{memb}	membrane mass fraction
$\bar{\Phi}$	polymer volume fraction in water
C_p	polymer mass fraction in water
M_w	molar mass, weight average molecular weight of a polymer

R_G	radius of gyration
a	monomer length
Σ	surface area per charged polar head
T	temperature
k_B	Boltzmann constant
ϵ_0	permittivity of the free space
ϵ_r	relative permittivity
e	elementary charge
L_B	Bjerrum length
λ_D	Debye length
Ψ	electrostatic potential

Chapter 1

Introduction

In a first part, we start with a section presenting basics about surfactants, lamellar phases and polymer-doped lamellar phases. Then, a section is dedicated to a brief review about polymer-doped lamellar phases. In the second part, the studied system is presented: the components and the phase diagram. This is followed by a review of the experimental work achieved about this system or similar ones. Finally the motivations complete this introductory chapter.

1 Basics

1.1 Surfactants in solution

1.1.1 Amphiphilic molecules

Surfactant molecules are constituted of two different parts covalently linked, which exhibit antagonistic properties towards water. The hydrophilic part (polar head) is soluble in water, whereas the hydrophobic part (hydrocarbon chain or aliphatic tail) wants to avoid any contact with water and is soluble in oil. This is why surfactants are also called amphiphilic molecules, which is in fact a more general term for soaps (surfactants) and phospholipids.

There are three families of surfactants, depending on the nature of the polar head:

- the ionic surfactants, cationic or anionic: their solubilization leads to the ionization of the head and a counter-ion is released (thus the polar head is finally charged, see example in Figure 1.1);
- non-ionic surfactants (the molecule does not have any charge);
- zwitterionic surfactants (neutral molecule with a positive and negative electrical charge at different locations).

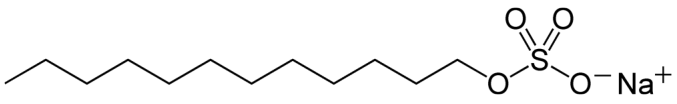

Figure 1.1: Sodium dodecyl sulfate molecule ($C_{12}H_{25}SO_4^-, Na^+$). This is an anionic surfactant: when dissolved into water, the polar head releases the Na^+ counterion and becomes negatively charged.

Because of this antagonistic character, amphiphilic molecules tend to migrate to interfaces (air/water or water/oil for example) and make possible for instance to "mix" water and oil (emulsions) and to get a large variety of auto-assembling systems.

1.1.2 Phase polymorphism

A noteworthy property of surfactant molecules is their ability to aggregate when their concentration is above the micellar concentration. Depending on the temperature and the concentration, which are crucial parameters, they are able to self-assemble in a wide variety of mesophases called lyotropic mesophases (in opposition to thermotropic mesophases for which the temperature is the only relevant parameter).

A remarkable feature of surfactants in water is that the mesophases encountered in phase diagrams are almost not dependent on the nature of the polar head neither on the morphology of the tail. The same structures are often observed and succeed each other in well-defined sequences in phase diagrams. The description of these sequences is

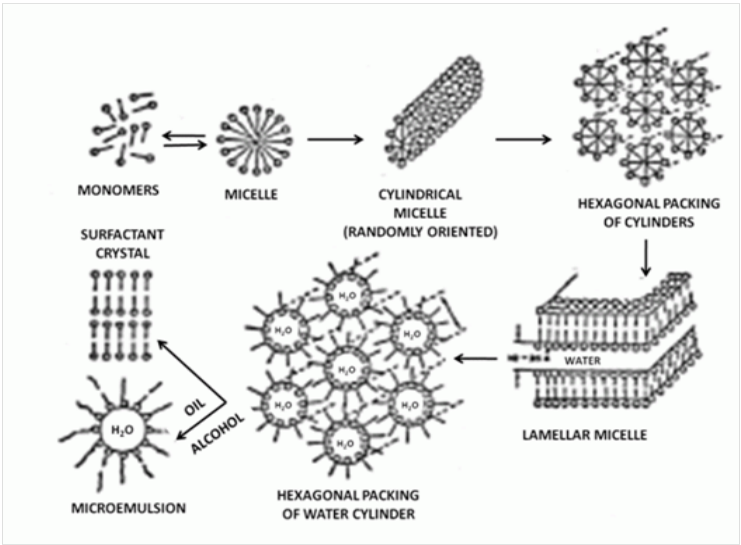

Figure 1.2: Formation of various structures in surfactant solutions with increasing surfactant concentration.

often based on geometric considerations (see [53], and Figure 1.2). Above the micellar

concentration, the molecules aggregate to build spherical micelles so as to avoid any contact between the hydrophobic tails and water. The polar heads are in contact with water and the hydrocarbon chains touch each other. When the concentration of surfactant in water increases, the micelles become cylindrical. At higher concentration, cylindrical micelles organize themselves in an hexagonal lattice (hexagonal phase) and finally, at very large concentrations, molecules are packed in stacked planar bilayers (lamellar phase). Other structures may be encountered between the hexagonal and lamellar mesophases (cubic phases for example, see Figure 1.3). Note that in these mesophases, the amphiphilic molecules keep a fluid-like structure.

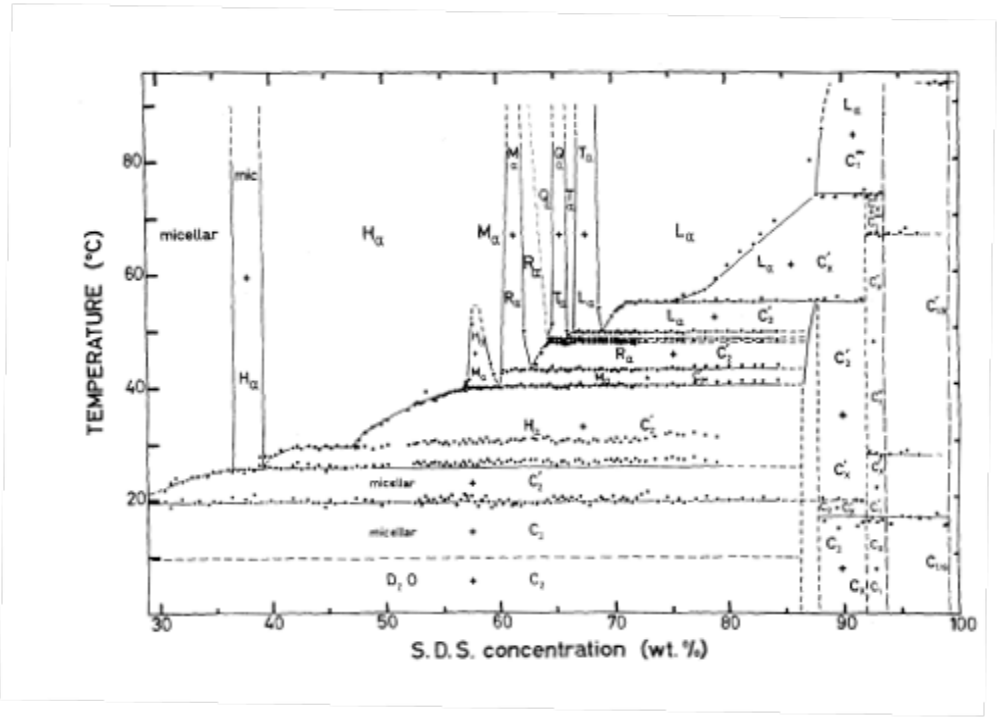

Figure 1.3: Phase diagram for the SDS-D_2O system established in 1989 by Kékicheff (see [62]). The Luzzati's terminology is adopted for the mesophases: H_α, hexagonal phase; M_α two-dimensional monoclinic phase; R_α, rhombohedral phase; Q_α, cubic phase; T_α, tetragonal phase; L_α, lamellar phase (the subscript α refers to a quasi-liquid state for paraffinic chains). Please refer to [62] for more details.

Nevertheless, for richer systems geometric considerations no longer explain the observed sequence of phases. Very often cosurfactant molecules are added since they help to widen the stability domain (in temperature as well as in concentration) of aggregates. Alcohols are often used as cosurfactants. In the ternary phase diagrams of solvent/surfactant/alcohol systems, the sequence of phases micellar $\rightarrow$ lamellar $\rightarrow$ sponge is often observed when the ratio alcohol/surfactant increases. To interpret this sequence, one has to take into account the elastic energy of the membranes as well as their entropy. The description is no longer molecular, we have to consider a bilayer.

1.2 Lamellar phase

1.2.1 Structure

A lamellar mesophase L_α is constituted of fluid membranes that are periodically stacked along one direction (their common normal). The membranes ideally extend infinitely and are parallel. Above the Krafft temperature [62], the membranes are constituted of surfactant molecules in a liquid-like state without any long-range order along the planes. The periodicity d is of the order of 3 to 20 nm, and the membrane thickness δ is about 2 to 3 nm (Figure 1.4).

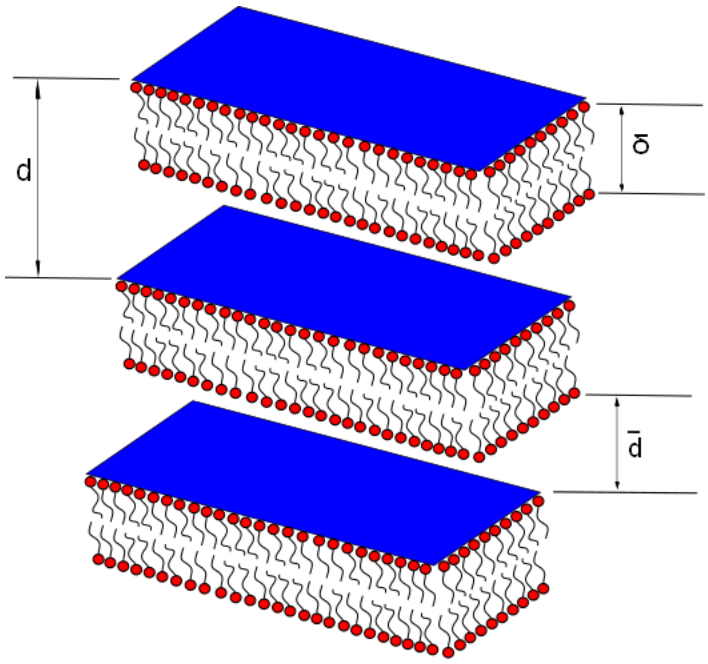

Figure 1.4: Structure of a lamellar phase L_α.

1.2.2 Elasticity of a bilayer

Helfrich demonstrated in 1973 that the curvature elasticity plays a crucial role in the elastic properties of fluid membranes. Let us consider a fluid membrane as an incompressible film, Helfrich gives the curvature energy per unit area [46], where $1/R_1$ and $1/R_2$ are the local principal curvatures of the membrane:

$$F_{curv} = \frac{1}{2}\kappa\Big(\frac{1}{R_1} + \frac{1}{R_2} - C_0\Big)^2 + \bar{\kappa}\frac{1}{R_1 R_2}$$

where $1/R_1 + 1/R_2$ is the mean curvature, $1/(R_1R_2)$ is the gaussian curvature, C_0 is the spontaneous curvature. κ and $\bar{\kappa}$ are respectively the normal and Gaussian bending elastic moduli, the first is related to the membrane rigidity and is always positive whereas the second is related to topological changes and may be positive or negative.

The first term is related to the energetic cost for the membrane to go from its state of spontaneous curvature through a different bended state. The second term is only related to the topology of the considered surface and is a constant (Gauss Bonnet theorem, please refer to [56, 79] for more details). So $\bar{\kappa}$ does not play any role in the deformations of the surface around its equilibrium position but it gives the topology of the surface at the equilibrium.

To better understand the relative stability of micelles, lamellae or sponge phases, let us consider a planar membrane that one deforms to get a sphere, a plane or a sponge element. The deformation costs an energy [8, 56]:

$$\begin{aligned} E_{\text{sphere}} &= 4\pi(2\kappa + \bar{\kappa}) \\ E_{\text{plane}} &= 0 \\ E_{\text{sponge}} &= -4\pi\bar{\kappa} \end{aligned}$$

We deduce that for

- $2\kappa + \bar{\kappa} < 0$, the vesicules phase is more stable
- $-2\kappa < \bar{\kappa} < 0$, the lamellar phase is more stable
- $\bar{\kappa} > 0$, the sponge phase is more stable.

This is why one observes the sequence spheres $\rightarrow$ lamellae $\rightarrow$ sponge when the ratio alcohol/surfactant is increased, which is linked to $\bar{\kappa}$ [82].

Nevertheless, the entropy of the membranes has also to be taken in consideration. The elasticity of the membranes plays a crucial role and according to the value of the rigidity modulus, we can distinguish two categories of membranes [8]:

- rigid membranes (biological membranes) whose normal bending elastic modulus is large compared to k_BT;
- flexible membranes, composed of one tail surfactant molecules, whose normal bending elastic modulus is of the order of k_BT.

We consider only flexible membranes, which thermally undulate a lot. As it is easier to bend an undulating membrane, the rigidity modulus is thus lowered. Both moduli κ and $\bar{\kappa}$ are renormalized depending at which scale we look at these fluctuations. A persistence length characterizing membranes flexibility is defined [8, 56]:

$$\xi_\kappa = a\exp\Big(\frac{4\pi\kappa}{3k_BT}\Big)$$

where a is a microscopic length related to the size of the surfactant molecule. For scales below ξ_κ, the membrane is considered as planar, for scales above ξ_κ, the membrane is wrinkled. The more rigid it is, the less sensitive to temperature it is and the larger is

ξ_κ. Finally, for a distance ξ larger than ξ_κ, the elastic constants are renormalized as follows:

$$\kappa' = \kappa - \frac{3}{4\pi} k_B T \ln\left(\frac{\xi}{a}\right)$$

$$\bar{\kappa}' = \bar{\kappa} + \frac{5}{6\pi} k_B T \ln\left(\frac{\xi}{a}\right)$$

The energy necessary to deform a membrane undulating on a sale ξ larger than ξ_κ decreases logarithmically with ξ. This entropic effect is remarkably at the origin of stabilizing undulation interactions, particularly for diluted non-charged lamellar phases.

1.2.3 Intermembrane interactions

The lamellar phase is a stack of a large number of bilayers that interact. These interactions are responsible for the stability of the phase, this is why it is crucial to know which interactions dominate and thus contribute to the stability of the stack.

The interactions that exist between bilayers are the Van der Waals attractive interaction, balanced by repulsive interactions, namely the hydration interaction, the electrostatic interaction (for charged membranes) and the steric undulation interaction. The hydration interaction and the Van der Waals interaction are significant for very weak interlayer spacing (2 to 5 nm for Van der Waals interaction and 1 nm for hydration). The systems that we consider in this thesis are not concerned by these interactions (diluted systems with periodicities in the range 10 nm to 20 nm). The steric undulation interaction and electrostatic interaction are presented in the Chapter 4.

1.2.4 Elastic moduli

In this section, we generalize the elasticity of a fluid membrane to a lamellar phase. Let us consider incompressible membranes that thermally undulate. The chemical potential of the surfactant is constant.

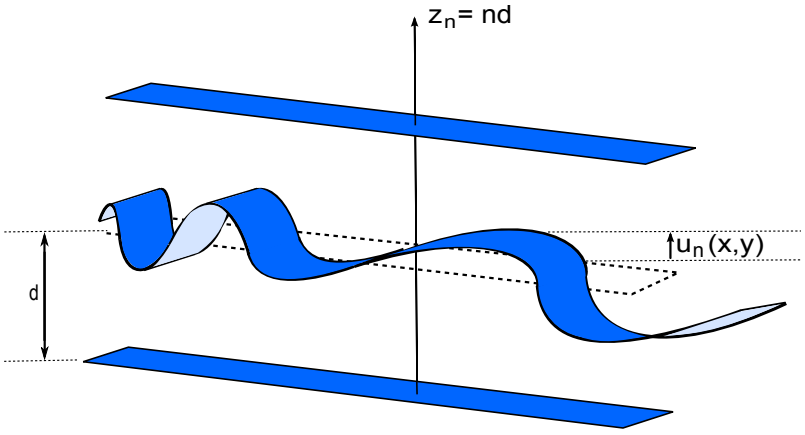

Figure 1.5: Membrane undulating between its two neighbours.

For small fluctuations around the equilibrium position, the free energy density is given by [23]:

$$f = f_{eq} + \frac{\bar{B}}{2}\Big(\frac{\partial u}{\partial z}\Big)^2 + \frac{K}{2}\Big(\frac{\partial^2 u}{\partial x^2} + \frac{\partial^2 u}{\partial y^2}\Big)^2 + \frac{\bar{K}}{2}\Big(\frac{\partial^2 u}{\partial x^2}\frac{\partial^2 u}{\partial y^2} - \frac{\partial^2 u}{\partial x \partial y}\frac{\partial^2 u}{\partial y \partial x}\Big)^2$$

where

- K is the normal curvature elastic constant, which describes the required energy to bend the bilayers together;
- $\bar{K}$ is the Gaussian curvature elastic constant, which describes the required energy to change the topology of all the bilayers;
- $\bar{B}$ is the smectic elastic compressibility modulus at constant chemical potential.

We have the following relationships:

$$K = \frac{\kappa}{d}$$
$$\bar{K} = \frac{\bar{\kappa}}{d}$$
$$\bar{B} = d\frac{\partial^2 V(d)}{\partial \bar{d}^2}$$

where $V(d)$ is the intermembrane interaction potential.

These three constants are sufficient to describe the elastic properties of the lamellar phase. Let us note the relevance of the relationship between $\bar{B}$ and $V(d)$. The measurement of the elastic compressibility modulus (Surface Force Apparatus, Dynamic Light Scattering, X-rays Scattering, Osmotic Pressure) gives insights into the intermembrane interactions.

1.3 Polymer-doped lamellar phase

1.3.1 Lamellar phase doped with a guest component

Much interest has been devoted to three-components lyotropic L_α lamellar phases, that consist of a host lamellar phase into which a guest component (proteins, clays, magnetic particles, polymers...) is incorporated. In 1994, Nallet *et al.* suggested in [76] to classify these systems in three distinct types of lamellar phases:

- the first type occurs when the amount of solvent swelling the surfactant bilayers becomes comparable to the amount of solvent separating them. The three components to be considered are the surfactant monolayer and the two solvents. Such a system is called a two-solvent lamellar phase;
- the second type arises when the surfactant bilayer hosts a colloidal component: this is a doped-bilayer lamellar phase;

- the third type arises when the solvent is now hosting a colloidal component while the surfactant bilayer remains "pure": this is a doped-solvent lamellar phase.

In this thesis we consider polymer doped-solvent lamellar phases. Three types of interactions must be taken into account:

- polymer/polymer interactions,
- polymer/solvent interactions,
- polymer/membrane interactions,

which can modify the equilibrium of the forces that are present in such a system. The nature of the interactions polymer/polymer and polymer/solvent is determined by the quality of the solvent towards the polymer and the temperature (see section 1.3.3), independently from the presence of the membranes. However, the interface membrane/solvent may alter the polymer behavior: depending on the hydrophobicity or hydrophilicity (linked to the chemical nature of the polymer), the polymer may adopt an adsorbing or non-adsorbing behavior towards the membranes. Thus a gradient of concentration settles between the membranes:

- if the polymer does not adsorb at the interface, the attractive depletion interaction occurs [32] (Figure 1.6);
- if the polymer adsorbs at the interface, two extreme situations may be encountered, depending on the quantity of polymer adsorbed and the interlayer spacing (Figure 1.7). When the fraction of polymer adsorbed at the interface is significant and the interlayer spacing is smaller than the polymer coil size, the steric repulsion between polymer segments leads to a short-range repulsive interaction. When the fraction of polymer is weak, and when the interlayer spacing is of the order of the radius of gyration of the polymer, the polymer chains can adsorb on the opposite interface, leading to a bridging attractive interaction [2].

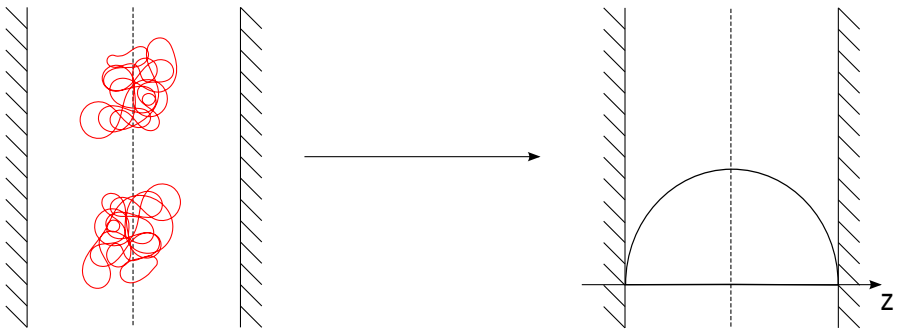

Figure 1.6: Concentration profile for a non-adsorbing polymer

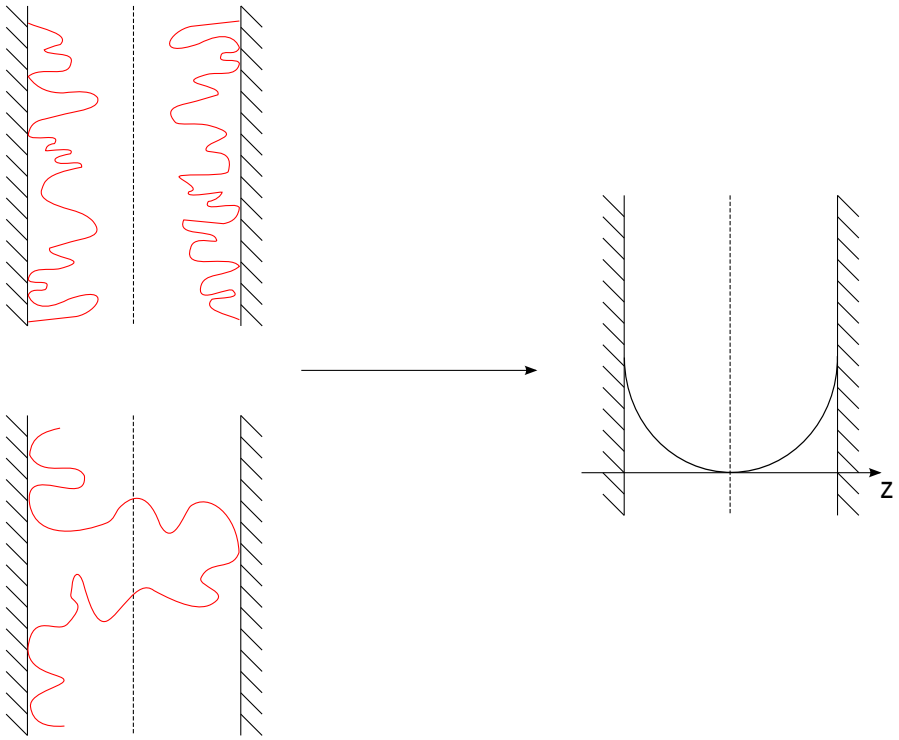

Figure 1.7: Concentration profile for an adsorbing polymer (lower drawing: bridging of a polymer chain that adsorbs onto both surfaces).

So the presence of a third component like a polymer makes more complicated the thermodynamic description of lamellar phases. Its influence on the elastic properties of the membranes deserves to be carefully examined depending on the experimental conditions considered (confinement, concentration, solvent...).

1.3.2 Elasticity of doped-solvent lamellar phases

Since doped-solvent lamellar phases contains three different components, the elastic compressibility has to be written in terms of three variables (coupled in general), namely the smectic period d and two compositions variables, the mass fractions of surfactant c_t and colloidal particles c_p. With the assumption that the system is incompressible, and for small fluctuations around the equilibrium position, the free energy density is given by [76]:

$$f = f_{eq} + \frac{\bar{B}}{2}\left(\frac{\partial u}{\partial z}\right)^2 + \frac{K}{2}\left(\frac{\partial^2 u}{\partial x^2} + \frac{\partial^2 u}{\partial y^2}\right)^2 + \frac{1}{2}\bar{\chi}_p^{-1}\delta\tilde{c}_p^2 + \frac{1}{2}\bar{\chi}_t^{-1}\delta\tilde{c}_t^2$$

where $\bar{\chi}_t^{-1}$ (resp. $\bar{\chi}_p^{-1}$) is related to the surfactant (resp. colloidal particle) osmotic compressibility and $\delta\tilde{c}_t$ (resp. $\delta\tilde{c}_p$) is the fluctuation of surfactant (resp. colloidal particle) mass fraction around the equilibrium.

K keeps the same meaning (section 1.2.4). $\bar{B}$ is now the elastic compressibility modulus at constant chemical potential of the surfactant and the guest component but

keeps the same meaning: it is still related to the intermembrane interaction potential (section 1.2.4).

1.3.3 Polymer solutions

We recall here some basics about polymer properties in solution (which depends on the temperature, the concentration, the chain conformation...). We consider only linear homopolymers.

Depending on the interactions between solvent molecules and monomers and between two monomers, we have to distinguish three situations:

- the situation where each monomer of the chain prefers to be surrounded by solvent molecules rather than by other monomers. The polymer is in good solvent.
- the situation where there is an attraction monomer/monomer that compensates the steric repulsion. The polymer is in theta solvent.
- the situation where the monomer/monomer interactions are favoured, which leads to a phase separation. The polymer is in poor solvent.

Note that these situations are all encountered for a couple polymer-solvent by varying the temperature.

Concentration effect

We consider here a polymer in good solvent.

When the amount of polymer in solution is very small, each chain occupies a volume usually described as a sphere of radius R_G, the radius of gyration. The polymer coils are far from each other and thus do not interact. This is the dilute regime.

When the concentration increases, the coils get closer and get entangled. The resulting net is characterised by its mesh ξ (the characteristic length of the system is not R_G anymore): $\xi(c) = R_G(\frac{c}{c^*})^{-\frac{3}{4}}$ where c is the polymer concentration, and c^* is the overlap concentration. Physically, this means that two monomers of the same chain cannot see each other when they are separated by a distance superior to ξ: their interactions are screened by the other monomers. ξ is independent of the chain-length. This is the semi-dilute regime.

The limit between both regimes corresponds to the situation where the coils are in contact but do not overlap, that is to say when $\xi = R_G$, and this how we define the overlap concentration: $\xi(c^*) = R_G$.

Scaling laws

For a polymer in good solvent (and in an isotropic solution), c^* and R_G are related to the chain length, i.e. to the molar mass by scaling laws (de Gennes, 1979):

$$c^* \propto M_w^{-4/5}$$

$$R_G \propto M_w^{3/5}$$

These relations are modified when the polymer is confined.

2 State of the art

2.1 Theoretical works

Daoud and de Gennes [22] in 1977 studied polymer solutions confined in small pores and defined four regimes of confinement of the macromolecules. On this basis, Brooks and Cates [11] continued to study polymer solutions confined between two walls so as to establish phase diagrams of polymer-doped lyotropic lamellar phases. Ligoure *et al.* [71] finally took advantage of the work of Brooks and Cates to calculate the polymer contribution to the elastic compressibility modulus. We address this topic with more details in the chapter 4. Note that in all these theoretical works, the polymer is a homopolymer that does not adsorb on the membranes.

Parallel to these studies, the influence of a homopolymer on the bending elastic moduli has also been investigated by de Gennes [25], Brooks [12, 13] and Clement [18]. Whatever the behavior of the polymer (adsorbing or non-adsorbing), we expect that the normal bending modulus decreases and that the Gaussian bending modulus increases. Nevertheless this modification should be very weak according to Brooks.

2.2 Experimental works

2.2.1 Adsorbing polymers

In this section we provide more details since the systems presented are directly related to the system studied in this thesis.

SDS/water/PEG system studied by Kékicheff (1984)

To our knowledge, the first work dealing with macromolecules dissolved in a lamellar lyotropic mesophase was published in 1984 by Kékicheff *et al.* [60]. The aim of this work was to show that it is possible to deform polymer coils (3-dimensional objects) into pancakes (2-dimensional objects) by using an anisotropic solvent. The choice of the system was guided by the work achieved by Cabane [14] and Cabane and Duplessix [15] about the dilute phase of the ternary system water/SDS/PEO. The macromolecules of PEO adsorb at the water/SDS interfaces of the micelles to form necklace-type structures.

In [60], they first show (X-rays and NMR experiments) that one-phase lamellar samples can be prepared for a range of compositions of the SDS/PEO/water system: the macromolecules are truly dissolved, and this does not depend on the PEO molecular weight ($M_w = 860$ to 66000 g/mol, $R_G = 12$ to 0.8 nm and water layers thicknesses ≈ 1 nm). Note that the lamellar phase of the SDS/water system exists above 50 °C and at very high concentration of SDS in water (≈ 70 wt %, Figure 1.3 and [62]).

Then, structural investigations are carried on. The average thickness of the water layers shrinks slightly when water molecules are replaced by PEO macromolecules. This effect is due to the adsorption of PEO at the water/SDS interfaces, which has in fact two effects. First, the balance between the adsorption energy and the configurational entropy of the polymer creates an interaction between membranes which is attractive

at equilibrium. Secondly, the adsorption of PEO on SDS/water interfaces is known to produce a slight increase in the average area per polar head of the SDS molecules, which should decrease the layer thicknesses δ and $\bar{d}$. The decrease of $\bar{d}$ is well observed but the authors cannot conclude about the effect on δ.

Some nonuniform deformations in the layers are observed (X-rays scattering): these deformations show up in directions parallel to the layers as pseudoperiodic correlations, with a range of 6 nm. But the lamellar structure in the perpendicular direction to the bilayers is not perturbed. As they were also observed for pure lamellar mesophases without any PEO dissolved in the vicinity of the phase boundary of the lamellar phase in the phase diagram, the feature was related to the structural reminiscence of the neighbouring phase (intermediate phases between the cylindrical hexagonal phase and the lamellar phase whose existence were a few years later elucidated by Kékicheff *et al.* [62], Figure 1.3).

In this work, the authors show also (neutron scattering) that the smaller macromolecules are arranged according to the periodicity of the lamellar mesophase and are therefore located in the water layers. For the larger ones, they spread in two or more water layers, and this crossing must be associated with some deformations of the bilayers. The authors show one possible model for these deformations in [60], the deformation is a localized pinching of the SDS bilayer coupled with the passage of one PEO strand across the bilayer.

SDS/octanol/water/PEG system studied by Ficheux (1995)

About ten years later, M.-F. Ficheux did her PhD work on the system SDS/octanol/water/PEG [33]. The octanol is long enough to be insoluble in water and slots into the membranes, it plays the role of a cosurfactant: it makes possible the existence of the lamellar phase at room temperature and with small amounts of SDS.

Ficheux established the phase diagrams of this quasi-ternary system for several molar ratios alcohol/surfactant (A/S) and for several PEG molar masses [36]. In particular, for A/S=2.7, the degree of solubilization (up to 30 wt %) is nearly independent of the molar size of the PEG in the range 3350-22600 g/mol, and is weakly dependent of the smectic period. What is remarkable is the appearance of a two-phase region in the phase diagram for both PEG of molar masses $M_w = 8000$ and 22600 g/mol. Two lamellar phases coexist in this region. The extent of this region, that is bounded by two critical points, is polymer size dependent, and is less wide for the PEG 8000. The periodicity d and bilayer thickness δ decrease when the concentration of polymer in water increases, as already observed (for d) and assumed (for δ) by Kékicheff in 1984. The observed decrease of δ is attributed to a slight increase of the average area per polar head in the bilayer [34].

They focused then on the system SDS/octanol/water/PEG 22600 (A/S=2.7). In a first study [34], they qualitatively show that an increase in the polymer concentration in water leads to a decrease of the elastic compressibility modulus $\bar{B}$ (neutron scattering). They then attempt a quantitative determination of the elastic compressibility modulus by dynamic light scattering. They are able to get results for one sample (owing to big

difficulties in obtaining well oriented samples) with composition $\Phi_{memb} = 0.24$ wt % and $C_p = 0.05$ wt %: $\bar{B} = 1.9$ kPa and $K \approx 1$ pN. They do not give a precise interpretation of this value. Note that this lamellar mesophase is located in the phase diagram close to one critical point ([36, 34], $\Phi_{memb} = 0.32$ wt % and $C_p = 0.038$ wt %).

In a second study, Ficheux, Bellocq and Nallet investigated the approach of this critical point by studying the Caillé exponent η (neutron scattering, [35]), which is proportional to $1/\sqrt{K\bar{B}}$. This exponent apparently diverges at the critical point, which would goes together with the decrease and disappearance of $\bar{B}$ at this special point.

Similar systems (Javierre, Freyssingeas, 1999)

Freyssingeas studied the SDS/pentanol/water/PEG system with the Surface Force Apparatus technique [40]. The period of the stack is fixed (constant membrane volume fraction, and constant ratio $A/S = 8$) and the parameter of the study is the polymer concentration in water. When the polymer concentration in water increases, the magnitude and the number of oscillations of the force−distance profiles decrease, showing that the intermembrane interactions become weaker. This is further supported by the experimental results concerning the elastic compressibility modulus: it decreases when C_p increases. The possible origins discussed for this enhanced attractive contribution are the adsorption of the PEG at the interfaces which could lead to a bridging interaction; or the altering of the classical electrostatic interaction due to the PEG (the charge distribution could change); or both effects are superimposed.

In this work, no polymer effect on the layer thickness and the period are observed.

Javierre devoted a part of her PhD work to the study of the SDS/hexanol/water/PEG system [56] ($A/S = 2.8$). Briefly, she performed neutron scattering experiments upon the approach of a suspected critical point (by increasing the membrane volume fraction toward the biphasic region, at C_p fixed and vice-versa). As Ficheux, she observed that the Caillé exponent increases and this is attributed to a decrease of $\bar{B}$ (upon the assumption that κ is constant on a dilution line, and thus K increases).

Like above, no polymer effect on the layer thickness and the period are observed.

Conclusions

It is interesting to remind the effect of the alcohol chain length. By comparing the three systems, it appears that:

- the polymer solubility and the extent of the two phase area increase with the alcohol chain length (no biphasic region for the system with the pentanol);

- the affinity of PEG with the bilayer increases with the alcohol chain length.

For the three alcohol/SDS/water/PEG systems, the interactions between bilayers are less repulsive in the presence of the polymer.

2.2.2 Non-adsorbing polymers

To study a polymer solution confined between two slits, a very good model system is a lamellar phase made of a cationic surfactant into which a hydrosoluble polymer is incorporated. To our knowledge, such systems have been widely studied in Montpellier in the years 1995-2000.

Ligoure and Bouglet studied the system polyvinylpyrrolidone (PVP)/cetylpiridinium chloride (CPCl)/hexanol/water [70, 71, 8, 9]. The polymer can be incorporated in the lamellar phase in all proportions and this does not modify the lamellar structure. This is checked in the four different regimes of confinement. Nevertheless, they noticed that the polymer induces a weak attractive interaction between bilayers (the Bragg peaks are less sharp). By adding salt to the solvent, they are able to balance the electrostatic repulsion which leads to a lamellar/lamellar phase separation. One critical point is found for a specific salt concentration. Finally they interpret the experimental results concerning the elastic compressibility modulus thanks to the theoretical model that they developed in the four regimes of confinement (see chapter Theory for more details).

On the same system PVP/CPCl/hexanol/water, Bouglet et al. [10] investigate the effect of the polymer on the bending elastic moduli κ and $\bar{\kappa}$ of the lamellar phase. They found that the mean bending modulus κ is insensitive to the amount of polymer, in agreement with theoretical predictions (NMR technique). But they observe a large proliferation of focal conic domains (polarizing microscope) even with small amounts of polymer, and this is confirmed by cryo-TEM experiments. This indicates that the presence of the non-adsorbing polymer strongly decreases $\bar{\kappa}$, in contradiction with theoretical predictions.

Porcar *et al.* incorporated PVP to the neutral system TX100/TX35/decane/water, and they doped it with the cationic surfactant CPCl ([79], [80], [81]). They observe four critical points by varying four different parameters (surface area per charged head group, polymer confinement, oil layer thickness and temperature). Thanks to the theory of Ligoure *et al.*, they are able to interpret the occurence of three of these critical points.

2.2.3 Copolymers

A lot of studies have been devoted to the incorporation of copolymers to lamellar phases, in particular amphiphilic block copolymers since they are of great advantage in the stabilization of colloidal dispersions. These studies have been directed towards biomaterials, such as liposomes and vesicles, where the presence of terminally grafted polymers at the interface with biofluids dramatically enhances their lifetime in the bloodstream. Please refer to the PhD work of Castro-Roman [16] for a complete review on this topic.

3 System studied

3.1 Presentation

In Figure 1.8, the phase diagram established by Ficheux [33, 34] is presented. Let us take her notations: C_p denotes the polymer mass fraction in water, Φ_{memb} denotes the membrane *mass* fraction. This phase diagram has been established until $C_p = 0.60$.

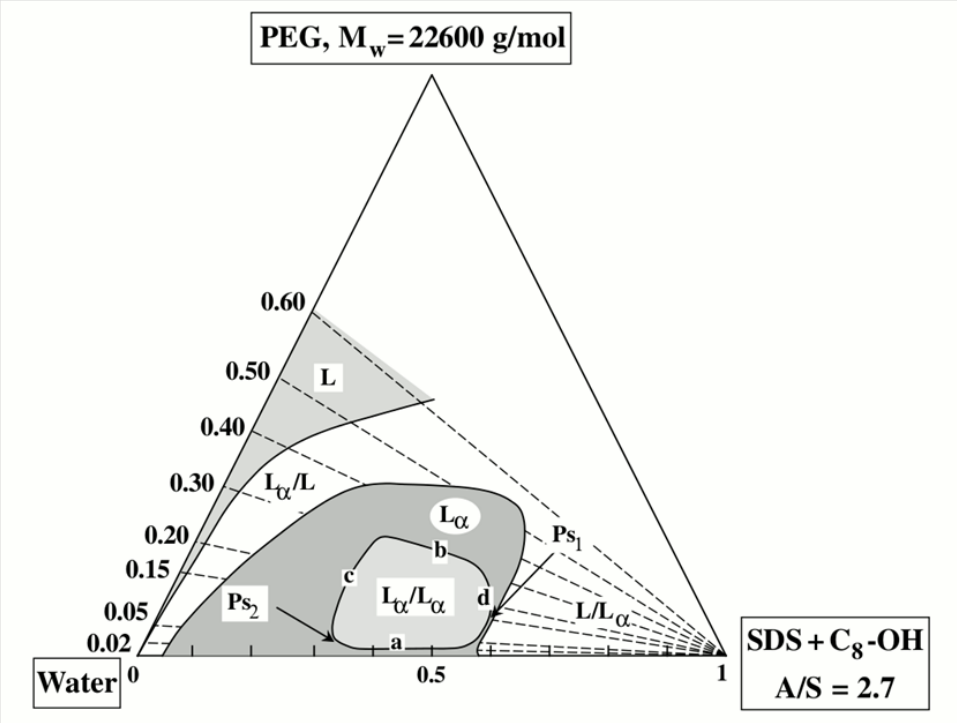

Figure 1.8: Section at constant temperature (T = 25 °C) and membrane composition (octanol to SDS molar ratio A/S = 2.7) of the quaternary phase diagram water/octanol/SDS/PEG established by Ficheux [33]. Compositions are given as wt % fractions. The "membrane" corner corresponds to SDS and octanol. L is an isotropic phase, L_α a lamellar phase. L_α/L_α and other similar symbols represent two-phase domains. P_{s1} and P_{s2} are critical points.

We distinguish an isotropic phase L, probably constituted of SDS micelles decorated by polymer, one lamellar phase L_α and three biphasic regions. We see immediately that it is possible to dissolve large amounts of polymer, until $C_p = 0.50$. For a lamellar phase with $\Phi_{memb} = 0.40$, it is possible to replace half of water molecules by macromolecules in weight.

One notices that the richer in polymer the solvent is, the less one can dilute the lamellar phase. On contrary, the polymer does not seem to have a crucial effect on the stability of concentrated lamellar phases: the phase-boundary at high Φ_{memb} is parallel to the water/PEG axis. Biphasic regions surround this lamellar region, where an

isotropic phase L coexists with a lamellar L_α one. The isotropic phase of the equilibrium L_α / L is a polymer solution (very poor in SDS), the L_α phase contains less polymer (RMN experiments performed by Ficheux [33]). In the equilibrium L/L_α, the isotropic phase is a solution rich in octanol that contains polymer, like for the L_α phase. The third biphasic region, included in the lamellar phase and appearing at intermediate C_p and Φ_{memb}, was unexpected. Let us note that beyond this coexistence region between two lamellar phases, a unique lamellar phase is regenerated, at high or low concentration of polymer in water, or at small or large smectic period. Besides, the upper and lower boundaries of the two-phase domain follow closely dilution lines, meaning that on these boundaries the polymer concentration in water is constant ($C_p = 0.01$ and $C_p = 0.35$) respectively. Similarly, the left boundary corresponds to a line at constant membrane fraction $\Phi_{memb} = 0.30$.

Ficheux identified from the splitting Δq between the Bragg peaks positions of the two coexisting lamellar phases two good candidates for critical points [34], at $\Phi_{memb} = 0.58$ and $C_p = 0.15$ for P_{s1} and $\Phi_{memb} = 0.32$ and $C_p = 0.038$ for P_{s2}. In [35], Ficheux *et al.* show that the Caillé exponent diverges on the approach of P_{s2}, which is attributed to the vanishing of the layer compression modulus $\bar{B}$.

3.2 Motivations

This system opens naturally several ways of study. The starting point of this thesis was to approach one of the critical points (P_{s2}) by measuring directly the intermembrane interactions (elastic compressibility modulus $\bar{B}$), with the Surface Force Apparatus technique (SFA), of the lamellar mesophase confined between the two macroscopic SFA surfaces. How does the force evolve on the approach of P_{s2}? Moreover, on this system, there are very little direct quantitative measurements of the elastic compressibility modulus. The SFA technique provides also information about the dislocations that nucleate or annihilate depending on the movement of the surfaces. This is thus possible to deduce the Burgers vector of the dislocations.

An other intriguing point concerns the polymer diffusion in the water layers. How does the interaction between the polymer and the membranes (adsorption) influence the diffusion? One can wonder also about the influence of the polymer concentration, or of the confinement of the macromolecules. Is the diffusion modified on the approach of the critical point? The Fluorescence Recovery After Photobleaching technique seems appropriate to investigate such problems.

Upon the approach of the critical point, one may expect that the lamellae undergo structural modifications like periodic defects in some directions (holes, connected membranes...). When an oriented sample is exposed to a X-ray beam, these defects should give rise to a diffuse scattering pattern that may be observed by performing Small Angle X-ray Scattering.

In this work, some aspects related to these questions are examined.

Chapter 2

Materials and methods

1 Materials

1.1 Sodium dodecylsulfate

The anionic surfactant, sodium dodecylsulfate (SDS), was purchased from Sigma-Aldrich as an "ACS reagent, $\geq$ 99%". The CAS number is 151-21-3. The molar mass is 288.8 g/mol and the density 1.16 at room temperature.

One concern with solutions of SDS, is the acid-catalyzed hydrolysis of the polar head which produces dodecanol and sodium hydrogen sulfate (autocatalytic reaction). This reaction is favoured when the temperature increases or when the acidity of the medium increases [65, 73]. The pH solutions of SDS in milli-Q water was 6.41 for a 10^{-1} mol/L solution and 6.35 for a 10^{-2} mol/L solution, indicating chemical stability of the surfactant. As the hydrolysis produces dodecanol, the surface tension has also been checked: it reveals the expected features with a critical micellar concentration of 8.3 mmol/L and a surface tension of around 39 mN/m in agreement with the expected value of 38.8 mN/m at 25 °C.

1.2 Octanol

The octanol was purchased from Sigma-Aldrich as an "1-octanol ($C_8H_{18}O$), anhydrous, $\geq$ 99%". The CAS number is 111-87-5. The molar mass is 130.23 g/mol and the density 0.827.

The refractive index was measured with a refractometer RFM340 Bellingham+Stanley Ltd., and found to be 1.428 in agreement with literature.

1.3 Water

The water is Milli-Q water (apparatus from Millipore), of resistivity 18.2 MΩ.cm at 25°C.

1.4 Poly(ethylene glycol)

The poly(ethylene glycol) (PEG), a linear water-soluble non-ionizable polymer, was purchased from VWR as "polyethylene glycol ($HO(C_2H_4O)_nH$) for synthesis, of average molecular weight $\sim$ 20 000 g/mol" of brand Merck. The CAS number is 25322-68-3.

The gel permeation chromatography performed in the Institute revealed a molar mass of M_w =18 713 g/mol and a polydispersity index $I = 1.05$.

The density of PEG solution is calculated with the relation given in [56] (densimeter PAAR): $d = 0.9966 + 1.65 * 10^{-4} c$ where c is the polymer concentration in g/L, at 25°C.

The radius of gyration is determined thanks to the set of data given in [60] (the R_G versus M_w relation was determined by neutron scattering). For a polymer of molar mass M_w =18 713 g/mol, a radius of gyration of 56 Å is inferred.

The overlap concentration is estimated with $c^* \sim \frac{M_w}{4\pi/3R_G^3}$ [44] which gives $\sim$ 42 g/L.

Finally, the refractive indexes of various PEG solutions in water have been measured using a refractometer RFM340 Bellingham+Stanley Ltd., (Figure 2.1). The experimental data can be fitted by the linear relation: $n_p = 1.333 + 0.0014\, C_p$ where C_p is the polymer weight % in water.

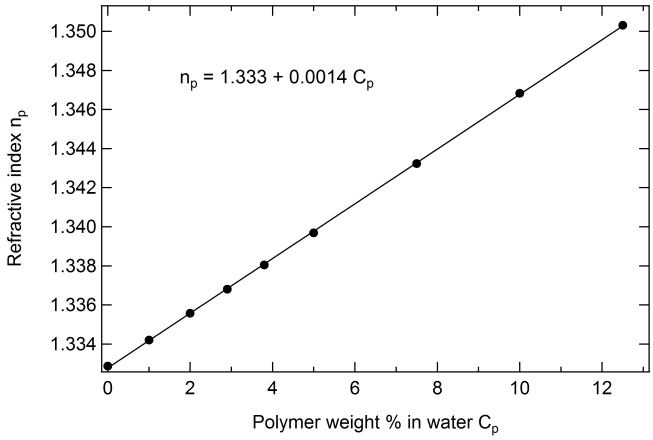

Figure 2.1: Refractive index of PEG solutions plotted as a function of the polymer weight % in water.

1.5 Lamellar mesophases samples preparation

The samples were prepared following the procedure:

- first the polymer content is weighed and dissolved into Milli-Q water; the aqueous solutions are gently stirred for a few hours at room temperature. The polymer solutions form clear solutions in the whole range of compositions. Note that fresh solutions were always prepared especially for preparing the mesophase samples used in SFA technique.

- the required quantity of SDS is weighed in a vial (for small amounts of sample) or in a centrifugation tube (for samples $\simeq$ 60 mL, for SFA experiments); then the corresponding amount needed of polymer solution is taken off from the mother solution and added to the SDS. The container is then sealed and attached to a setup that allows the container to rotate slowly. Thus, the SDS dissolves completely in the solution in a few hours;

- finally the required quantity of octanol is added to the mixture; slow rotation of the container is carried out for 3 to 4 weeks in a oven at (25.0 ± 0.1)°C. From time to time the process is interrupted and the container is centrifuged at 5000 rounds/minute for a few minutes so as to eliminate the bubbles.

This procedure allows to obtain homogeneous mixtures at equilibrium. The samples are then stocked in the same oven at (25.0 ± 0.1)°C before use.

2 Methods

2.1 Optical microscopy

Polarized optical microscopy is used to check that the mesophases prepared as explained above are macroscopically homogeneous and located in the lamellar phase of the phase diagram. Indeed, lamellar phases are birefringent with characteristic textures that can be observed between crossed polarizers.

Textures show a spatial organization that is well larger than typical dimensions of the structure. But the properties of symmetry of the structure impose some conditions to the texture, which allow in certain cases to identify the structures by observing the textures.

In particular, some defects like crosses can exist only in layered structures. For lamellar phases one can observe for example four-leaf clovers which correspond to one unique focal domain, or oily streaks and fan-like morphologies that correspond to a juxtaposition of a lot of focal conic domains [66] (Figure 2.2). Sometimes, some spherulites are formed in the lamellar phase which gives the Maltese crosses.

2.2 X-ray diffraction

X-ray diffraction experiments were performed in our laboratory, within the group of Michel Rawiso, by using a diffractometer developed by Molecular Metrology (Elexience in France). X-rays are produced thanks to a rotating anode tube. The diffractometer operates with a pinhole collimation of the X-ray beam and a two-dimensional gas-filled multiwire detector. A monochromatic ($\lambda = 1.54$ Å with $\Delta\lambda/\lambda < 4\%$, K-$\alpha$ emission of the copper) and focused X-ray beam is obtained through a multilayer optic designed and fabricated by Osmic. The size of the incident beam on the sample was close to 600 μm. The sample to detector distance was set at 1.50 m, allowing to explore scattering

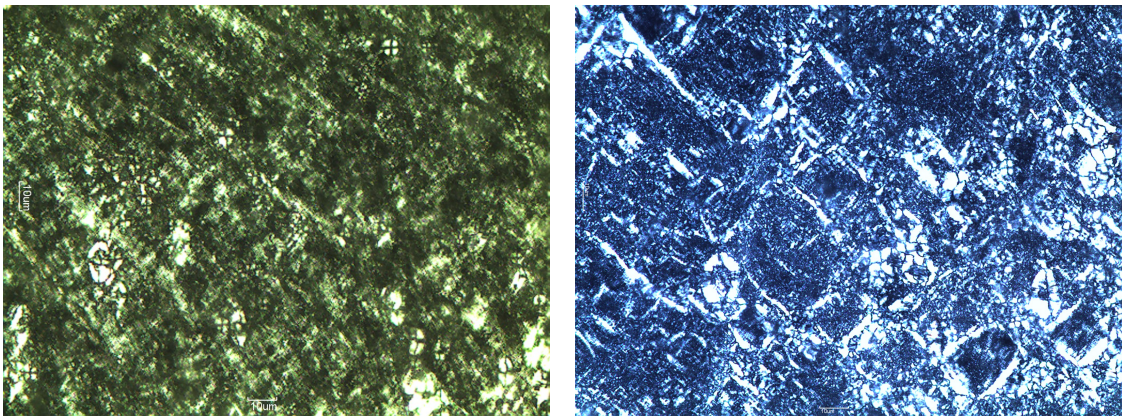

(a) (b)

Figure 2.2: Textures of the lamellar mesophase: four-leaf clovers, structures in fan, oily streaks and Maltese crosses. Scale bar: 3.5 mm $\equiv$ 10 μm.

vectors ranging from q = 0.006 $\mathring{\text{A}}^{-1}$ to 0.16 $\mathring{\text{A}}^{-1}$. $q = 4\pi\sin(\theta/2)/\lambda$, where λ and θ are the wavelength of the incident beam and the scattering angle, respectively. The q-resolution related to the beam size on the sample and the beam divergence was close to 0.005 $\mathring{\text{A}}^{-1}$. Cells of 1 mm thickness and calibrated Mica windows were used as sample holders. Measurements were performed at room temperature.

2.3 Surface Force Apparatus

Methods involving direct measurement of molecular interactions between macroscopic surfaces are based on the measurement of two quantities: the force of interaction and the distance that separates them. With the surface force apparatus (SFA), both attractive and repulsive forces can be measured from the deflection of a sensitive spring (cantilever). In contrast to AFM the absolute separation between the surfaces is exactly defined (a true zero for the origin of distances is calibrated) and accurately determined by means of interferometric techniques. In most cases the force F scales with the radius of curvature of the surfaces R. In general the normalised force F/R can be directly related to the interaction free energy E. One of the most powerful techniques to measure the force profile between two surfaces is the interferometric surface force apparatus pioneered by Israelachvili *et al* [52, 54] in the mid 70s.

2.3.1 Principle

SFA allows the force to be measured as a function of separation between two macroscopic surfaces in air or immersed in liquids. The separation between the surfaces is determined by optical interferometry and the force is read from the deflection of a cantilever spring on which one of the surfaces is mounted and that can be moved to

bring the surfaces to a given separation. The principle behind the SFA is depicted schematically in Figure 2.3.

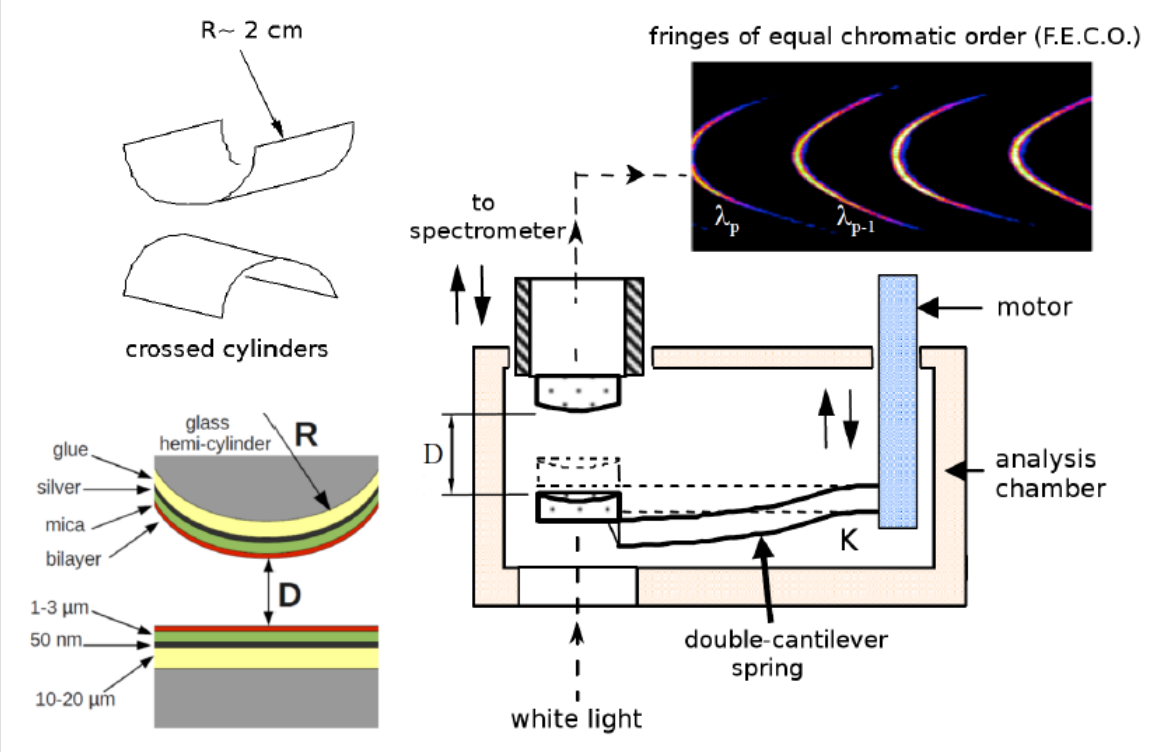

Figure 2.3: A schematic representation of the interferometric surface force apparatus (SFA). The surfaces are attached to a piezoelectric crystal and on a double-cantilever spring, respectively. The crossed cylinder geometry is equivalent to that of a sphere against a flat as the radius of curvature, R (about 2 cm), is much larger than the surface separation D (in the drawing the curvature of the surfaces has been exaggerated). The interference FECO pattern set in incident white light gives the real separation between the surfaces (relative to silver backing) and their local shape.

Preparation of the surfaces

Precise force measurements require a pair of surfaces which produces interference fringes yielding resolution of less than a few Angstroms. Thus delicately thin (1 - 3 μm thick), molecularly smooth and optically transparent substrates coated with silver layers need to be prepared. To ensure a contaminant free surface the whole sample preparation is carried out in a clean room.

The preferred substrate in the SFA is muscovite mica, which is a naturally occurring mineral consisting of aluminosilicate layers held together by ionic bonds between potassium. When mica is cleaved along crystallographic planes, the ionic interlayer bonds are broken and large atomically smooth areas (flat to within 0.1 nm) can be obtained, whose charge is of 1 electron per 48 $\mathring{A}^2$. The mica is cleaved to obtain 1 - 3 μm thick

sheets possibly free of cleavage steps. Small mica squares (1 cm x 1 cm) are cut with a white-hot platinum wire (0.1 mm diameter) and immediately placed face down on a freshly cleaved, large backing sheet onto which it adheres. In this way the surface of the pieces in contact with the backing sheet are protected from contamination. The backing sheet decorated with the small thin pieces can be transported and coated with a ~ 50 nm silver layer by vacuum deposition (reflectivity $> 98\%$ in the green region of the visible spectrum).

Prior to an experiment the thin mica sheets are glued, silvered side down, to the supporting fused silica cylinders (highly polished to give a cylinder with a radius of 2 cm). As glue the thermosetting resin, Epikote 1004 from Shell Chemical Co. (melting point ca. 100 °C) is used. The Epikote resin is very suitable as a glue for three reasons: it is transparent, it does not change its volume as it sets, thus preventing any stress in the glued mica sheet upon cooling and it is not a source for contaminants [42].

Crossed cylinder geometry

The two thin sheets of mica freshly attached to the curved supporting silica disks, are mounted in the apparatus facing each other with the cylinder axes at right angles to each other (Figure 2.3). This geometry allows the precise alignment of two interacting plates and unwanted effects at the edges of the plates are avoided. The geometry of crossed cylinders has an additional advantage. If the region of contact becomes contaminated or locally damaged (for example due to adhesive properties of the surfaces) during the course of an experiment, one surface can be moved, first along the axis of one cylinder and then along the other to reveal a new and pristine contact area. Changing contact position several times under the same solution conditions within the same experiment increases the statistics of the measured data and the reliability of the results.

The crossed cylinder arrangement is also convenient for the comparison of experiment with theory. Let us note R the inverse Gaussian curvature ($R = \sqrt{R_1 R_2}$). According to Derjaguin the force between crossed cylinders of equal radius R, is the same as the force F between a sphere of radius R and a plane flat surface or between two spheres each of radius $2R$ as R is much larger than the separation between the substrates. Further, this force is equivalent to the free energy $E(D)$ of interaction per unit area between two plane parallel surfaces of the same material [27]:

$$\frac{F}{R} = 2\pi E \tag{2.1}$$

For this reason, forces $F(D)$ measured with the SFA between two crossed-cylinders of mean radius of curvature R are routinely plotted as F/R and are therefore implicitly related to the interaction free energy $E(D)$.

The relation is only valid within certain limitations. The Derjaguin approximation holds provided the range of the force is small compared to the radius of curvature of the surfaces. This is always fulfilled in measurements using the SFA ($R \sim 2$ cm and $D \sim 0.1$ nm - several μm so $R >> D$). R needs also to be independent of D (the surfaces must remain undeformed) so that $F(D)$ is mathematically well-defined, single-valued and integrable. This may not always be fulfilled. Especially when the surfaces

are being deformed due to the action of strong surface forces the comparison between experiments and theory is no longer straightforward. In some cases the application of equation (2.1) can be questionable. Hence statistical mechanic derivations have to be applied to correctly describe the interactions e.g. for oscillatory structural forces arising between curved surfaces in fluids.

We will see that for complex fluids such as confined lamellar mesophases, the Derjaguin equation is questioned as hydrodynamics interactions and propagation of the layered order can be long-ranged. We have therefore developed special analysis of the collected data (see Chapter 3).

Distance measurement

The outer silvered faces of the two mica sheets form an optical cavity (a Fabry-Perot like interferometer) providing the means to measure distances. Collimated white light is directed and impinged normal to the surfaces. Multiple reflections occur between the two reflective films. The transmitted light consists of a spectrum of intensity maxima known as fringes of equal chromatic order (FECO) [51]. If a microscope focuses the light emerging from the interferometer on the entry slit of a grating spectrometer, the fringes are split up according to their wavelength. Analysis of this array allows to measure the optical thickness of the film and simultaneously determine the thickness and the refractive index of each layer in the interferometer.

It should be noted that multiple-beam interferometry requires the presence of two highly reflective thin films separated by one or more dielectric materials of total thickness greater than the wavelength of visible light. The spectrum can be accurately predicted using classical electromagnetic theory, and the FECO wavelengths depend on the thicknesses and the optical properties of the media (refractive indices and their dispersions) [51, 89]. Since mica is birefringent, each fringe normally appears as a doublet. Thus one fringe is extinguished by passing the light through a polariser.

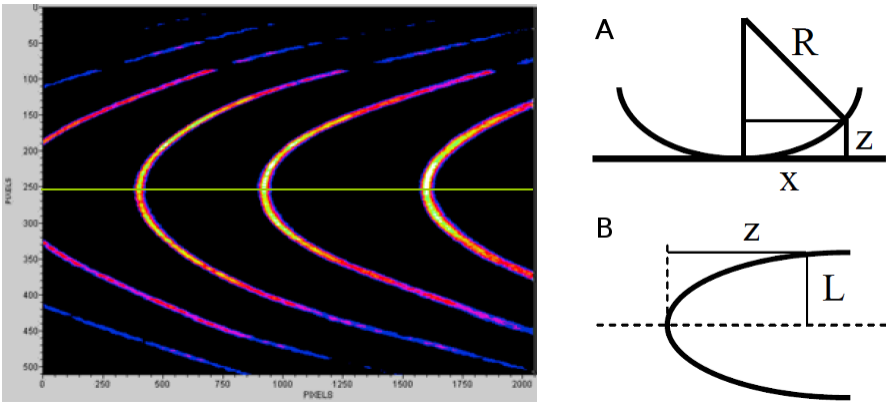

Figure 2.4: Typical interference FECO. Schemes A and B show the relation between the geometry of a sphere against a flat suface (A) and fringe parabolic shape (B).

The spatial positions of the observed FECO change continuously as the separation

between the surfaces is varied. The separation determined by multiple-beam interferometry is an absolute value relative to the predetermined zero separation (measured distance of contact in air, or in an aqueous solution). This is an important advantage over most of the non-interferometric devices. Under optimum experimental conditions a 0.1 nm resolution can be achieved for surface separations larger than 5 nm.

Since the gap between the curved surfaces is not uniform, the shape of the observed FECO is a direct representation of the relative geometry of the surfaces (Figure 2.4). In particular the curvatures of the surfaces can be measured along two perpendicular directions in the plane of the surfaces, R_1 and R_2, and thus the force can be normalized by the mean Gaussian curvature ($R = \sqrt{R_1 R_2}$). Uncertainties on the measurement of R are 10%.

The lateral magnification is set by the microscope (about x32) that focuses the light emerging from the interferometer to the spectrometer slit. Features of lateral dimensions larger than about 1 μm can be observed e.g. when the surfaces are brought into a strong adhesive contact a flattened region forms, which is easily observed in the FECO fringe pattern because the glue adhering the mica to the discs is rather compliant.

Force measurement

In the SFA design schematically displayed in Figure 2.3, one of the surfaces is attached to a piezoelectric tube. The other one is mounted at the end of a double force-measuring cantilever (of constant stiffness $K_c \sim 50$ N/m) that can be moved to bring the surfaces to a given separation. Accurate force measurements require precise control of the surface separation. This is usually realised either mechanically by a system of micrometers and differential springs or by piezoelectric devices. The advantage of the latter ones is, that they displace the surfaces smoothly without causing vibrations. However the piezo-actuators are prone to nonlinearity, hysteresis and creep, which have to be corrected by electronic feedback system to provide a subnanometric precision. In the setup of the laboratory an ensemble of piezoelectric actuators (Physik Instruments) has been mounted. The non-linearity and hysteresis are electronically corrected. The range of displacement is 100 μm and the minimum repeatable step is 0.5 nm.

Forces between the surfaces of the crossed cylinders are determined from the deflection of the cantilever spring system and calculated by Hookes law with the known spring constant. The spring constant is calibrated with an accuracy of 1 % after each experiment. Small calibrated weights are placed at the surfaces and the deflection is measured. A double cantilever is preferable to a single leaf spring because it prevents the curved surfaces from rolling and shearing as the load is varied. The force can be determined with a resolution of about 50 nN. When normalised by the radius of curvature of the surfaces, this is equivalent to 0.002 mN/m, corresponding to a free energy ~ 0.3 μJ/m^2 [58].

A force measurement is started with the surfaces separated well beyond the range of any surface force. Then the surfaces are stepwise approached. After each displacement, the surfaces are allowed to come to rest and their true distance is measured by the

optical method. This process is repeated and the measured separation profile as a function of the actuator displacement is recorded. A straight line of slope equal to 1 is obtained at large separations where no force of interaction occurs. Repulsive forces are seen as a continuous deflection away from contact and are limited only by the onset of deformation of the surfaces. Strongly attractive surface interactions lead to a mechanical instability. Similar to AFM it occurs when the slope of the force-distance profile exceeds the cantilever spring constant. As a consequence the technique allows forces to be measured only over the regions where the gradient of the force ($\partial F/\partial D$) is smaller than the spring constant K. Thus only parts of the force curves are directly accessible and the force vs distance profile appears to be discontinuous, with jumps from unstable (e.g. $\partial F/\partial D > K$) to stable mechanical regimes.

2.3.2 Instrumentation

The SFA displayed in Figure 2.5 is home-built by the group of Patrick Kékicheff at the Institut Charles Sadron, Strasbourg.

(a) (b)

Figure 2.5: Figure (a): setup of the SFA, on the left the electronics, in the middle the SFA chamber in the plexiglas cabinet, on the right the spectrometer. Figure (b): SFA chamber filled with a lamellar mesophase, through the window, the surfaces are almost not visible due to the non translucid sample.

The upper surface is attached to the piezo actuator (Physik Instrument) with a max. travel of 100 μm and a precision of 0.5 nm, used for fine approach of the surfaces. The lower surface is placed at the end of a double-cantilever spring made of stainless steel with a force constant around 50 N/m. The sample chamber with a volume of 45 cm^3 is also made of chemical inert stainless steel in order to prevent contamination of the sample surfaces or solutions. For coarse alignment the surfaces are moved with screw spindle connected to a computer which allows displacement of the upper surface with a precision of 0.1 μm. In order to avoid thermal drifts of the mechanics, the temperature of the sample chamber is strictly controlled to 25 °C using a PID controller (Lakeshore 340) which regulates the temperature with a precision of 0.5 °C/24 h in the

laboratory, 0.05 °C/24 h within the plexiglas confinement and 0.001 °C/h within the sample chamber. The temperature of the laboratory room is fixed 3 °C lower than the desired temperature of the SFA.

Collimated white light from 150 W halogen lamp is directed in the optical cavity via liquid core optical fiber. The resulting interference pattern is enlarged by a 16x objective and directed to a Jobin-Yvon imaging spectrometer by an imaging optical fiber (composed of 120 000 single fibers) and a doublet adaptator (x2) to enter into the spectrometer. The spectrometer is coupled with a liquid nitrogen cooled CCD camera (2048 x 512 pixels). The spectrometer-camera system is controlled with a computer and the interference patterns are analysed with a home written software.

2.3.3 Refractive index of the medium

To measure the separation between the surfaces, the ordinary refractive index of the medium n is required. The ordinary refractive index of an array of plates (membranes) of refractive index n_m immersed in an aqueous medium (polymer solution) of refractive index n_p and occupying a volume fraction t is given in [63]:

$$n^2 = \frac{n_m^2 n_p^2}{t n_p^2 + (1-t) n_m^2} \tag{2.2}$$

n_p is given by the curve presented in Figure 2.1. The refractive index of the membrane is calculated in this way:

$$n_m^2 = t_s n_s^2 + (1 - t_s) n_a^2 \tag{2.3}$$

where t_s denotes the volume fraction of SDS *in the membrane*, $n_s = 1.461$ the refractive index of SDS and $n_a = 1.428$ the refractive index of octanol. This relation gives $n_m = 1.4405$.

2.3.4 Force calculation

The force is calculated from the piezoelectric device position and the surface separation (see Figure 2.6):

$$F_i = F_0 + K_c(C(z_i - z_0) - (l_0 - l_i)) \tag{2.4}$$

where F_i is the force calculated at the M_i point, F_0 is the unknown force at the starting point M_0, and l_i, l_0, z_i, z_0 are the coordinates defined as follows:

$$M_i \begin{pmatrix} l_i \\ z_i \end{pmatrix} \qquad M_0 \begin{pmatrix} l_0 \\ z_0 \end{pmatrix}$$

where the separation between the two surfaces at the M_i (resp. M_0) point is l_i (resp. l_0) and z_i (resp. z_0) is the piezoelectric device position at M_i (resp. M_0). K_c is the

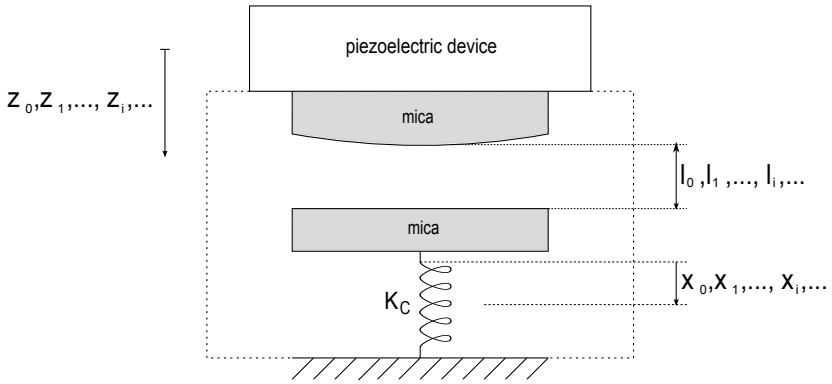

Figure 2.6: Simplified representation of the surfaces and cantilever spring, the dashed line represents the chamber which is filled with the sample. When the upper surface is moved from the point M_{i-1} to M_i, the cantilever spring deviates from an additional quantity $\Delta x_i = x_i - x_{i-1} = (z_i - z_{i-1}) - (l_{i-1} - l_i)$. The total deformation at the point M_i is $x_i - x_0 = (z_i - z_0) - (l_0 - l_i)$.

cantilever spring constant. C is the calibration coefficient of the experiment, defined as the slope of the graph $(l,\, z)$ far from the contact position:

$$C = \frac{\Delta l}{\Delta z}$$

The coefficient C allows us to take into account a possible drift of the surfaces due to mechanical fluctuations, temperature fluctuations, vibrations...

2.3.5 Homeotropic alignment of the lamellar mesophases in SFA

Usually, as lamellar phases are very viscous, we let two days to the experiment to equilibrate after the sample is introduced in the SFA chamber. Then two weeks are necessary to obtain an homeotropic alignment (see Figure 2.7) of the membranes, that is membranes aligned parallel to the confining mica surfaces. The alignment was achieved by performing slow movement of the surfaces back and forth over separations of several micrometers. This method, equivalent to shearing the liquid crystal is often used to produce homeotropic alignment in lamellar systems. The system was then allowed to equilibrate for at least 24 hours at a separation of a few micrometers. As already

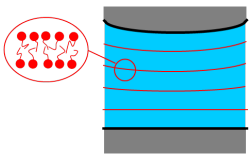

Figure 2.7: Homeotropic alignment of the lamellae (red) between the two mica surfaces (grey).

mentioned in the Section 2.3.1, the geometry of crossed cylinders of radii R is equivalent

to the geometry of a sphere of radius R against a plane. So in a confined medium of non-uniform thickness, there is a conflict between the homeotropic alignment and the need for a constant layer spacing: as a result defects must arise. Thus for a wedge-shaped geometry, an array of edge dislocation loops is expected (Figure 2.8). Dislocations are characterized by their Burgers vector (see Figure 2.9).

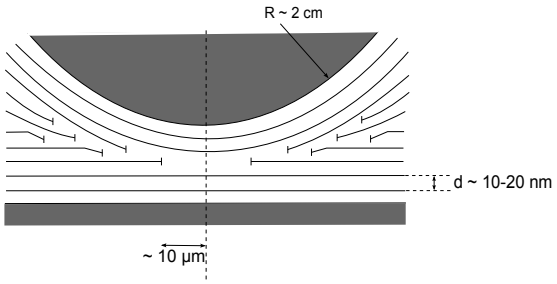

Figure 2.8: The conflict between the homeotropic alignment and the need for a constant layer spacing gives rise to the formation of an array of edge dislocation loops.

(a) (b)

Figure 2.9: Edge dislocations of Burgers vector $b = 1$ (Figure a) and $b = 2$ (Figure b).

Chapter 3

Experimental results

1 Introduction

In the following sections, the experimental results concerning four samples are presented. The samples are located in the phase diagram as presented in the Figure 3.1 below:

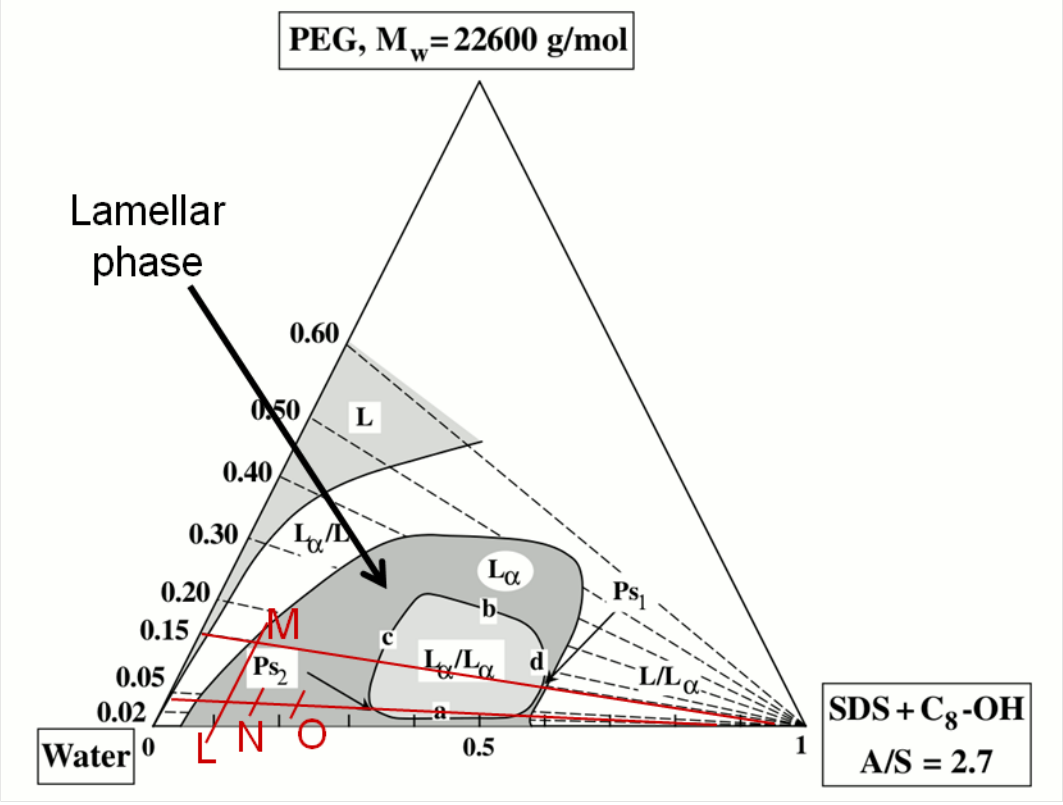

Figure 3.1

Samples L and M

The samples denoted by the letters L and M are situated on an axis parallel to the water/PEG axis, thus their membrane mass fraction is the same: $\Phi_{memb} = 10$ wt %. The sample L does not contain any polymer and the sample M contains 15 wt % polymer in water, that is to say $C_p = 15$ wt %.

These samples are located in the dilute part of the phase diagram and are thus less viscous than the more concentrated mesophases. This is why we started the SFA experiments on these samples, to understand how we need to proceed to perform an SFA experiment. These experiments allow us to investigate the effect of the polymer concentration on the elastic properties of the lamellar mesophases.

Samples N and O

The samples denoted by the letters N and O are situated on the same dilution line, thus their polymer concentration in water is the same: $C_p = 3.8$ wt %. The sample N contains 15 wt % of membrane, $\Phi_{memb} = 15$ wt % and the sample O contains 20 wt % of membrane, $\Phi_{memb} = 20$ wt %.

These samples are located on the dilution line leading to the critical point P_{s2}. The aim is to progressively approach P_{s2} and the biphasic L_α/L_α region, and thus to observe the influence of the critical point on the force profiles.

We sum up the locations:

$$L\begin{pmatrix}\Phi_{memb} = 10 \text{ wt \%}\\ C_p = 0 \text{ wt \%}\end{pmatrix} \qquad M\begin{pmatrix}\Phi_{memb} = 10 \text{ wt \%}\\ C_p = 15 \text{ wt \%}\end{pmatrix}$$

$$N\begin{pmatrix}\Phi_{memb} = 15 \text{ wt \%}\\ C_p = 3.8 \text{ wt \%}\end{pmatrix} \qquad O\begin{pmatrix}\Phi_{memb} = 20 \text{ wt \%}\\ C_p = 3.8 \text{ wt \%}\end{pmatrix}$$

Remark

Note that a SFA experiment performed on one sample lasts 6 to 8 weeks. In average, 2 weeks are necesseray to obtain a good homeotropic alignment. The data are then collected over 4 to 6 weeks.

2 What happens when water is replaced by polymer?

In this part, the experimental results concerning samples L and M are presented. Both samples contain $\Phi_{memb} = 10$ wt% of surfactant and cosurfactant. Thus, it will be possible to compare the results between these two samples to get insights into the effect of the polymer concentration in water on the elastic properties of the lamellar phase.

In Figures 3.2 (sample L) and 3.3 (sample M), the intensity scattered by the lamellar mesophases as a function of the scattering wave vector is presented. A series of three Bragg diffraction peaks can be seen. Their positions are in the ratio 1:2:3 indicating a

one-dimensional structure of periodicity $d = 22.8 \pm 0.4$ nm for the lamellar mesophase situated at the point L in the phase diagram and $d = 18.5 \pm 0.5$ nm for the lamellar mesophase situated at the point M in the phase diagram.

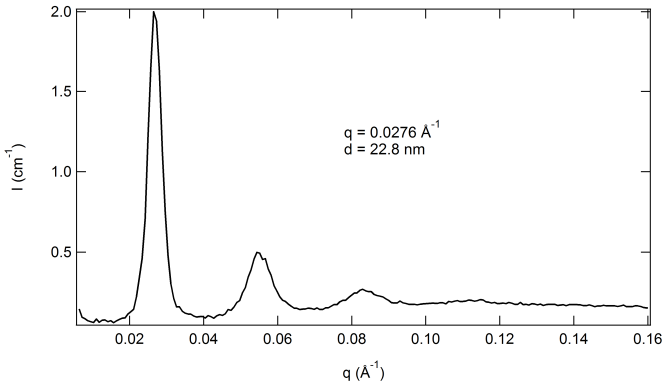

Figure 3.2: Intensity scattered by the lamellar mesophase (sample L) as a function of the wave vector (SAXS). A series of three Bragg diffraction peaks, which positions are in the ratio 1:2:3, allows us to infer the periodicity of the sample: $d = 22.8 \pm 0.4$ nm.

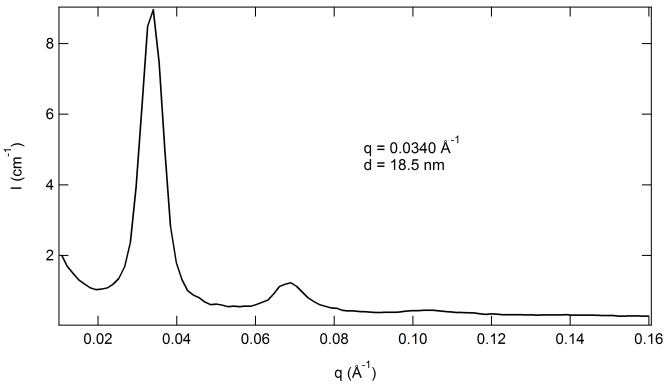

Figure 3.3: Intensity scattered as a function of the wave vector (SAXS, sample M).

The periodicity of lamellar mesophases *without polymer* at different volume fraction has been measured. It is proportional to the inverse of the membrane volume fraction and follows the expected dilution law for a lamellar structure (Figure 3.4). From the slope a membrane thickness δ is extracted : $\delta = 2.4 \pm 0.1$ nm. This result is in good agreement with the value published by M.-F. Ficheux: $\delta = 2.3$ nm in [34].

Concerning the sample with $C_p = 15$ wt%, the membrane thickness is $\delta = 2.1$ nm taken from [34].

Finally, as already observed by Ficheux, the periodicity and the membrane thickness decrease when the polymer concentration increases [34]. The effect is stronger on the periodicity d and may arise from a softening of the electrostatic repulsion due to the presence of the macromolecules between the membranes.

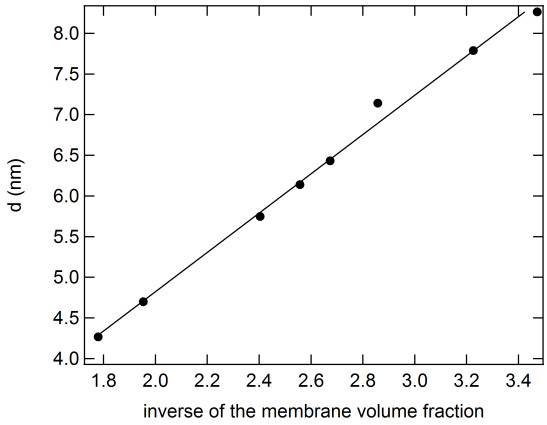

Figure 3.4: Periodicity of several lamellar mesophases (no polymer dissolved in the water layers) as a function of their inverse surfactant and cosurfactant volume fraction. The slope allows us to infer a membrane thickness $\delta = 2.4 \pm 0.1$ nm.

2.1 Force calculation

As presented in the Chapter 2 (Materials and Methods), the two independent quantities measured during an SFA experiment are the surface separation and the piezoelectric device position. In Figure 3.5 is presented an example of a force run measurement performed upon the approach of the surfaces.

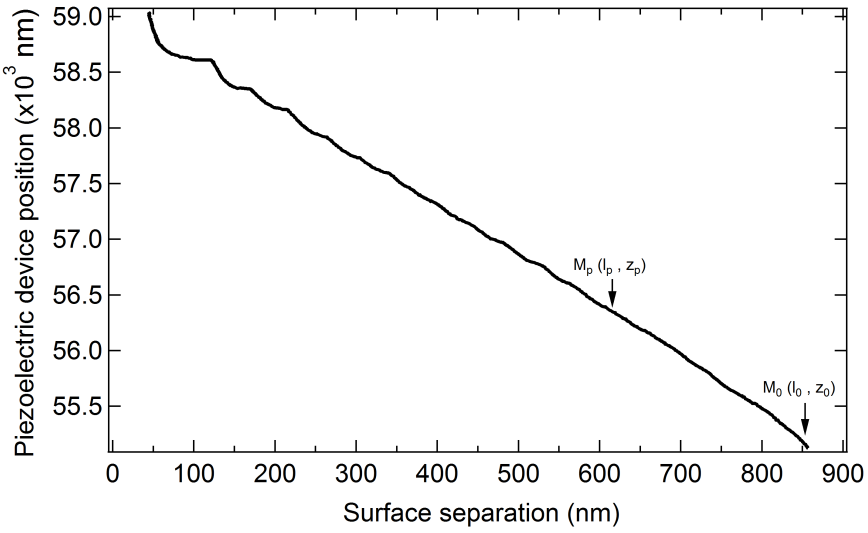

Figure 3.5: Piezoelectric device position as a function of the surface separation. These are the two independent quantities recorded upon a force run measurement (measurement performed upon approach of the surfaces, sample L).

As recalled previously, the calculation of the force is usually done according to the

following equation:

$$F_p = F_0 + K_c(C(z_p - z_0) - (l_0 - l_p))$$

where F_p is the force calculated at the M_p point, F_0 is the unknown force at the starting point M_0, and l_p, l_0, z_p, z_0 are the coordinates defined as follows:

$$M_p \begin{pmatrix} l_p \\ z_p \end{pmatrix} \qquad M_0 \begin{pmatrix} l_0 \\ z_0 \end{pmatrix}$$

where the separation between the two surfaces at the M_p (resp. M_0) point is l_p (resp. l_0) and z_p (resp. z_0) is the piezoelectric device position at M_p (resp. M_0). K_c is the cantilever spring constant. C is the calibration coefficient of the experiment, defined as the slope of the graph far from the contact position:

$$C = \frac{\Delta l}{\Delta z}$$

Far from the contact position, the interaction between the surfaces is considered as negligible, below the sensitivity of the SFA device; this is why the change in the surface separation should be equal to the input displacement of the upper surface (i.e. to the displacement of the piezoelectric device). So C is usually very close to 1 (should be strictly equal to 1 in the absence of any surface drift).

In the example given in Figure 3.5, we observe a straight line (on which oscillations superimpose) which gives $C = 0.23$. Considering that the mesophase has been carefully homeotropically aligned along the mica surfaces for days, that no thermal and mechanical drift of the SFA occurs, the very low value of that apparent calibration suggests that even far from the contact position, some interactions must occur between the surfaces. This observation has been observed in independent measurements on different mesophases in this system as well as in other systems [59]. Therefore, to infer the force from the measured data (response of the surface separation upon a change in the piezoelectric device position, see Figure 3.5), we have proceeded as follows within the framework of two main assumptions:

- the first point M_0 (starting point) is at equilibrium (no fluctuations of the surface separation);
- the total response of the sample represents the total force experienced by the confined system upon a change in the separation between the two surfaces: viscoelasticity, elasticity, plasticity, structural rearrangements...

Under these assumptions, the force, that we call in the following the total force, is calculated as:

$$F_p = F_0 + K_c((z_p - z_0) - (l_0 - l_p)) \tag{3.1}$$

For the first measured point, F_0 is arbitrarily set to zero since the Surface Force Apparatus does not give access to the absolute force.

2.2 Total force as a function of surface separation

In Figure 3.6 and 3.7, total force as a function of surface separation curves are presented (sample L). All the measurements presented were performed upon approach of the surfaces; the measurements were performed by successive compression/dilation cycles. The force measurements performed upon separation of the surfaces exhibit a different behavior and some effort to interpret them need to be done. Thus they are not presented here.

The piezoelectric device is controlled to move the upper surface by steps. So the speeds indicated are those of the upper surface displacement. Steps of 3 to 5 nm every 15 s allow us to achieve reliable measurements in a reasonable time. A run beginning around 850 nm lasts typically 4 hours.

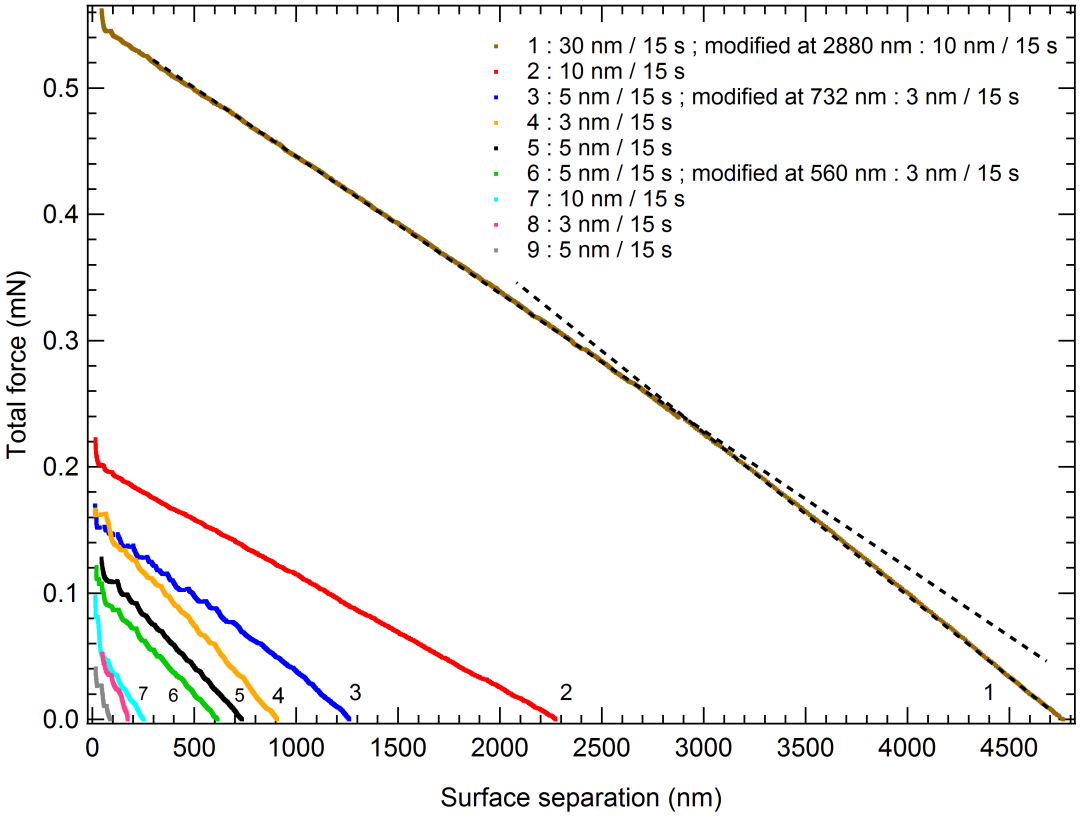

Figure 3.6: Total force as a function of surface separation for several measurements performed upon approach of the surfaces (sample L). For measurement 1, the dashed lines indicate the change in the background slope when the speed is decreased.

2.2.1 Observations

Several observations can be made :

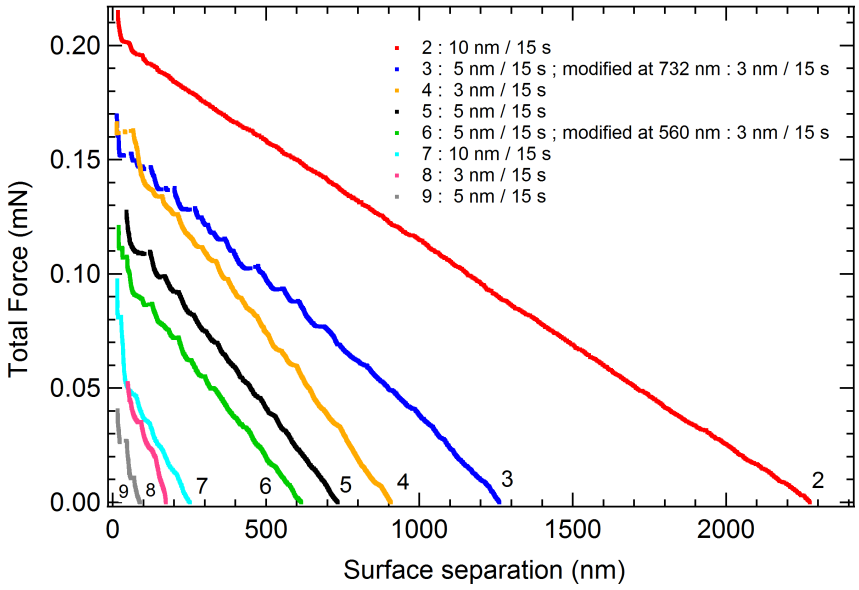

Figure 3.7: Total force - separation profiles (enlargement of Figure 3.6, sample L).

- the force profiles are constituted of a linear background on which oscillations superimpose;

- the slope of the linear background is sensitive to the initial surface separation: the slope increases when the initial starting surface separation decreases (compare for example runs 3, 5 and 9 that were performed at the same speed);

- the slope of the linear background is also sensitive to the speed. Indeed for the run 1 there is a break in the slope when the speed is changed: the slope diminishes when the speed decreases;

- the measurements performed at a speed superior to 5 nm/15 s show less oscillations;

- strikingly, if we consider two runs, for one given surface separation, we observe that the forces are not equal. This is not just a problem of offset since the slope is different.

The same behavior is observed for sample M, the experimental curves are presented in the appendix (end of the section).

Long-range interactions are obviously at the origin of the linear background. The slope of the linear background is sensitive to the speed, indicating that it may arise from the viscoelasticity of the samples. This is why we investigate the slope of the linear background by introducing the *sample stiffness* in the next section.

2.2.2 Stiffness of the sample

In this section, we present two "models" to calculate the sample stiffness.

Toy model 1

The sample stiffness can be deduced from a quick calculation. Upon the assumption that the measurements are performed very slowly (quasi-statics), the balance of the forces gives

$$F_p = F'_p$$

where F_p (resp. F'_p) is the force applied by the cantilever on the sample (resp. the force applied by the sample on the cantilever). Thus

$$F_0 + K_c((z_p - z_0) - (l_0 - l_p)) = F'_0 + K_p(l_0 - l_p)$$

where K_p is the stiffness of the sample at the M_p point. Setting $M_p = M_0$ in the above equation, we get

$$F_0 = F'_0.$$

Therefore

$$K_c((z_p - z_0) - (l_0 - l_p)) = K_p(l_0 - l_p)$$

and we finally obtain

$$K_p = K_c(\frac{z_p - z_0}{l_0 - l_p} - 1). \tag{3.2}$$

A plot of K_p as a function of the separation is presented in Figure 3.8 for the measurement 5.

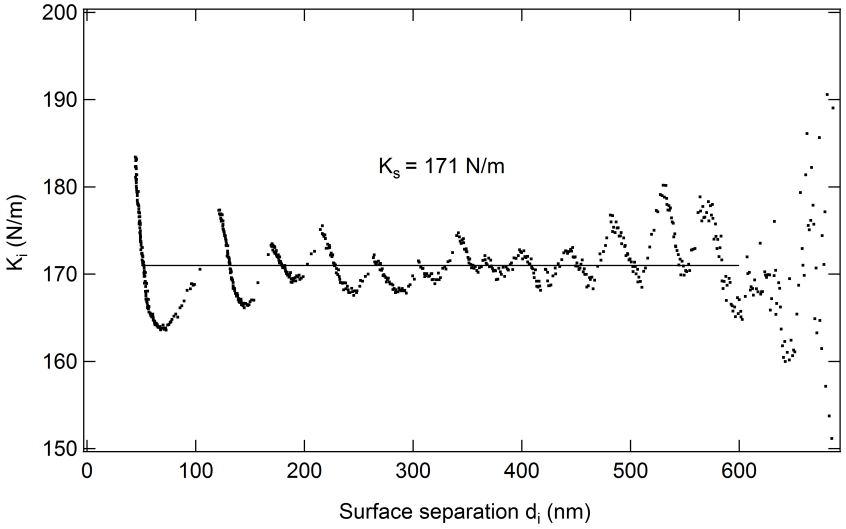

Figure 3.8: Stiffness K_p calculated for each point M_p according to equation (3.2) for the run 5 (sample L). Note that K_p oscillates around a constant value $K_s = 171$ N/m.

The stiffness of the lamellar mesophase is oscillating around a constant value. If we denote K_s the mean stiffness of the sample, we get $K_s = 171$ N/m for the force run 5 (sample L).

Finally, we can compare the sample stiffnesses that we calculate for each force run measurement (see Figure 3.10 and following) for one given sample. More interestingly, this give us a criterion to compare different samples. Sample M exhibits a lower sample stiffness (range 50 to 200 N/m, see the Figure 3.27 in the appendix, end of the section) than sample L (range 100 to 500 N/m), which seems consistent with the macroscopic observation: the sample M is more liquid and less viscoelastic than sample L. The sample stiffness account thus for an effective viscosity on the cantilever and on the surfaces.

If we express the force at the M_p point as a linear decreasing function $F_p = F_0 + \beta(l_0 - l_p)$, describing the linear background only, by identification with (3.1), we get

$$z_p - z_0 = (l_0 - l_p)\big(1 + \frac{\beta}{K_c}\big) \tag{3.3}$$

and finally $K_p = K_c(\frac{z_p - z_0}{l_0 - l_p} - 1) = \beta$, which is checked by measuring the slope.

Toy model 2

Let us now check that the measurements are performed slowly enough so that the system is at the equilibrium at any step of the force run measurement. In the previous model, the system has been described only with stiffnesses. But a real physical system needs to be described by a combination of both stiffnesses and dampers. Figure 3.9a represents a scheme of the system constituted of the confined mesophase between the two surfaces, the cantilever, and the bulk sample. K_s and C_s are respectively the stiffness and the damper of the confined sample, K_c is the cantilever stiffness, C_m is the damper of the surrounding mesophase (bulk).

Now the balance of the forces is written as

$$K_c((z_p - z_0) - (l_0 - l_p)) + \text{viscous forces} = K_p(l_0 - l_p)$$

where the viscous forces result from both C_s and C_m. Indeed, when the upper surface moves by steps (5 nm step for illustration, see Figure 3.9b), as K_s is superior to K_c (by a factor of 3 to 10), the displacement is mainly transferred to the lower surface. Then, time is required for attaining a new equilibrium position by the opposite (lower) surface since it results from a balance between both springs, which equilibrate through dampers C_s and C_m.

If each measurement *is recorded before the surface separation equilibrium is reached*, one must introduce a deviation ϵ_p (positive a priori) to the surface separation l_p in the expression of the forces. This way to take into account the viscous forces is not rigourous, we should in principle express the forces resulting from the dampers. This would introduce additional unknown this is why, for the sake of simplicity, we take into

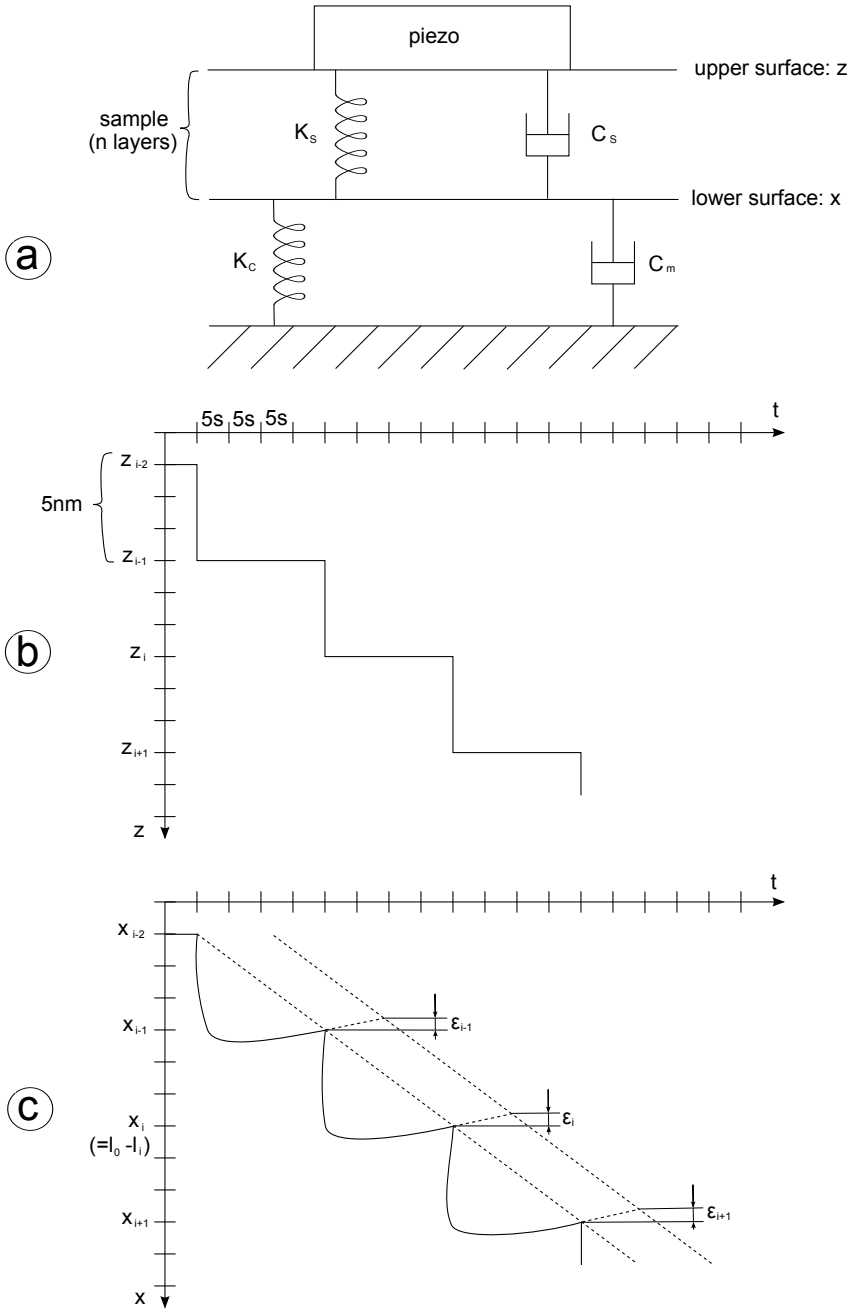

Figure 3.9: a- Scheme representing the considered dynamical system: K_c is the cantilever stiffness, K_s and C_s are the confined sample stiffness and damper respectively and K_m is the damper due to the surrounding bulk sample. b- Scheme representing the input displacement steps of the upper surface (linked to the piezoelectric device) as a function of time. c- Scheme representing the response of the lower surface in position as a function of time.

account the viscous forces by introducing the deviation ϵ_p. Let us calculate the force at the M_p point, by summing all the additional deformations:

$$
\begin{array}{ll}
M_0 & K_c((0-z_0)-(l_0-0)) = K_s(l_0-0) \\
(\ldots) & \\
M_i & K_c((z_i-z_{i-1})-(l_{i-1}-l_i+\epsilon_i)) = K_s(l_{i-1}-l_i+\epsilon_i) \\
M_{i+1} & K_c((z_{i+1}-z_i)-(l_i-l_{i+1}+\epsilon_{i+1})) = K_s(l_i-l_{i+1}+\epsilon_{i+1}) \\
(\ldots) & \\
M_p & K_c((z_p-z_{p-1})-(l_{p-1}-l_p+\epsilon_p)) = K_s(l_{p-1}-l_p+\epsilon_p) \\
\multicolumn{2}{c}{- -} \\
\multicolumn{2}{c}{K_c((z_p-z_0)-(l_0-l_p+\sum_{i=1}^{p}\epsilon_i)) = K_s(l_0-l_p+\sum_{i=1}^{p}\epsilon_i)}
\end{array}
$$

Note that we have replaced K_i by its average K_s. Hence

$$K_s = K_c(\frac{z_p-z_0}{l_0-l_p+\sum_{i=1}^{p}\epsilon_i}-1) = K_c\left(\frac{z_p-z_0}{(l_0-l_p)(1+\frac{\sum_{i=1}^{p}\epsilon_i}{l_0-l_p})}-1\right)$$

and with $\sum_{i=1}^{p}\epsilon_i << l_0-l_p$ we get

$$K_s \simeq K_c(\frac{z_p-z_0}{l_0-l_p}-1) - K_c\frac{\sum_{i=1}^{p}\epsilon_i(z_p-z_0)}{(l_0-l_p)^2}.$$

Let us take $\epsilon_i \simeq$ constant $\simeq \epsilon$ independent of M_i and l_i, we obtain

$$K_s \simeq K_c(\frac{z_p-z_0}{l_0-l_p}-1) - K_c\frac{p\epsilon(z_p-z_0)}{(l_0-l_p)^2}. \tag{3.4}$$

We recognise equation (3.2) with an additional term in the right-hand side. Let us note $K_s' = -K_c\frac{p\epsilon(z_p-z_0)}{(l_0-l_p)^2}$. Replacing (z_p-z_0) in this expression thanks to equation (3.3), we obtain

$$K_s' = -K_c\frac{p\epsilon(1+\beta/K_c)}{l_0-l_p}. \tag{3.5}$$

K_s' is a constant since we can write $l_0-l_p = p\bar{s}$ where $\bar{s}$ denotes the mean step at which the surfaces get closer. We now that $\bar{s} \simeq s_{\text{piezo}}C$, where s_{piezo} is the step achieved by the piezoelectric device and C the "calibration coefficient" (see Section 3.1), thus

$$K_s' \simeq -\frac{\epsilon(K_c+\beta)}{s_{\text{piezo}}C}. \tag{3.6}$$

To estimate ϵ, let us assume that the sample does not have any stiffness, that is to say $K_c(\frac{z_p-z_0}{l_0-l_p}-1) = K_c\frac{p\epsilon(z_p-z_0)}{(l_0-l_p)^2}$. This will give us the *maximum* deviation ϵ:

$$K_c(\frac{z_p-z_0}{l_0-l_p}-1) = \beta = \frac{\epsilon(K_c/\beta+1)\beta}{s_{\text{piezo}}C}$$

$$\text{that is} \qquad 1 = \frac{\epsilon(K_c/\beta+1)}{s_{\text{piezo}}C}$$

Let us calculate the deviations for measurements 5 and 9, this will give us the maximum range of deviations for the measurements 5, 6, 7, 8 and 9, which are the measurements that we consider in the following analysis. For measurement 5, we have $\beta = 3.4\,K_c$, $s_{\text{piezo}} = 5$ nm, $C = 0.23$, so we get $\epsilon = 0.9$ nm. For measurement 9, we have $\beta = 10\,K_c$, $s_{\text{piezo}} = 5$ nm, $C = 0.04$, we get $\epsilon = 0.2$ nm. These deviations are the maximum possible deviations and they are weak. We can thus make sure that the measurements 5, 6, 7, 8 and 9 that have been used for the following analysis are performed at the thermodynamic equilibrium. On the contrary, we calculate $\epsilon = 6.3$ nm for measurement 1 ($\beta = 3\,K_c$, $s_{\text{piezo}} = 30$ nm, $C = 0.28$), which strengthens our opinion in the fact that this measurement is not performed at the equilibrium.

Note that equation (3.4) shows that if the measurements are performed too quickly, the stiffness should appear enhanced. This is in agreement with the experimental observation.

Finally, this second model provides a mean to check that our measurements are performed at thermodynamic equilibrium, which is crucial for the following analysis (extraction of the elastic compressibility modulus).

Evolution of K_s with the initial surface separation

We examine now qualitatively the evolution of K_s as a function of the initial surface separation in Figure 3.10. First of all we see that the stiffness of the sample is always

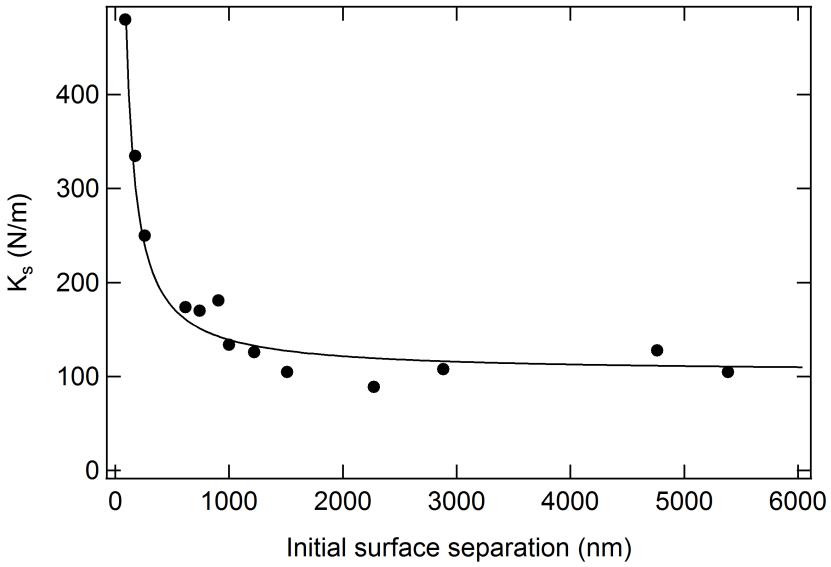

Figure 3.10: Mean stiffness of the sample K_s as a function of the initial surface separation l_0 for several force run measurements (sample L). Each point corresponds to a run presented in Figure 3.6, and additional points correspond to runs that are not presented.

bigger than the cantilever stiffness ($K_c = 50$ N/m). The sample stiffness seems to

behave as a power law. Regarding the total force versus separation profiles, which remind the force curve of a spring, it is tempting to fit the data with

$$K_s = K_s^\infty + \frac{A}{l_0}.$$

We get

$$K_s^\infty = 104 \pm 7 \text{ N/m}$$
$$A = (35 \pm 2)10^{-6} \text{ N}.$$

The result $K_s - K_s^\infty = \frac{A}{l_0}$ could be naively interpreted by assuming that the stack of membranes is equivalent to a series of springs, whose stiffnesses k_m are equal and whose lengths correspond to the sample period d. Thus,

$$\frac{1}{K_s} = \sum_{p=1}^{n} \frac{1}{k_m} = \frac{n}{k_m}.$$

With $n = \frac{l_0}{d}$, we get

$$K_s = \frac{k_m}{n} = \frac{k_m d}{l_0}.$$

So $K_s \equiv K_s - K_s^\infty$ would be related to l_0 by a -1 power law. We could write

$$(K_s - K_s^\infty) l_0 = k_m d = \text{constant} = A$$

with $A = (35 \pm 2)10^{-6}$ N, we would finally deduce the stiffness of a membrane:

$$k_m = (1.6 \pm 0.2)10^3 \text{ N/m}.$$

But there is little chance that this approach is correct: what would be the meaning of K_s^∞? How could we prove the dependence of K_s with $1/l_0$ regarding the expressions that we have obtained for K_s?

Finally, we should simply keep in mind that we observe a dependence of the slope of the linear background with the initial surface separation, that is to say with the initial number of layers confined in the stack. This effect could be related to the dislocation array, that may contribute to the linear background. If we consider one total force curve, the fact that the stiffness of the sample remains constant in the course of the measurement, while some bilayers are expelled, may show that the dislocations contribute to the stiffness of the sample. If we consider that the stack is equivalent to a series of springs of equivalent stiffnesses and lengths, this would mean that the dislocations contribute to the stiffness with the same weight as a bilayer from the stack. Of course this picture is certainly too simplistic, but it gives an idea of what may happen.

2.2.3 Conclusion

In conclusion, we have found a criterion to check that the measurements are performed at the thermodynamic equilibrium. Note that equation (3.4) shows that if the measurements are performed too quickly, the stiffness should appear enhanced, which is certainly the case for the measurements performed from far (above 1500 nm) that we do not take into account in the following. Concerning the other measurements (3 to 9), we have shown that the maximum deviation is small and that the thermodynamic equilibrium is reached.

Eventually, the slope of the linear background is sensitive to the speed which reveals a viscoelastic behavior. But it appears also dependent from the initial surface separation, which may be explained by considering a contribution of the dislocation array that forms in the course of the force run measurement.

Note that a similar behavior has been observed for sample M, the experimental curves are presented in the end of the section.

2.3 Elastic behavior

To eliminate the contribution of the long-range interactions, the linear background has been subtracted from the total force profile. By doing this, the resulting force profiles superimpose on a master curve. The resulting force-distance profile is shown in Figure 3.11 for sample L and in Figure 3.12 for sample M. Concerning sample M, note that the parabolae minima have been set arbitrarily to zero in force because different runs have revealed some scatter in the absolute force values, especially for the second and third oscillations as shown in Figure 3.13.

2.3.1 Observations

Several observations can be made about this force-distance profiles (Figures 3.11 and 3.12):

- the force profile is oscillatory and constituted of regular oscillations;
- the force profile is discrete due to mechanical instability of the cantilever (see Chapter 2 (Materials and Methods));
- in Figure 3.11, the oscillations superimpose on an attractive background below 300 nm, which turns to be repulsive below about 20 nm;
- the amplitudes of the oscillations increase when the surface separation decreases;
- the minima between two consecutive oscillations are separated in average by a distance equal to twice the periodicity of the sample as measured by X-rays.

All these observations show that the extracted force-distance profiles exhibit classical features of lamellar phase force profiles reported in the literature in other systems

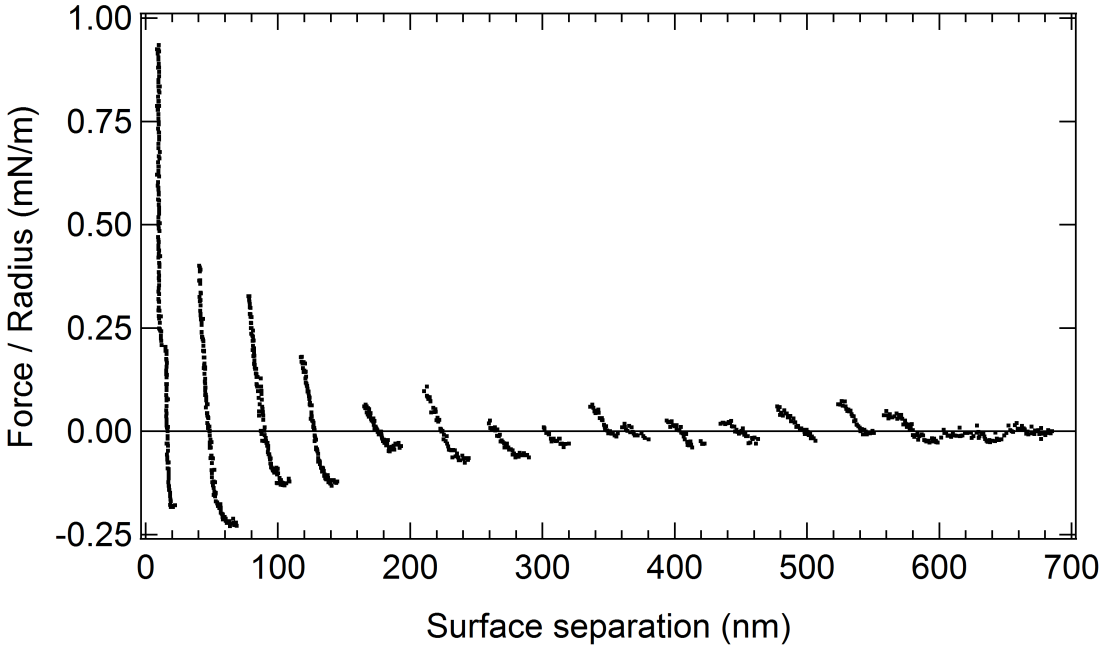

Figure 3.11: Force F (normalized by the mean radius of curvature R of the surfaces), as a function of surface separation for the lamellar mesophase located at the point L in the phase diagram.

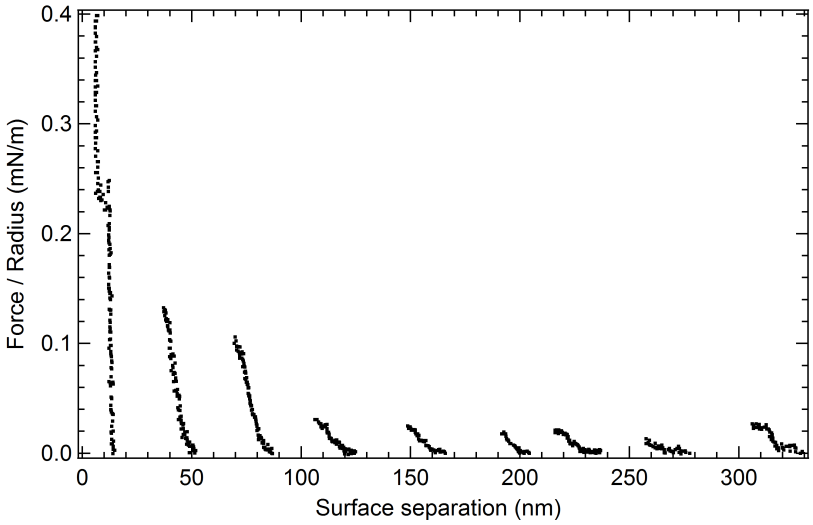

Figure 3.12: Force F (normalized by the mean radius of curvature R of the surfaces), as a function of surface separation for the lamellar mesophase located at the point M in the phase diagram.

[61, 84, 63, 83, 3, 40]. As we will demonstrate below (see Section 2.3.2) the force-distance profiles are indeed constituted of a set of parabolae, only the half of them is

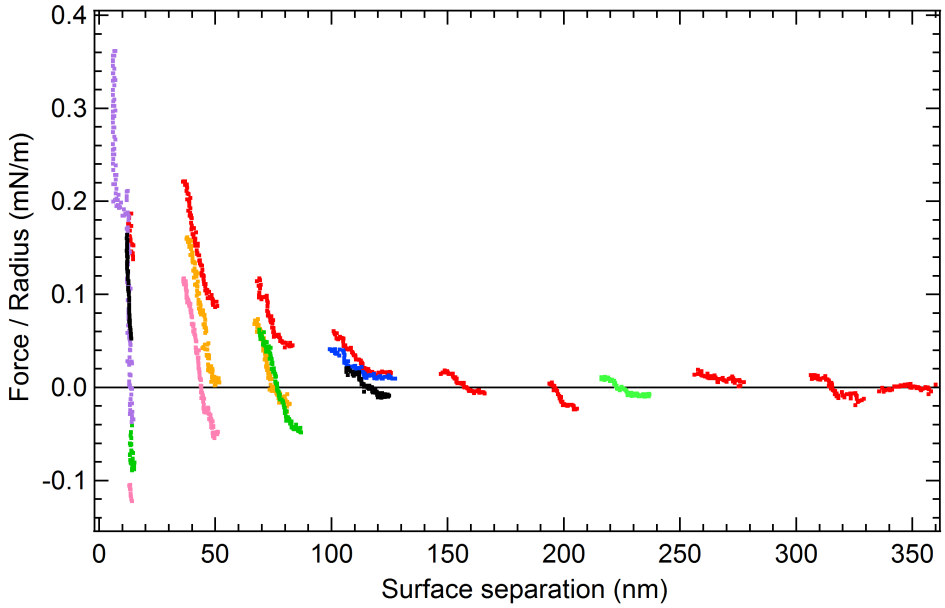

Figure 3.13: Force F (normalized by the mean radius of curvature R of the surfaces), as a function of surface separation (sample M). The colors show different force run measurements.

measured because of the mechanical instability of the cantilever.

The force profiles provide information about the elastic properties of the lamellar phase as well as about its structural rearrangements. We focus now on the elastic behavior and we postpone the study of the structural rearrangements to the section 2.4.

2.3.2 Framework

The elastic compressibility modulus $\bar{B}$ at constant chemical potential is of great importance (as presented in the Chapter 1 (Introduction)) since it is related to the intermembrane interaction potential V :

$$\bar{B} = d\frac{\mathrm{d}^2 V}{\mathrm{d}^2 \bar{d}}$$

where $\bar{d}$ is the intermembrane separation and d the period of the sample.

The method to extract the elastic compressibility modulus of the system from the force-distance profile is now presented. For further details, one may refer to reference [84].

By assuming that the stack of membranes is equivalent to a series of springs - whose stiffnesses are all equal and depend on the intermembrane interaction, and whose lengths correspond to the sample period - the lamellar structure experiences an elastic stress upon approach or separation of the confining surfaces. For a layered system of thickness

l_n at zero stress (l_n is an integral multiple of d), the corresponding elastic energy per unit of surface has a parabolic shape centered around l_n:

$$E = \frac{1}{2}\bar{B}\frac{\Delta {l_n}^2}{l_n}$$

where

$$\Delta l_n = l_n - l$$

and l is the surface separation. The minima of the parabolae correspond to the l_n positions; the inwards jumps correspond to positions at which two neighbouring parabolae would intersect and are denoted l_n^i. Using the Derjaguin approximation (the long-range interactions have been removed), the elastic compressibility modulus $\bar{B}$ and the measured force F are related by

$$(F - F_n)\frac{l_n}{\pi R} = \bar{B}\Delta {l_n}^2 \tag{3.7}$$

where F_n are the forces at the minima l_n.

Before going on with the extraction of the elastic compressibility modulus from the shape of the parabolae, it is crucial to check that the measurements were performed at the thermodynamic equilibrium.

2.3.3 Thermodynamic equilibrium

In a set of intersecting parabolae, the minima l_n are regularly spaced as well as the inwards jump positions l_n^i according to the relation:

$$l_n = nd$$

$$l_n^i = \sqrt{n(n-b)}d$$

where b is the Burgers vector of the dislocation and n is the number of layers confined in the stack at the minimum of each parabola. For each oscillation, the positions of the minima l_n are plotted against $n-2$ (Figure 3.14) since the last two bilayers that remain between the surfaces have usually a reduced periodicity [84] (see the following paragraph); and those of the inward jumps against $\sqrt{n(n-2)}$ since $b = 2$ (Figure 3.15). The solid lines are the best fits to the data:

$$l_n = (20 \pm 2) + (21.3 \pm 0.1)(n-2)$$

$$l_n^i = (-20 \pm 3) + (21.0 \pm 0.2)\sqrt{n(n-2)}$$

and give a reticular distance $d = 21$ nm in agreement with the periodicity inferred from the SAXS measurement.

The fact that the measured values are so close to the fitted line indicates that the forces are measured at the thermodynamic equilibrium, which confirms that our new

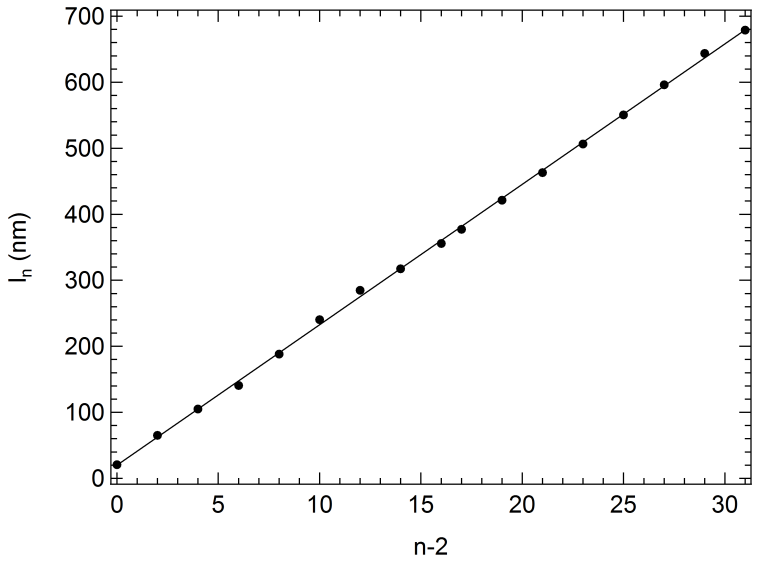

Figure 3.14: For each oscillation (sample L), the positions of the minima l_n are plotted against $n-2$. The solid line is the best fit to the data, giving a reticular distance $d = 21.3 \pm 0.1$ nm in agreement with the X-ray measurement. Note that two points are closer than the other, showing that the Burgers vector is $b = 1$ instead of $b = 2$.

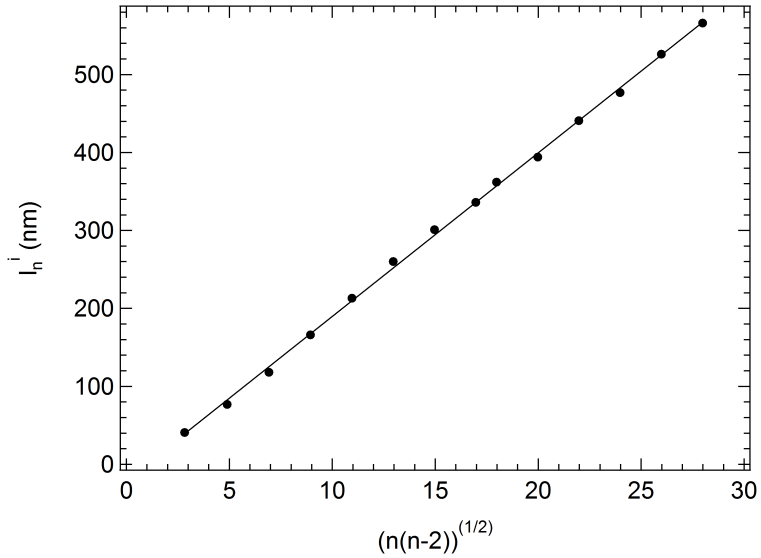

Figure 3.15: For each oscillation (sample L), the positions of the inwards jumps l_n^i are plotted against $\sqrt{n(n-2)}$. The solid line is the best fit to the data, giving a reticular distance $d = 21.0 \pm 0.2$ nm in agreement with the X-ray measurement.

criterion (estimation of the maximum deviation ϵ) is valid. Similarly results concerning the sample M are obtained: the measurements are performed at the thermodynamic equilibrium. The experimental curves are presented in the last subsection.

In Figure 3.14, the ordinate at origin in the fit gives insights into the structure of the confined last two bilayers. Indeed, for these bilayers, if we denote d' their corresponding periodicity, we get: $2d' = 20$ nm which is in agreement with the position of the steric wall at 10 nm, position at which we assume that one bilayer remains. The ordinate at origin obtained with the l_n^i positions is due to the same effect. In Figures 3.16 and 3.17, we suggest a representation of the confined last two bilayers (the measurement of the refractive index is not precise enough to conclude). Note that this give a much smaller periodicity compared to the periodicity of the bulk sample, this is discussed in the last Section 2.4.

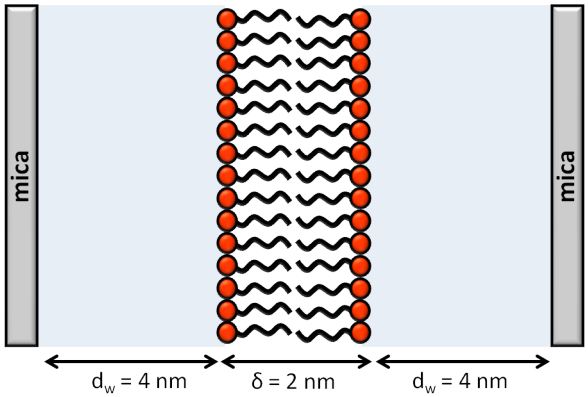

Figure 3.16: Last confined membrane at the steric wall position $l = 10$ nm. Since $\delta = 2$ nm (inferred from the dilution law above), we deduce that the water layers remaining between the membranes and the mica surfaces is $d_w \simeq 4$ nm.

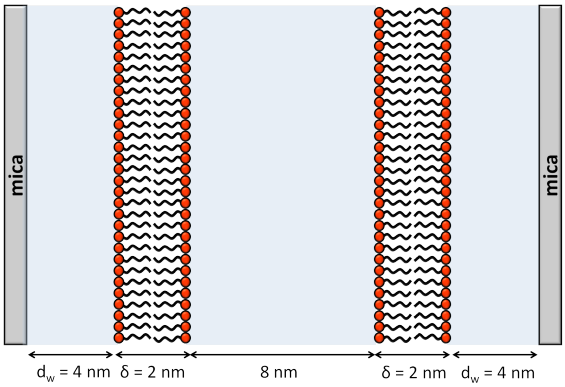

Figure 3.17: First minimum ($l \simeq 20$ nm): two confined membranes whom "periodicity" is reduced.

.

Remark: the thermodynamic equilibrium is valid under the following assumption: by subtracting the linear background, we free ourselves of any speed effect. This is of course not strictly true, since we have seen that the speed has also a little influence on

the oscillations. But in this analysis we see that the measurement are performed slowly enough to make this assumption.

Remark 2: the minima of the parabolae are usually obtained by performing measurements upon separation of the surfaces [61, 84]. In this experiment, the runs out (not presented here, see Chapter 5) show that the minima l_n are very close to the minima of the runs in, this is why we have used these values (see Figure 3.14).

2.3.4 Elastic compressibility modulus

By plotting the relevant quantities as indicated in equation (3.7) the elastic compressibility modulus is directly given by the slope of the graph. In Figure 3.18 are presented the results for three different oscillations from different measurements, for sample L.

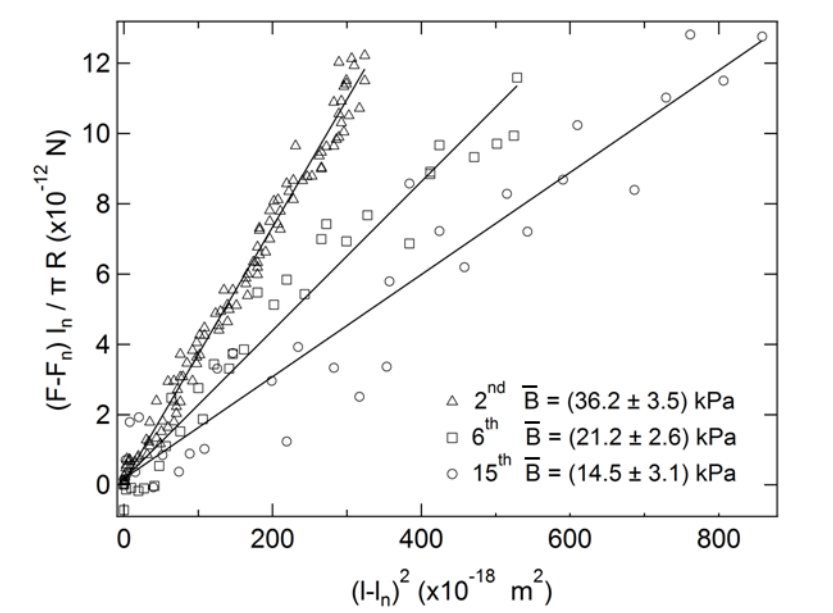

Figure 3.18: The data from the second, sixth and fifteenth oscillations (sample L) plotted according to equation (3.7). The solid lines are for every oscillation the best fit to the data. A value for the elastic compressibility modulus $\bar{B}$ is extracted from each slope.

In Figure 3.19 the value obtained for $\bar{B}$ is plotted against the number of layers confined between the surfaces, for each oscillation and for both samples L and M.

At large separations of the confining walls, the magnitude of the elastic compressibility modulus inferred from the oscillations of high rank ($n > 10$) appears to be constant: $\bar{B} = (16.6 \pm 2.8)$ kPa for sample L and $\bar{B} = (6.4 \pm 1.7)$ kPa for sample M. These values will be considered as the bulk values of the elastic compressibility modulus of these lamellar mesophases.

For sample L, its magnitude will be interpreted as due to the electrostatic interactions between the membranes. Concerning sample L, its magnitude will thus be

interpreted as due to the electrostatic interactions between the membranes as well, on which an attraction due to the polymer superimposes (see Chapter 4).

At smaller separations, the magnitude of $\bar{B}$ increases rapidly as the confinement of the lamellar structure becomes more pronounced. Thus within the range of the first four oscillations ($n < 8$), the value of $\bar{B}$ increases by a factor 3. This rapid increase has been observed in other systems [61] and is interpreted as an enhancement of the electrostatic repulsion: the restriction of the undulation fluctuations of the membranes in the vicinity of hard confining walls gives rise to a better localized and well-defined charge distribution [55].

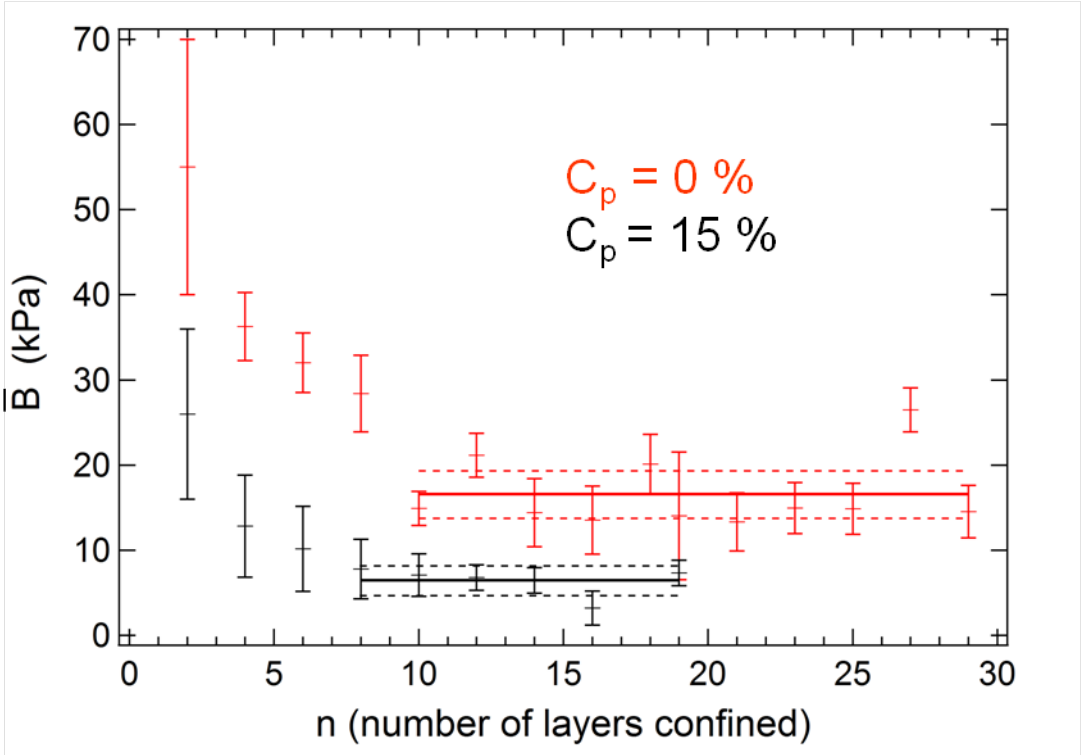

Figure 3.19: Plot of the elastic compressibility modulus inferred from each oscillation as a function of the number of layers confined, for sample L (red) and sample M (black).

2.4 Defects and Burgers vector

In Figures 3.11 and 3.12, the minima of the parabolae are separated by a distance equal to two times the period. This means that upon the approach of the surfaces, the bilayers are expelled two by two and the Burgers vector of the dislocations is equal to two ($b = 2$) for both mesophases.

Sample L

We note an exception for the jump between the tenth and ninth oscillations, the Burgers vector is equal to one.

For the last oscillation, two bilayers remain confined between the surfaces. One of them is expelled when the separation changes from 16 nm to 10 nm. This transition does not seem clearly discrete since no true unstable points are measured. Then the force increases and the last bilayer remains confined, the force has to be increased a lot to break it. We attribute this transition to a likely complex process, hemifusion for instance (see [48]).

We report now some rare occurrences in the behavior. The black curve of Figure 3.20 is the force profile already presented above, which is an average of several very reproducible measurements. However, for some peculiar inward runs, we have observed interesting phenomena such as shown by the red curve in Figure 3.20. This red curve exhibits some irregularities:

- the third and fifth oscillations exhibit very small magnitude and the inward jumps occur before the expected value l_n^i: this is probably due to some kinetic energy that the system would have stored;

- the second and fourth oscillations are deformed: they seem to be constituted of two different parts, the deformation appears in the middle of the oscillation;

- during the jump from the second to the next oscillation, the elastic stress is not completely released and the Burgers vector is equal to one;

- the same phenoma is repeated for the last inward jump (elastic stress and Burgers vector equal to one).

The deformation that occurs around the middle of the oscillation shows that the system tries to nucleate a dislocation of Burgers vector equal to one. As the system has not enough energy, it cannot nucleate the $b = 1$ dislocation and finally rearranges its structure to allow further compression without jumping in. The oscillation is kept along, and eventually the system will nucleate a dislocation of Burgers vector $b = 2$. Obviously Burgers vector $b = 2$ is the most favourable for this lamellar structure. Note that such behavior with deformed oscillations occurs always after oscillations whose magnitude were abnormally small (measurement upon approach of the surfaces), showing that the system tries to use the stored energy to nucleate a $b = 1$ dislocation loop.

For the last oscillations next to the walls of $b = 1$, it shows that the system in this case has chosen an other path to nucleate the dislocations.

In Figure 3.21, we present a measurement with an oscillation of Burgers vector equal to 4. Similarly to the curve presented above, the previous oscillation was not well built. This $b = 4$ oscillation is deformed at a separation corresponding to a Burgers vector $b = 3$. Again, the system has not enough energy to nucleate the $b = 3$ dislocation and finally continues on a $b = 4$ oscillation.

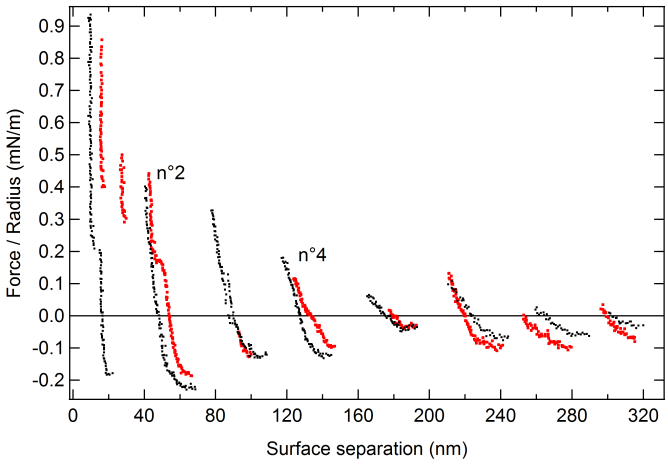

Figure 3.20: Normalized force as a function of the surface separation. The black curve is the force profile presented in Figure 3.11. The red curve exhibits exotic behavior: note the third and fifth oscillations with very small amplitudes; the second and third oscillations are deformed; the Burgers vector $b = 1$ dislocations occuring for the last two jumps.

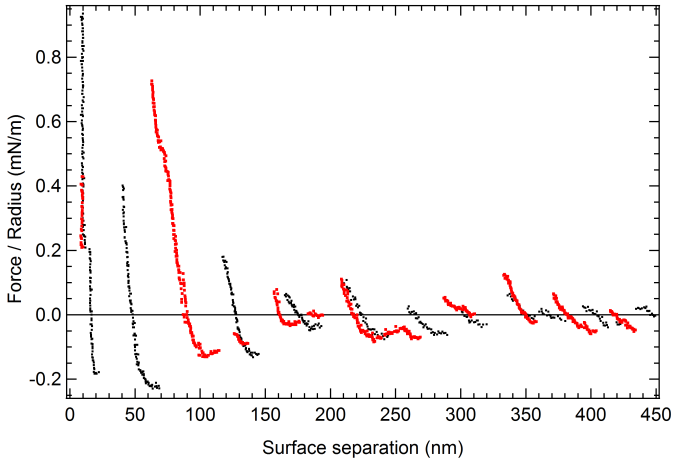

Figure 3.21: Normalized force as a function of the surface separation. The black curve is the force profile presented in Figure 3.11. The red curve exhibits exotic behavior: note the fourth oscillation with very small amplitude; the third oscillation is deformed and $b = 4$.

Sample M

We note an exception for the jump between the ninth and eighth oscillations: $b = 3$.

For the last oscillation, two bilayers remain confined between the surfaces. One of them is expelled when the separation changes from 15 nm to 6 nm. This transition does not seem clearly discrete since no true unstable points are measured. Then the force increases and the last bilayer remains confined, the force has to be increased a

lot to break it. We may attribute this transition to a complex process (hemifusion for instance, see [48]).

In Figure 3.22, three force versus separation profiles are presented. In green we recognise the averaged force profile presented in Figure 3.12. The red curve exhibit a singular transition between the third and second oscillation: no true unstable points are measured (compare to the slope K/R). Certainly this continuous transition can be attributed to a complex process as well (hemifusion). The blue curve is presented as a guide for the eyes: it extends the red curve whose measurement was stopped too early.

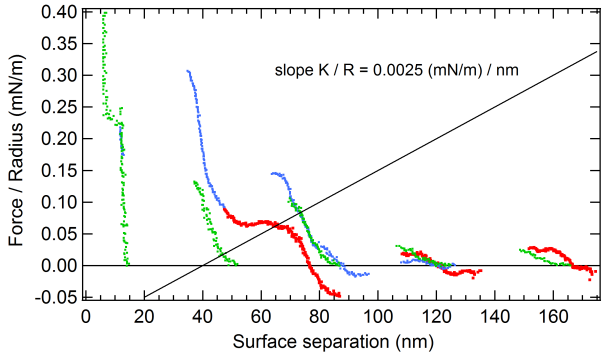

Figure 3.22: Normalized force as a function of the surface separation. The green curve is the averaged force profile presented in Figure 3.12. The red curve exhibit a continuous transition between the third and second oscillation. The blue curve is presented as a guide for the eyes (it extends the red curve whose measurement was stopped too early).

2.5 Appendix: experimental curves for sample M

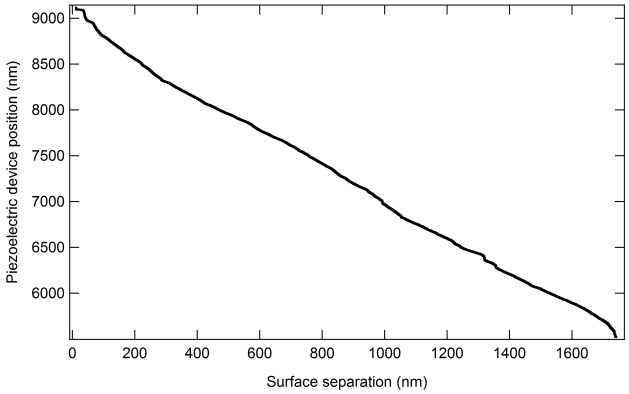

Figure 3.23: Piezoelectric device position as a function of the surface separation. This measurement has been performed upon approach of the surfaces at a speed of 1 nm/15 s. The average slope of this graph gives $C = 0.52$ which shows that there are long-range interactions.

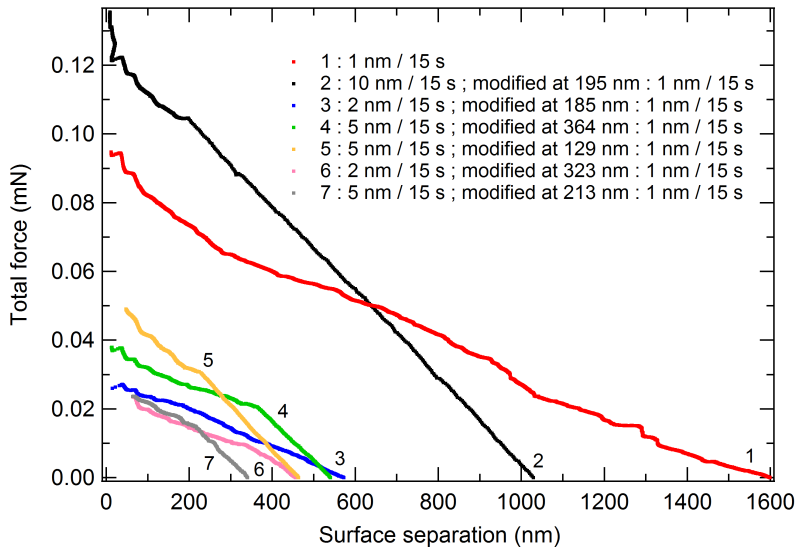

Figure 3.24: Total force as a function of the surface separation for several measurements performed upon approach of the surfaces. Here we show the influence of the speed, which has been modified in the course of the measurement: the slope of the linear background is very sensitive to the speed. Indeed there are breaks in the slopes when the speed is changed (Figure 3.24). The slope decreases when the speed decreases. Note also that the measurements performed at a speed higher than 5 nm/15 s show no oscillation.

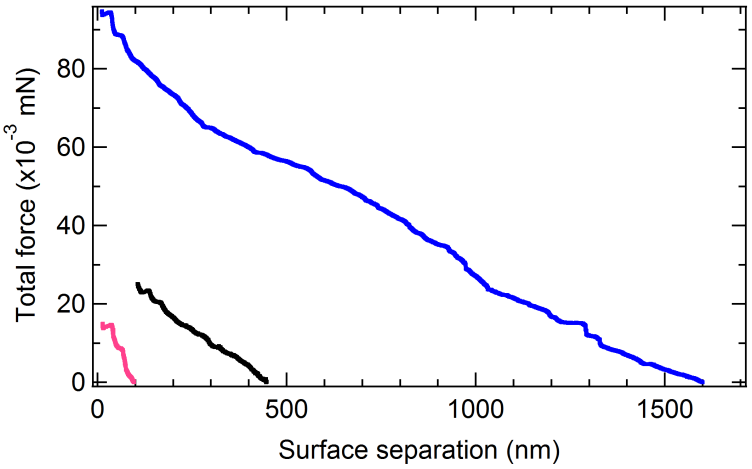

Figure 3.25: Total force as a function of the surface separation for several measurements performed upon approach of the surfaces. Here we show the influence of the initial separation: the slope of the linear background increases when the initial surface separation decreases. These measurements have been performed at 1 nm/15 s.

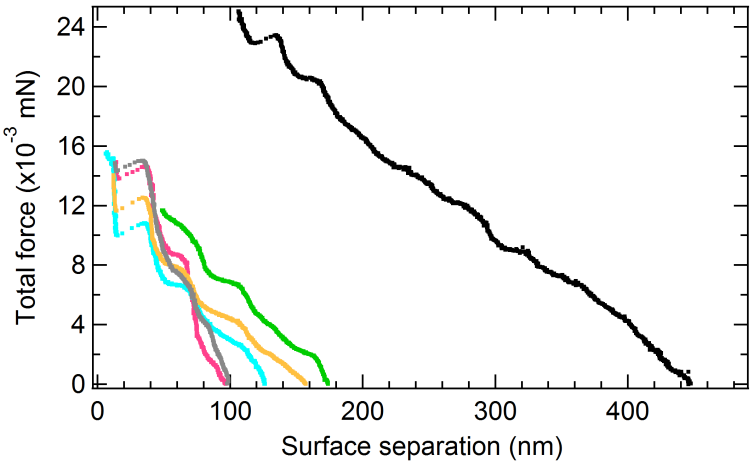

Figure 3.26: Total force as a function of the surface separation for several measurements performed upon approach of the surfaces. Here we show the influence of the initial separation for shorter separations than those presented in Figure 3.25. The slope of the linear background increases when the initial surface separation decreases. These measurements have been performed at 1 nm/15 s. The run 1 starting at 1600 nm seems a little bit irregular: no other run has been performed in this range of separations (since it lasts 15 hours) so maybe the homeotropic alignment is of less good quality. Note that the maximum deviation ϵ for these measurements is very weak: $K_s = 60$ to 200 N/m and $C = 0.5$ to 0.2 so we get for the maximum deviation $\epsilon = 0.3$ to 0.15 nm.

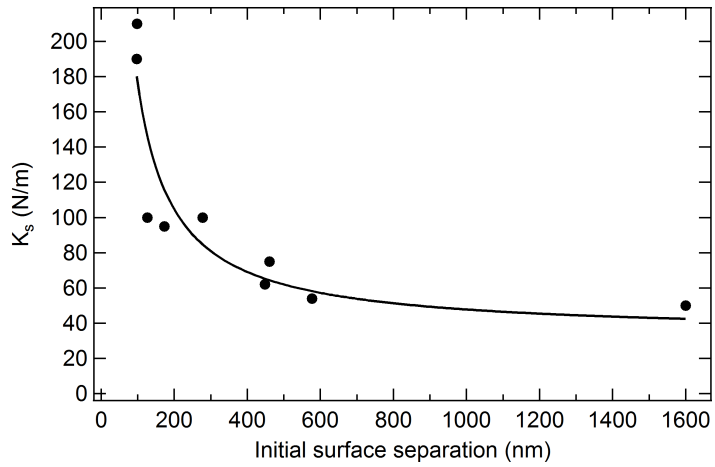

Figure 3.27: Stiffness of the sample K_s as a function of the initial separation l_0.

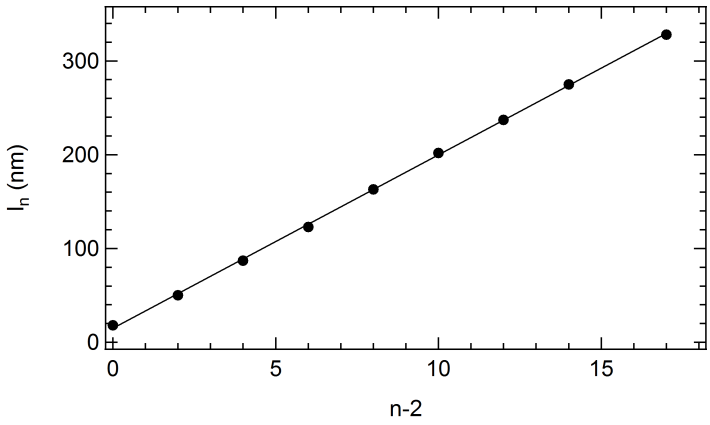

Figure 3.28: For each oscillation, the positions of the minima l_n are plotted against $n-2$. The solid line is the best fit to the data, $l_n = (15 \pm 1) + (18.5 \pm 0.1)(n-2)$, giving a reticular distance 18.5 ± 0.1 nm in agreement with the X-ray measurement.

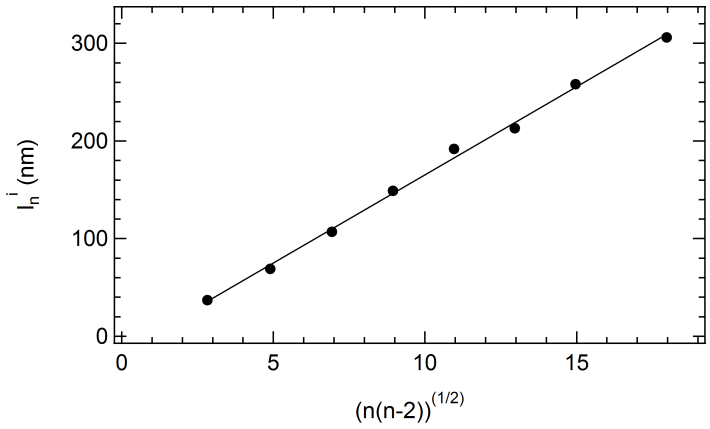

Figure 3.29: For each oscillation, the positions of the inwards jumps l_n^i are plotted against $\sqrt{n(n-2)}$. The solid line is the best fit to the data, $l_n^i = (-15 \pm 5) + (18.1 \pm 0.4)\sqrt{n(n-2)}$, giving a reticular distance 18.1 ± 0.4 nm in agreement with the X-ray measurement.

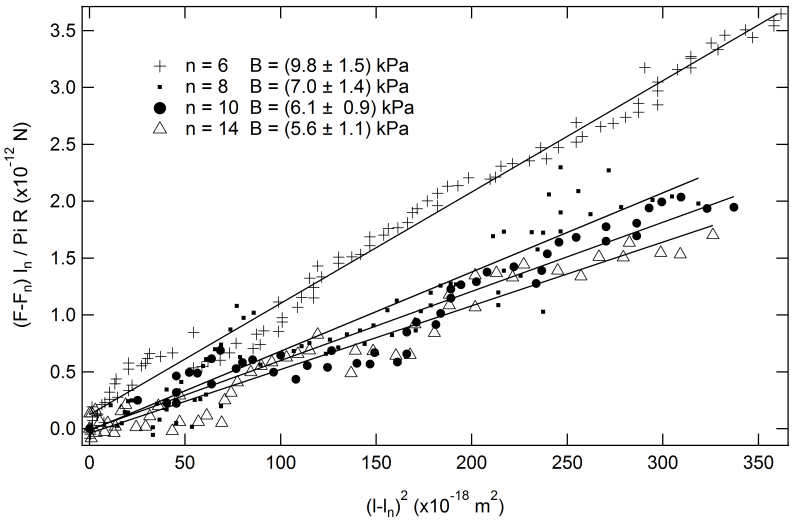

Figure 3.30: The data from a few oscillations plotted according to equation (3.7). The solid lines are the best fit to the data, each slope allows us to extract a value for the elastic compressibility modulus.

3 On the approach of the critical point P_{s2}: avalanches phenomena and large Burgers vectors

In this section, the experimental results concerning samples N and O are presented.

In Figures 3.31 and 3.32, the intensity scattered by the lamellar mesophases situated at respectively N and O in the phase diagram are presented as a function of the wave vector. In Figure 3.31, a series of four Bragg diffraction peaks can be seen. Their positions are in the ratio 1:2:3:4 indicating a one-dimensional structure of periodicity $d = 14.6 \pm 0.1$ nm for sample N. In Figure 3.32, a series of three Bragg diffraction peaks can be seen. Their positions are in the ratio 1:2:3 indicating a one-dimensional structure of periodicity $d = 10.9 \pm 0.1$ nm for sample O.

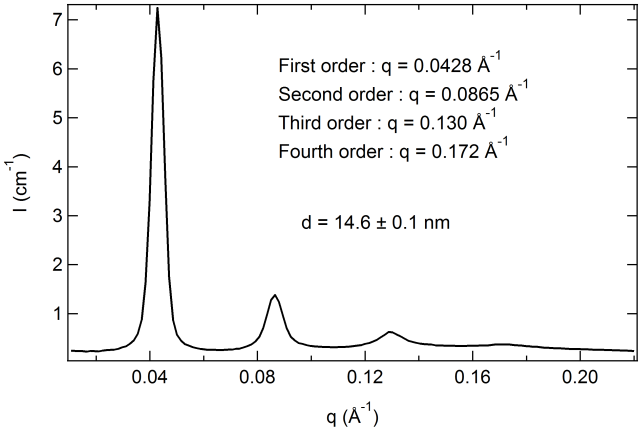

Figure 3.31: Intensity scattered as a function of the wave vector (SAXS).

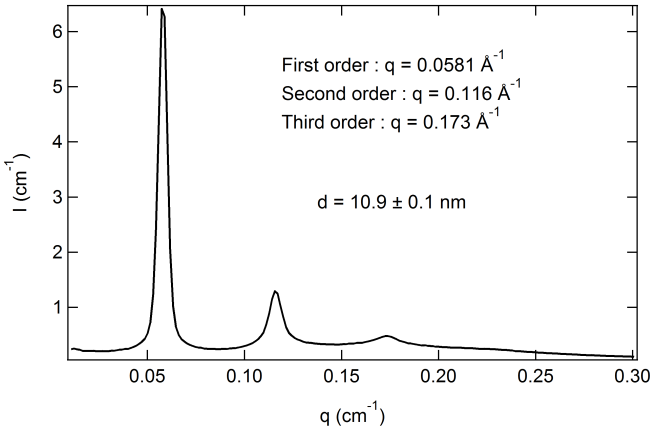

Figure 3.32: Intensity scattered as a function of the wave vector (SAXS).

The periodicity of such lamellar mesophases (same concentration of polymer in the water layers $C_p = 3.8$ wt %) at different membrane volume fraction has been

measured. It is proportional to the inverse of the membrane volume fraction and follows the expected dilution law for a lamellar structure (Figure 3.33). From the slope a membrane thickness δ is extracted: $\delta = 2.1 \pm 0.1$ nm. This result is in good agreement with the value published by M.-F. Ficheux: $\delta = 2.1$ nm [34].

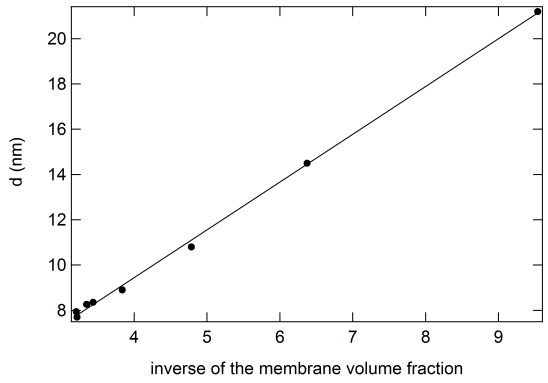

Figure 3.33: Periodicity of several lamellar mesophases as a function of their inverse membrane volume fraction. All the lamellar mesophases have the same amount of polymer in the water layers: $C_p = 3.8$ wt %.

3.1 Total force as a function of surface separation

In Figure 3.34, a measurement performed at a speed of 5 nm/15 s is presented (sample N). The average slope of this graph between 150 nm and 250 nm is $C = 0.030$, which is by an order of magnitude below the values extracted in previous experiments. This shows that the long-range interactions existing in the lamellar mesophase located at the point N in the phase diagram are stronger than for samples L and M. A similar behavior is observed for sample O, the experimental curves are presented in the last section.

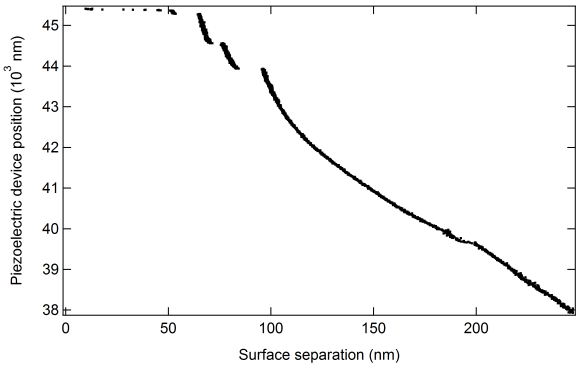

Figure 3.34: Piezoelectric device position as a function of the surface separation (sample N).

3.1.1 Total force

In Figures 3.35 and 3.36, total force versus separation profiles are presented for sample N and O respectively. The measurements were performed upon approach of the surfaces. Typically the measurements were performed by successive compression/dilation cycles (force run measurements "in" performed during the day and force run measurement "out" perfomed during the night). As in the previous section, the force run measurements "out" are not presented here, they indeed exhibit a different behavior that we are not able to interpret.

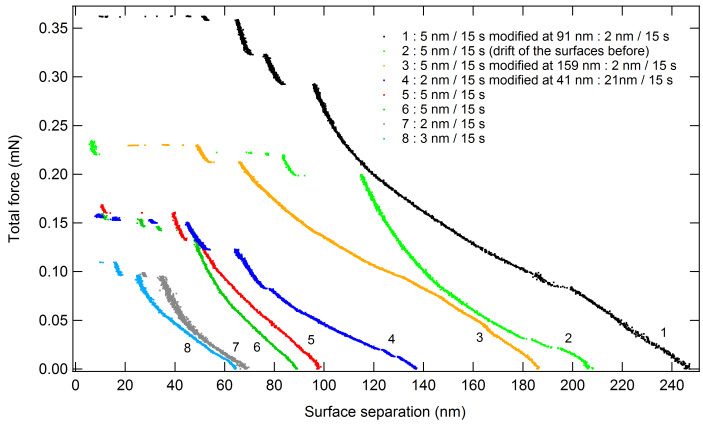

Figure 3.35: Total force as a function of the surface separation for several measurements performed upon the approach of the surfaces (sample N).

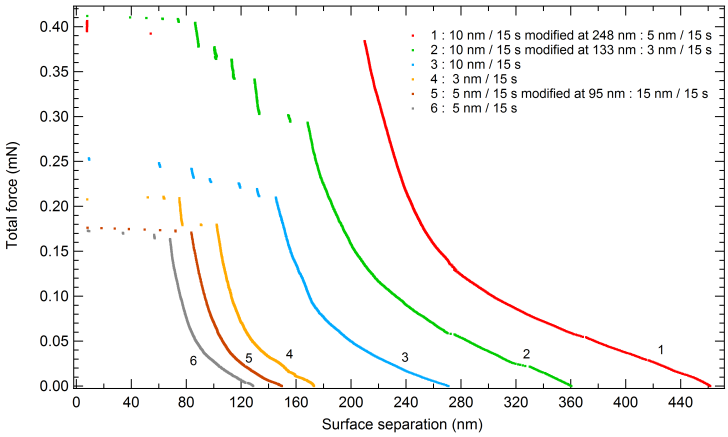

Figure 3.36: Total force as a function of the surface separation for several measurements performed upon the approach of the surfaces (sample O).

Several observations can be made :

- concerning sample N (O resp.), the measurements were performed between 60 nm and 250 nm (120 nm and 450 nm resp.) and the force maximum evolves between

0.10 mN and 0.36 mN (0.15 mN and 0.4 mN resp.), which is roughly larger by a factor 3 to the measurements presented in the previous section;

- at the beginning of the run, the force evolves linearly with the surface separation decrease;
- then the force deviates substantially from this linear background and increases;
- to release the stress, one or two inward jumps occur followed by very quick events bringing the surfaces to a contact position of approximately 7 nm.
- We note that the measurement marked 2 (sample N) is particularly steep; this may be explained by an unusual drift of the surfaces recorded during the night. Indeed the surfaces which were brought at a separation of $\sim$ 500 nm at 5 a.m. were found at $\sim$ 200 nm five hours later (average drift of +0.9 nm/minute).

In this study, no investigation was carried out regarding the influence of the speed on the surface movement: for the range of speed used and due to the behavior of the force which deviates from the linear background, it is difficult to draw clear observations.

3.1.2 Stiffness of the sample

The stiffness of the sample is calculated like in the previous section, for illustration, K_p as a function of the surface separation is plotted in Figure 3.37 for the measurement 1 (sample N).

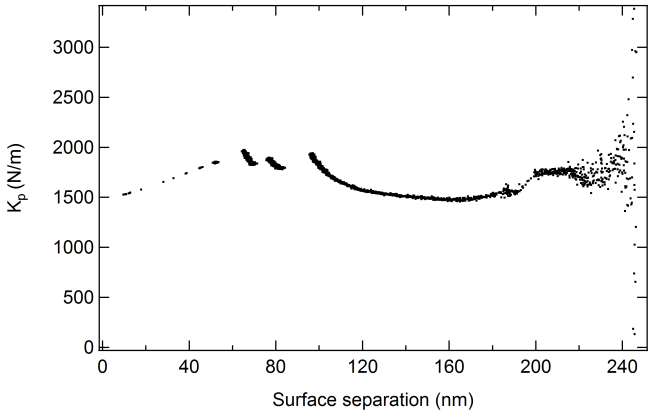

Figure 3.37: Stiffness K_p calculated for each point M_p as a function of the surface separation (sample N). At the beginning of the measurement, $K_s \simeq 1500$ N/m.

The average stiffness K_s deduced for sample N ranges between 1000 N/m and 2200 N/m (which is 20 to 44 times K_c). This is well above the stiffnesses of samples L (about 3 to 10 times K_c) and M (about 1 to 4 times K_c). This observation is consistent with the fact that the viscosity increases when the membrane volume fraction increases, thus

the sample appears to be stiffer. We obtain similar orders of magnitude for the stiffness of sample O, the experimental curves are presented in the end of the section (appendix).

The maximum deviation ϵ is of the order of 0.15 nm for measurement 1 ($C = 0.03$, $s_{piezo} = 5$ nm and $K_s = 30K_c$), which is small, and thus evidencing that the surface separation equilibrium is reached at any distance.

3.2 Elastic behavior and dislocation nucleation energies

To eliminate the contribution of the long-range interactions, a linear background has been subtracted to each total force profile. The resulting force profiles are presented in Figures 3.38a to 3.38h for sample N.

3.2.1 Observations and interpretation

These force profiles exhibit quite similar features. At the beginning of the measurement, the force evolves around zero and seems a little bit irregular; then the force increases progressively and becomes steeper and steeper; the stress is released by one or two inward jumps followed by very quick occurences (measurement 1: 3 minutes were required for the surfaces to "jump" from 50 nm to the contact position; note that the complete measurements lasted 9 hours); finally we note that the relaxation process may even lead to negative forces.

What is remarkable is that these force profiles do not superimpose on a master curve and clearly depends on the initial surface separation (this is why we have presented them in distinct figures). To get a better overview of the phenomenon, all the curves are gathered in Figure 3.39 for sample N. The force curves obtained for sample O are represented in Figure 3.40.

Such a behavior may be interpreted in terms of an energy barrier too high to nucleate the dislocations, so that the nucleation of an edge dislocation loop is delayed. To overcome the barrier, large strains exceeding a few bilayer thicknesses must be applied before the stress is released by the occurrence of a more likely nucleation. Thus, the compressive force follows a path located well above the supposed set of intersecting parabolae. The force-distance profile deviates rapidly from the pure elastic parabolic shape. Once the strain is large enough to promote the nucleation process, the stress is partly released: one or more bilayers are expelled. Then the force increases again steeply until the strain is large enough again to promote the nucleation process. Often, at this point, when the second (or the third) nucleation process starts, the system has enough energy to expel the stack of remaining bilayers "all at once". The stress is obviously well relaxed (see the unstable points that lead to the contact position).

One may note that most of the inward jumps positions coincide with jumps positions from other measurements but the distance separating two consecutive jumps positions is not equal to the period or to a multiple integer of it (it was the case in the previous section).

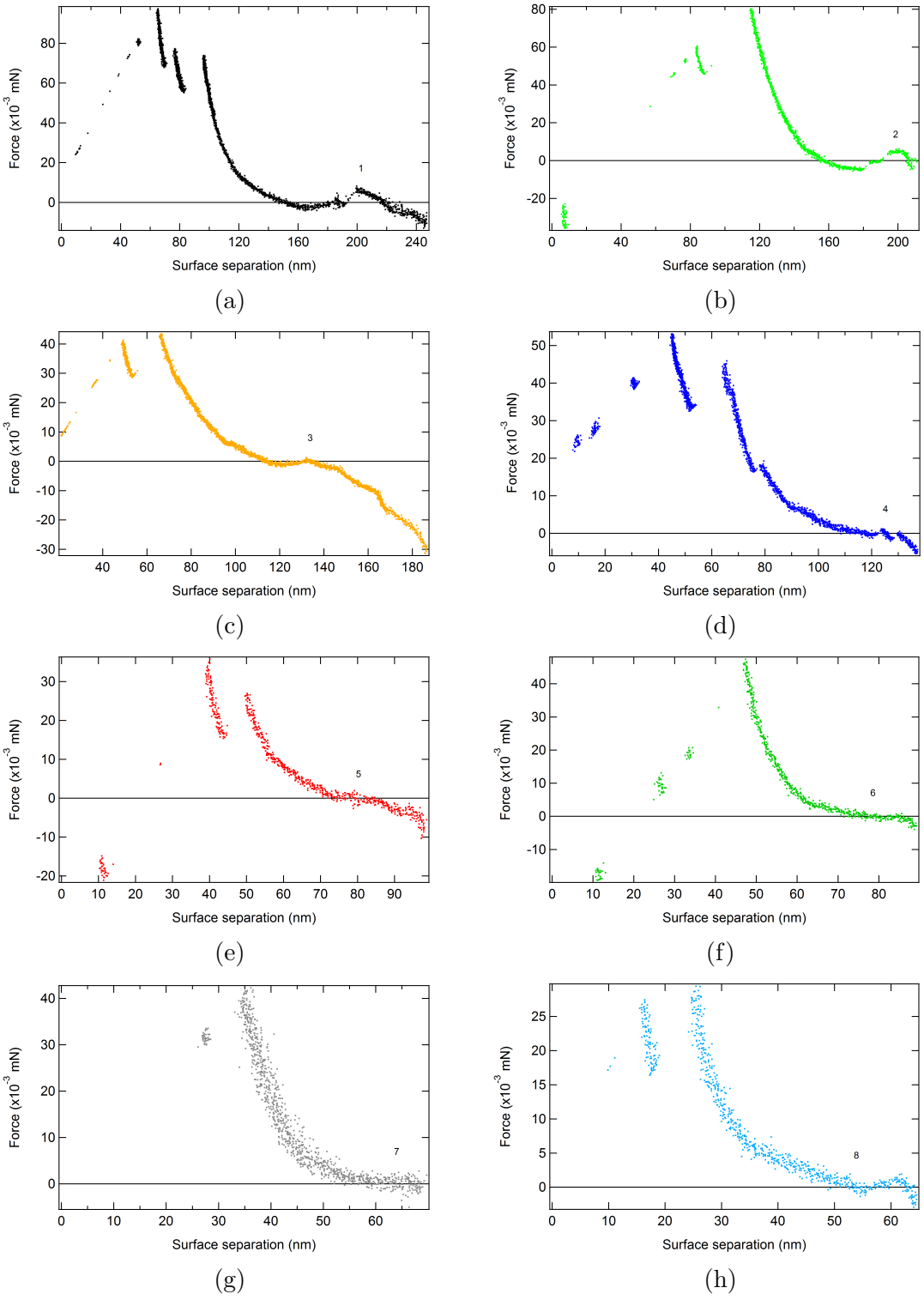

Figure 3.38: Resulting force as a function of the surface separation for measurements 1 to 8 (sample N) after subtraction of the linear background from the total force profile (see Figure 3.35).

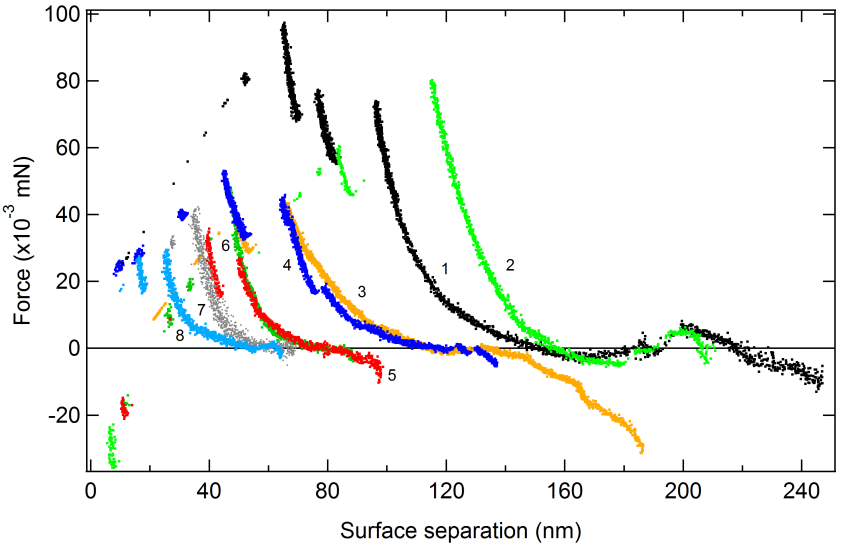

Figure 3.39: Forces as a function of the surface separation, the measurement 5 superimposes with 6 (sample N).

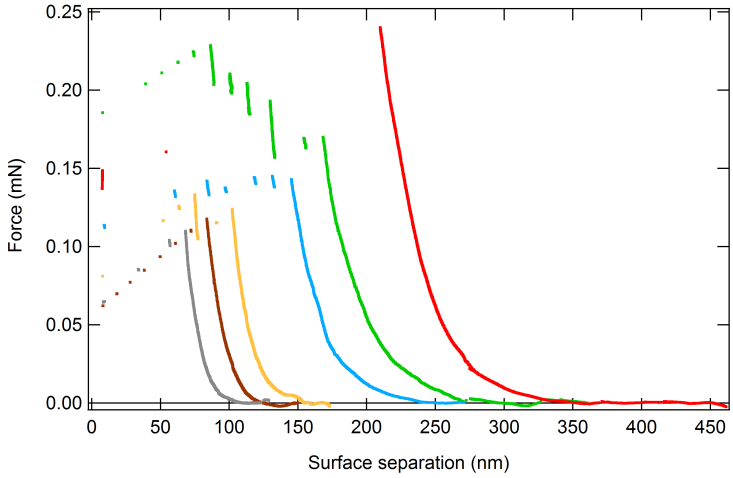

Figure 3.40: Forces as a function of the surface separation (sample O).

The interpretation that we suggest in the following is based first on the study of the parabolae (elastic regime), and then on the study of the "plastic regime" when the force deviates from the parabola.

3.2.2 Thermodynamic equilibrium

For each oscillation, the positions of the minima l_n are plotted against $n-2$ where n denotes the number of layers confined at the minimum of each parabola (Figure 3.41, sample N).

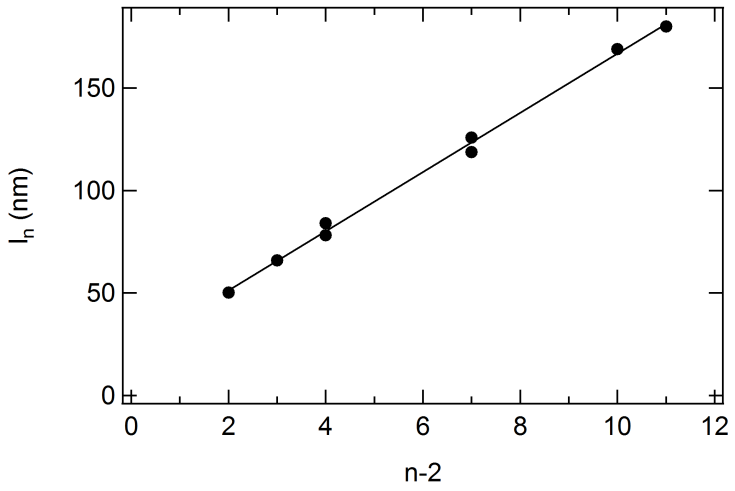

Figure 3.41: For each oscillation, the positions of the minima l_n are plotted against $n-2$. The solid line is the best fit to the data, giving a reticular distance 14.4 ± 0.3 nm in agreement with the X-ray measurement (sample N).

The solid line is the best fit to the data:

$$l_n = (22 \pm 2) + (14.4 \pm 0.3)(n-2)$$

and gives a reticular distance $d = 14.4$ nm in agreement with the periodicity inferred from the SAXS measurement. This additional criterion allows us to be confident in the fact that the thermodynamic equilibrium is reached at every step of the force run measurement.

The inward jumps are not treated since they are obtained in the plastic regime and are thus not expected to follow the usual law.

3.2.3 Elastic compressibility modulus

In Figure 3.42, the quantity $(F - F_n)\frac{l_n}{\pi R}$ is plotted against $\Delta {l_n}^2$ for the measurement 1 (sample N).

We identify the elastic regime in the linear part of the graph, and the deviation from the line is attributed to the plastic regime. In Figures 3.43a to 3.43g, the linear part is represented for all the measurements (sample N). Note that the measurement 2 is not presented here because the drift of the surfaces has certainly influenced the measurement since we obtain $\bar{B} = (27.4 \pm 2)$ kPa, which is much higher than the other values.

For each oscillation, the value obtained for $\bar{B}$ is plotted against n in Figure 3.44 for sample N and 3.45 for sample O.

The average value $\bar{B} = (18.8 \pm 2.5)$ kPa is considered as the bulk value of the elastic compressibility modulus of the lamellar mesophase located at the point N in the phase diagram. Similarly, we deduce $\bar{B} = (23.4 \pm 3.6)$ kPa the bulk value of the

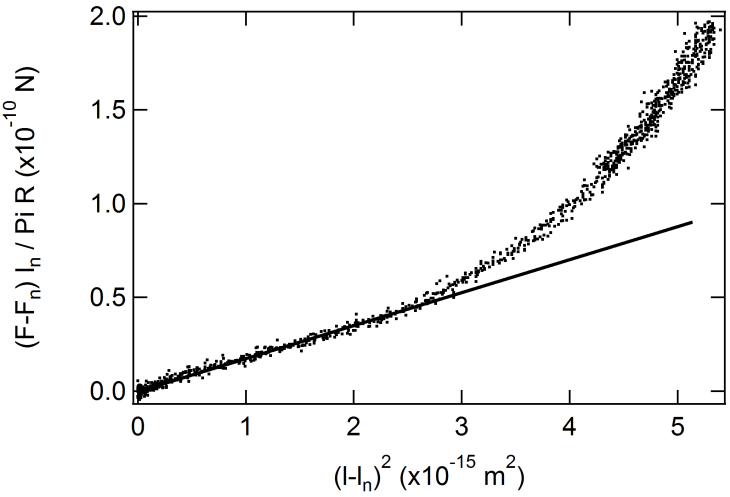

Figure 3.42: $(F - F_n)\frac{l_n}{\pi R}$ is plotted against ${\Delta l_n}^2$ for the measurement 1 (sample N).

elastic compressibility modulus for the lamellar mesophase located at the point O. The magnitudes of these moduli, which are close, will be discussed more in details in the Chapter 5.

Remark: The total elastic force between the surfaces is [83]:

$$F(l) = \pi R\bar{B}\frac{(l - n_0 d)^2}{n_0 d} + 2\pi R(\gamma + \gamma')\sum_{i=0}^{N_{max}} \frac{1}{\tilde{r}_i} \tag{3.8}$$

where l is the separation, n_0 is the number of layers in the "central cell" [83] (see Figure 4.6, Chapter 4, section 2), γ and γ' are respectively the far-field and the core energies, $\tilde{r}_i$ is the equilibrium radius of the dislocation loop. The first term is the wedge confinement energy (it arises exclusively from the central cell) and the second term is the contribution of the line energies, that we have obviously to take into account in this study. We see that this expression of the force deviates from the Derjaguin equivalence: an additional interaction proportional to the line energies $\gamma + \gamma'$ superimposes on the Derjaguin form. Because the Derjaguin approximation is strictly not valid in the whole range of forces measured, we have represented the force (and not the normalized force) as a function of the separation in Figures 3.39 and 3.38. But we could also have represented the normalized force, one should just keep in mind that the Derjaguin approximation is valid only in the elastic regime of compression, where it has been used to extract the elastic compressibility modulus.

3.2.4 Dislocation nucleation energies

In this part, we estimate the total energy necessary to break the n membranes that constitute the stack confined between the two mica surfaces at the minimum of the first parabola of the measurement. We calculate the area between the measured curve

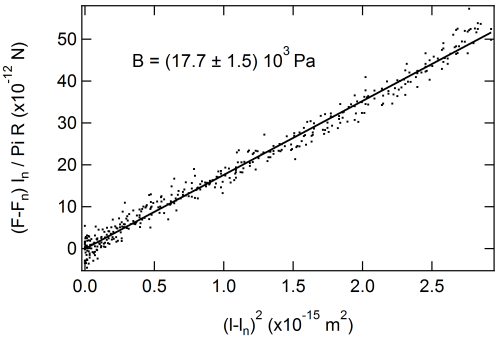

(a) measurement 1

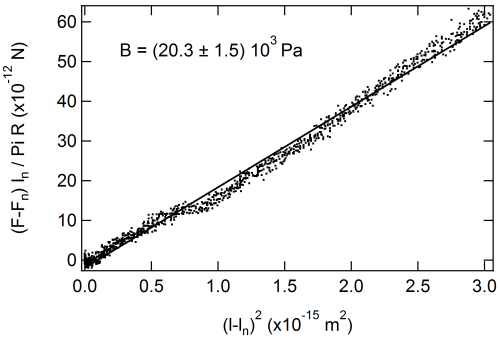

(b) measurement 3

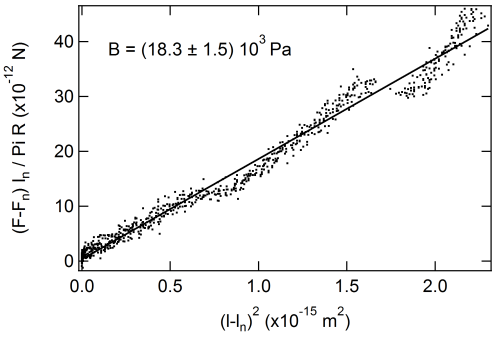

(c) measurement 4

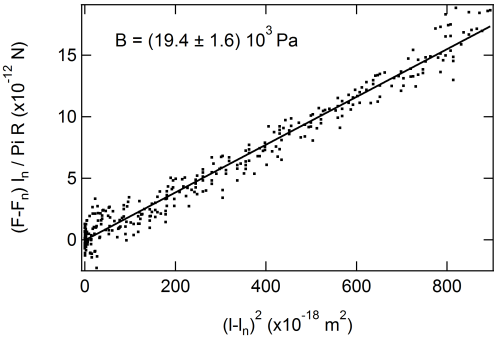

(d) measurement 5

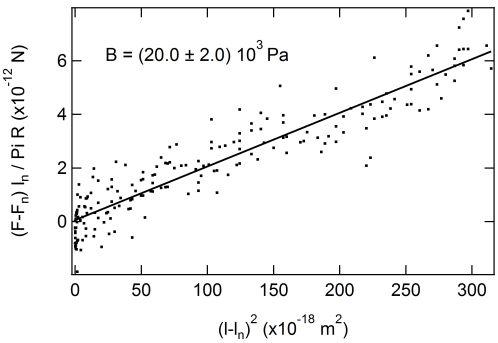

(e) measurement 6

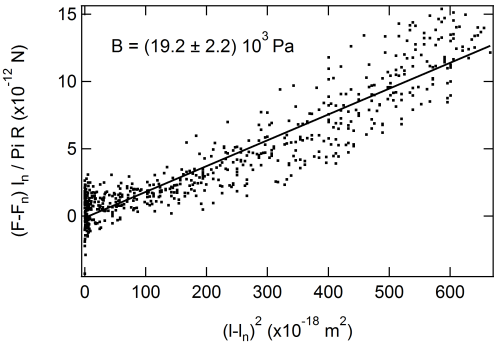

(f) measurement 7

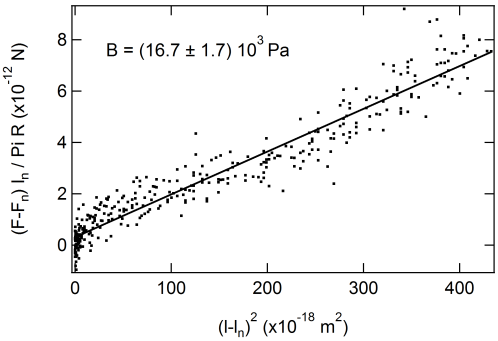

(g) measurement 8

Figure 3.43: The slopes of these graphs allow us to deduce the elastic compression modulus for measurements 1 and 3 to 8 (sample N).

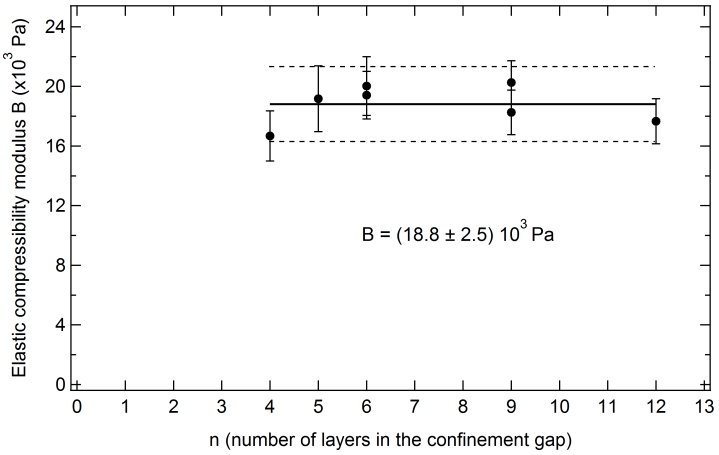

Figure 3.44: Plot of the elastic compressibility modulus obtained for each oscillation as a function of n (sample N).

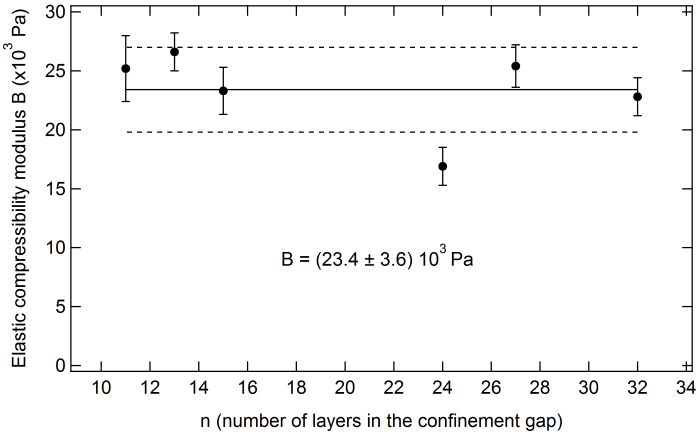

Figure 3.45: Plot of the elastic compressibility modulus obtained for each oscillation as a function of n (sample O).

and the parabolae, this area represents the work done by the system to achieve the expulsion of membranes from the confinement gap.

In Figures 3.46 and 3.47, the force profiles are presented as well as the *calculated* sets of parabolae with $l_n = 22 + 14.4(n-2)$ and $\bar{B} = 18.8$ kPa for sample N (Figure 3.46); $l_n = 19 + 10.9(n-2)$ and $\bar{B} = 23.4$ kPa for sample O (Figure 3.47).

In Figure 3.48 (sample N), we show how we measure the area for four measurements. This is based on the following assumptions:

- Once the system has jumped, we assume that the system is still in the plastic regime (which seems to be reasonable since all the portions of force are very steep).

- Concerning sample N, we do not favour a Burgers vector equal to 2. Indeed, if we

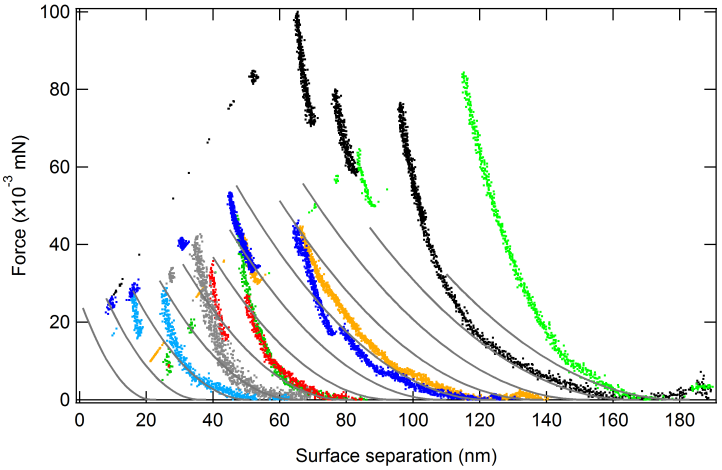

Figure 3.46: Force as a function of the surface separation (sample N). The solid lines are the calculated set of parabolae with $l_n = 22 + 14.4(n-2)$ and $\bar{B} = 18.8$ kPa.

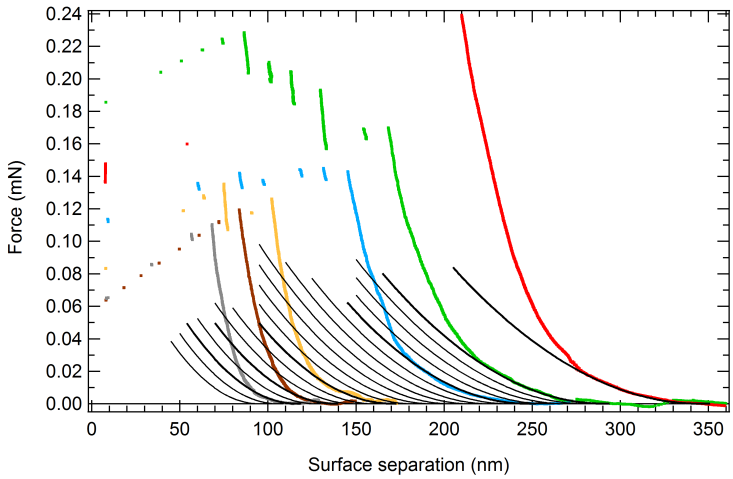

Figure 3.47: Plot of the force as a function of separation (sample O). The solid lines are the calculated set of parabolae with $l_n = 19 + 10.9(n-2)$ and $\bar{B} = 23.4$ kPa.

were assuming this for measurement 1, it would mean that the fourth jump belongs to the same parabola that measurement 5. This would give a very steep curve with almost no elastic regime and would absolutely not fit with the appearance of all measurements. Concerning sample O, we favour a Burgers vector equal to 2.

In Figure 3.49 (sample O), we show that the total energy is the sum of several areas.

In Figures 3.50 (sample N) and 3.51 (sample O), the total plastic energy measured for a stack of n membranes is plotted as a function of n in log-log representation. The solid line is a fit to the data and indicates a slope p equal to 2: $p = 2.1 \pm 0.4$ (sample N) and $p = 1.7 \pm 0.2$ (sample O).

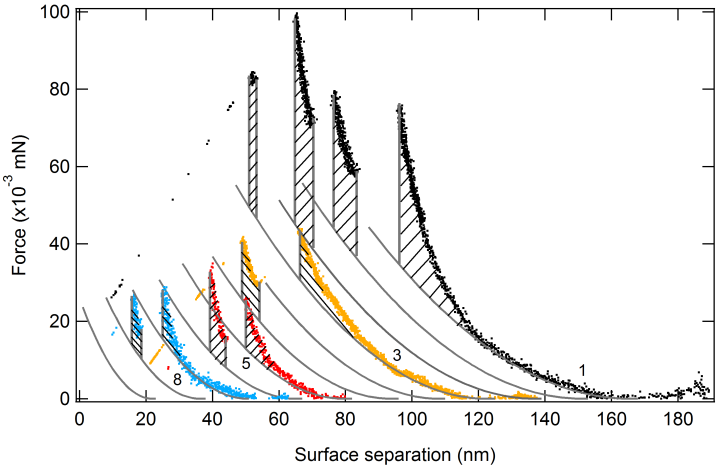

Figure 3.48: For each measurement, the hatched areas are summed up to calculate the total plastic energy (here shown for a few measurements, sample N).

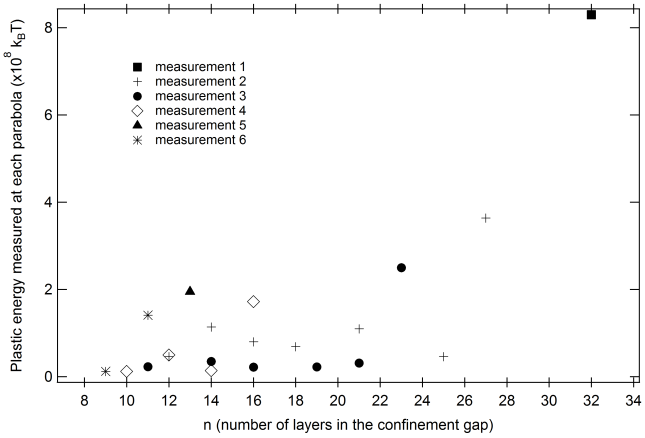

Figure 3.49: For each measurement (sample O), the total energy is the sum of several areas (in particular for measurement 2 and 3 which exhibit several jumps). Here is represented the area measured at each jump, between the measured force curve and the extrapolated parabola, as a function of n.

The total plastic energy necessary to break the stack of membranes at the minimum of the parabola appears to be proportional to n^2. Thus the law inferred from our measurements is: $\Delta E = \alpha n^2$ where ΔE denotes the total plastic energy.

In Figures 3.52 (sample N) and 3.53 (sample O), the total energy is divided by n^2 to extract the quantity $\alpha = (9.6 \pm 2.6)\, 10^5\ k_BT$ for sample N and $\alpha = (1.0 \pm 0.2) 10^6 k_BT$ for sample O. Surprisingly, we obtain very close values for this constant!

The interpretation of this law is not straightforward. Indeed we can expect a very complex mechanism leading to the expelling of the stack of membranes. For example, one could imagine a process where dislocation loops of Burgers vectors equal to 1 or 2 (discrete jumps) arise at the start, followed by a screw dislocation of Burgers vector

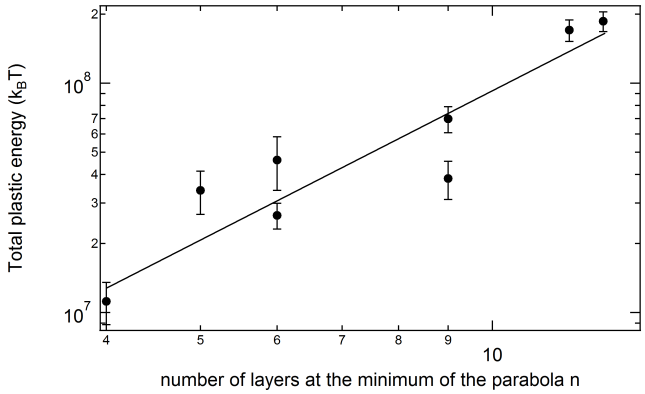

Figure 3.50: Total plastic energy as a function of n, the number of membranes that constitute the stack confined between the two mica surfaces at the minimum of the first parabola of the measurement, in a log-log representation (sample N). The solid line is a fit to the data and indicates a slope $p = 2.1 \pm 0.4$.

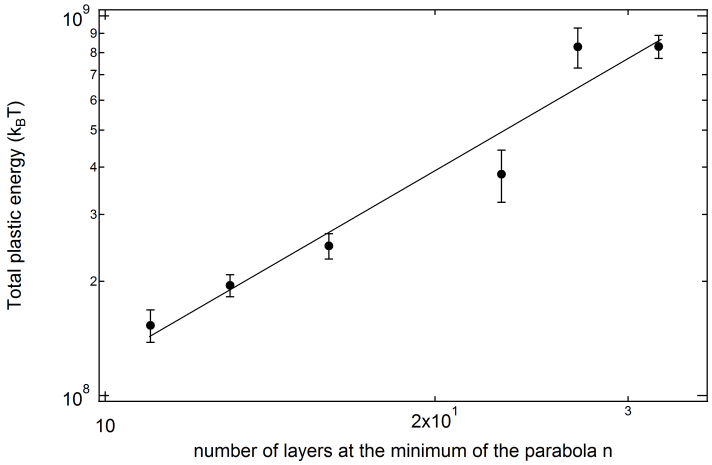

Figure 3.51: Plot of the total plastic energy as a function of n in a log-log representation (sample O). The solid line is a fit to the data and indicates a slope $p = 1.7 \pm 0.2$.

equal to the remaining number of layers (very quick events, where one bilayer may drag along an other bilayer and so on). The screw dislocation could be partly activated during the plastic regime. We discuss these aspects related to dislocations in the Discussion (Chapter 5).

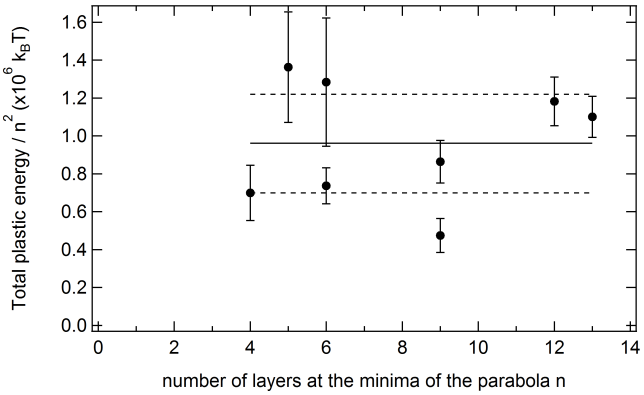

Figure 3.52: Total plastic energy ΔE divided by n^2, plotted against n, the number of membranes that constitute the stack confined between the two mica surfaces at the minimum of the first parabola of the measurement. This allows to extract $\alpha = (9.6 \pm 2.6)\, 10^5\ k_B T$.

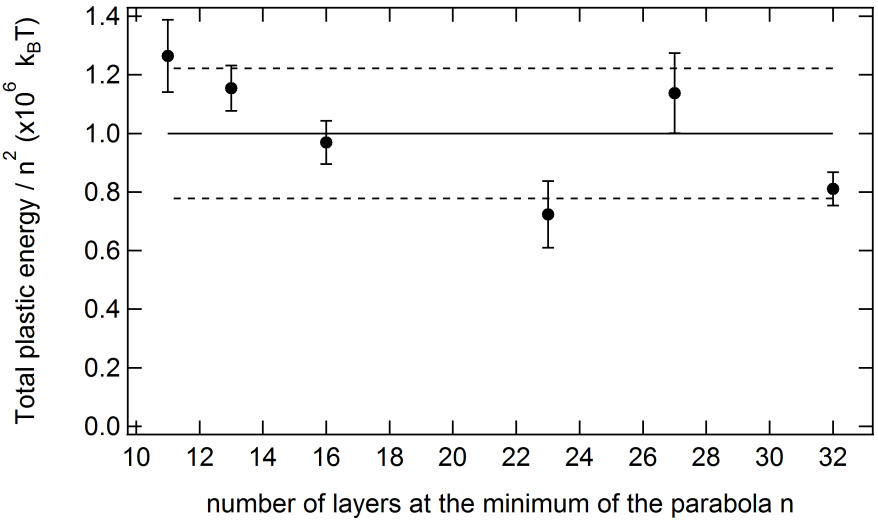

Figure 3.53: Total plastic energy ΔE divided by n^2, plotted against n, the number of membranes that constitute the stack confined between the two mica surfaces at the minimum of the first parabola of the measurement. This allows to extract $\alpha = (1.0 \pm 0.2) 10^6 k_B T$

3.3 Appendix: experimental curves for sample O

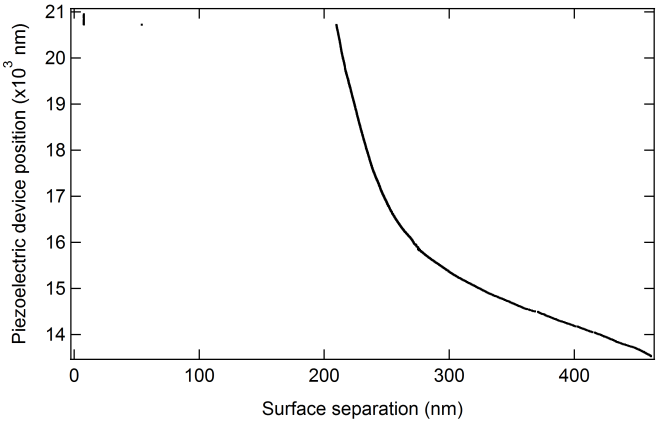

Figure 3.54: Piezoelectric device position as a function of the surface separation (measurement upon approach of the surfaces). The measurement has been performed at a speed of 10 nm/15 s (modified at 250 nm: 5 nm/15 s). The average slope of this graph between 330 nm and 440 nm is $C = 0.01$, which is of the same order of magnitude than for sample N.

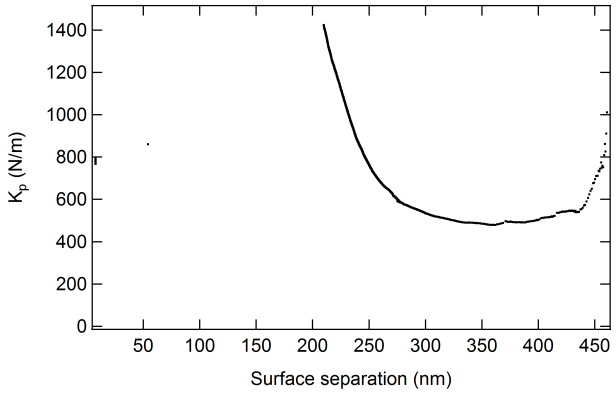

Figure 3.55: Stiffness K_p calculated for each point M_p as a function of the surface separation (measurement 1). At the begining of the measurement, $K_s \simeq 500$ N/m and then it increases a lot onwards to 1400 N/m. At this point, the stress is finally released by the nucleation of a dislocation. Note that the maximum deviation ϵ is of the order of 0.9 nm at the beginning of the measurement, where $K_s \simeq 10K_c$, $C = 0.01$ and with $s_{piezo} = 10$ nm. The measurement is thus performed at the thermodynamic equilibrium.

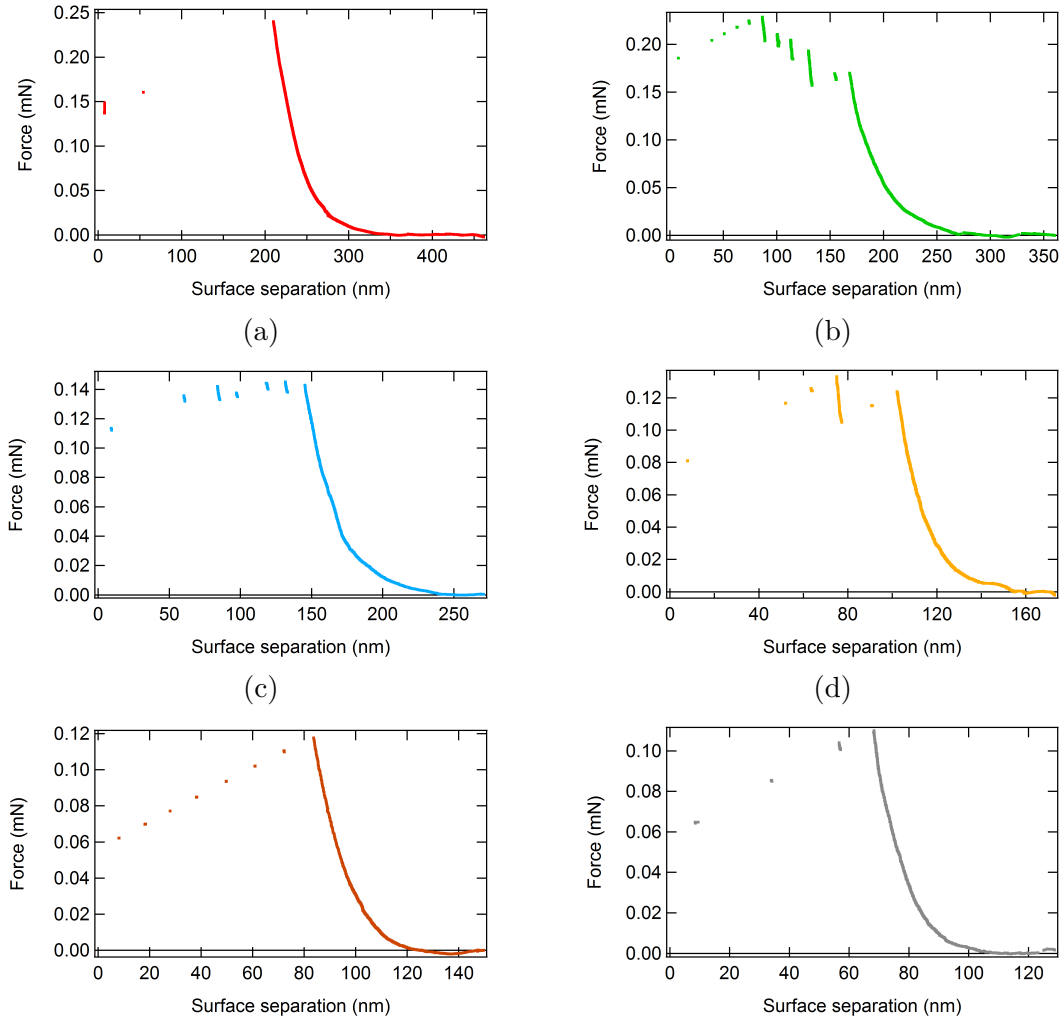

Figure 3.56: Force as function of the surface separation for measurements 1 to 6, after subtraction of the linear background. The stress is released by one or more inwards jumps followed by very quick occurences: 30 seconds were required for the surfaces to "jump" from 210 nm into the contact position for measurement 1. Note that the complete measurements lasted 5 hours. Concerning measurement 2, 2.5 minutes were required for the surfaces to jump from 75 nm into the contact position which is again short compared to the duration of the complete measurement (5 hours also).

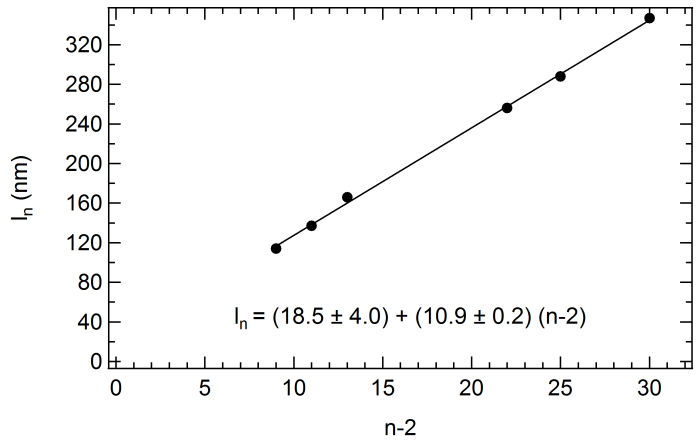

Figure 3.57: For each oscillation, the positions of the minima l_n are plotted against $n-2$. The solid line is the best fit to the data $l_n = (19 \pm 4) + (10.9 \pm 0.2)(n-2)$, giving a reticular distance 10.9 ± 0.2 nm in agreement with the X-ray measurement.

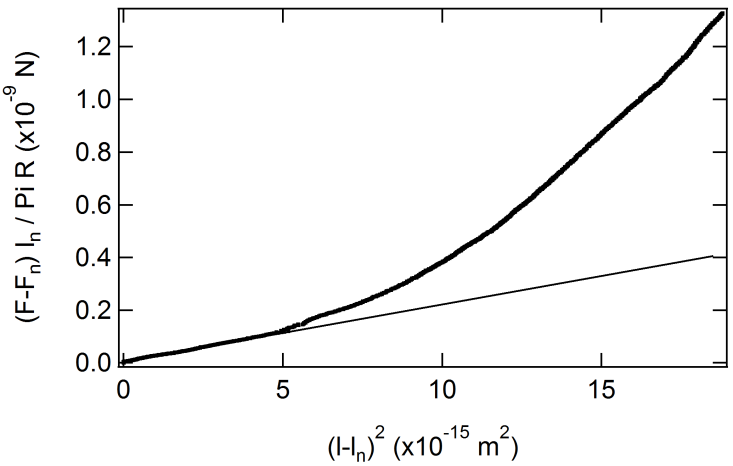

Figure 3.58: The two quantities $(F - F_n)\frac{l_n}{\pi R}$ and $\Delta {l_n}^2$ are plotted for the measurement 1 according to the equation $(F-F_n)\frac{l_n}{\pi R} = B\Delta {l_n}^2$ where F_n are the forces at the minima l_n. We identify the elastic regime in the linear part of the graph, and the deviation from the line is attributed to the plastic regime.

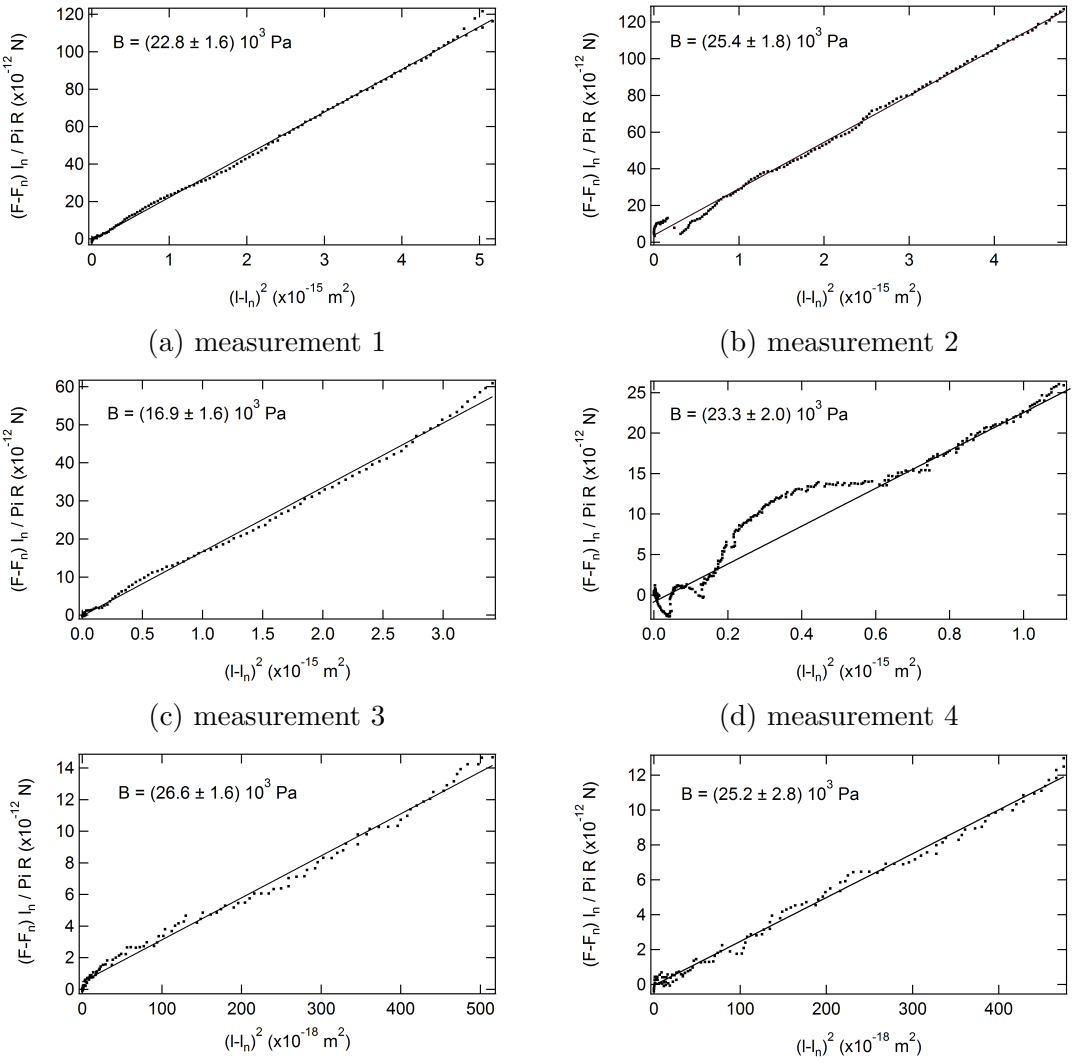

(a) measurement 1 (b) measurement 2

(c) measurement 3 (d) measurement 4

(e) measurement 5 (f) measurement 6

Figure 3.59: The linear part is represented here for each measurement and thus allows us to infer a value for the elastic compression modulus.

3.4 Measurements at large separations: large Burgers vectors

In this section, we present measurements performed on *sample N* at large separations, between 5 and 10 μm. To our knowledge, this is the first time that such measurements are performed. Indeed the stability of the SFA developped in Strasbourg and the possibility of acquiring data at very large separations has allowed us to investigate such separation ranges that was not possible before, and not accessible in the other laboratories using the SFA technique.

3.4.1 Total force

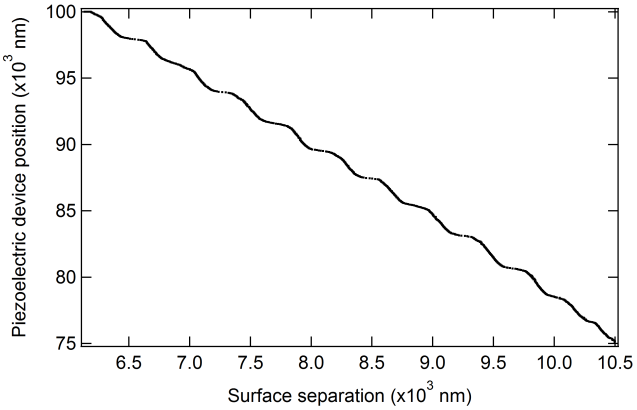

Figure 3.60: Piezoelectric device position as a function of the surface separation (measurement upon approach of the surfaces).

In Figure 3.60, a measurement performed at a speed of 25 nm/15 s is presented. The average slope of this graph gives $C = 0.18$, which is similar to the value obtained in section 2 concerning sample L (without polymer). The total force versus separation profile is presented in Figure 3.61.

The total force versus separation profile exhibits the same features as those presented in section 2: oscillations superimpose on a linear background. The stiffness of the sample is presented in the Figure 3.62, and appears to be of the same order of magnitude than the values inferred for sample L.

Some other measurements performed at smaller speeds (5 nm/15 s, 10 nm/15 s, 15 nm/15 s) exhibit the same features, but the stiffness of the sample seems to decrease a little bit when the speed is decreased (as particularly observed for sample M, section 2).

3.4.2 Elastic behavior

To eliminate the contribution of the long-range interactions, the linear background has been subtracted from the total force profile. The resulting force profile is presented in Figures 3.64 and 3.64.

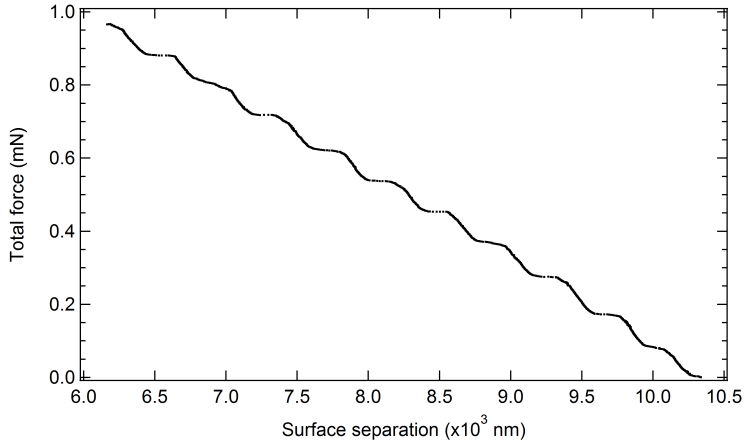

Figure 3.61: Total force as a function of the surface separation (measurement upon approach of the surfaces).

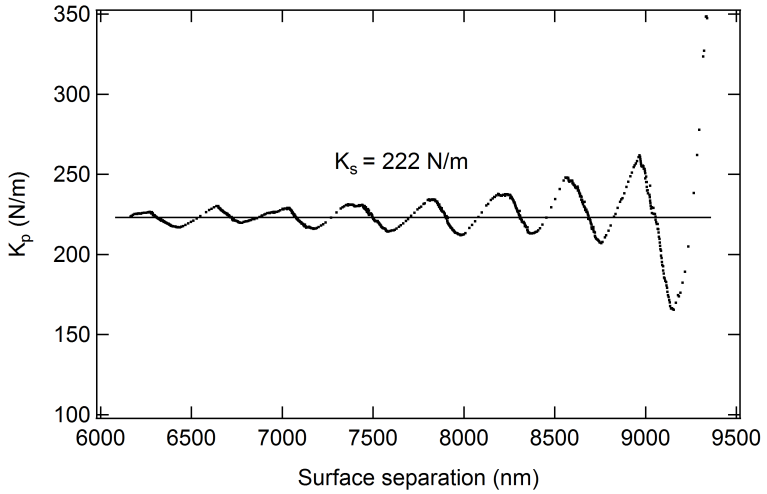

Figure 3.62: Stiffness K_p calculated for each point M_p as a function of the surface separation.

This force profile exhibits large and regular oscillations, of constant amplitude of about 2 mN/m, whose minima are separated by a distance corresponding to about 30 periodicities of the sample. The force oscillates around zero. These values are far above the amplitudes and Burgers vectors observed for samples L and M which exhibit also regular oscillatory force profiles (see section 2). Indeed, for sample L, the amplitude of the oscillations ranges from 0.1 mN/m far from the contact position, to about 0.7 mN/m for the oscillation preceding the steric wall position. The Burgers vector is equal to two for both samples L and M.

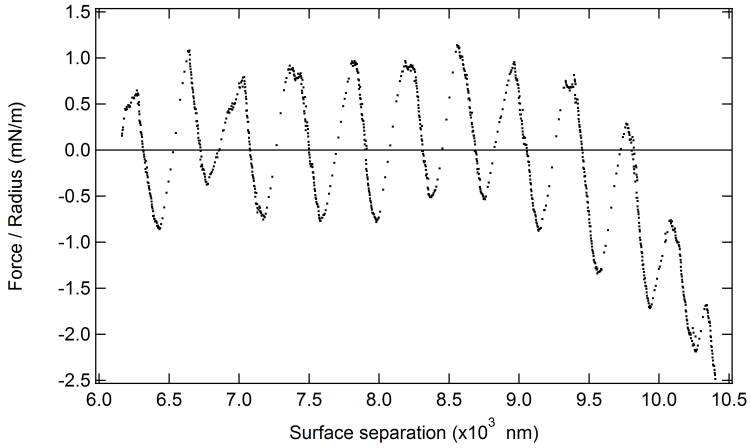

Figure 3.63: Normalised force as a function of the surface separation, the unstable points are left on purpose.

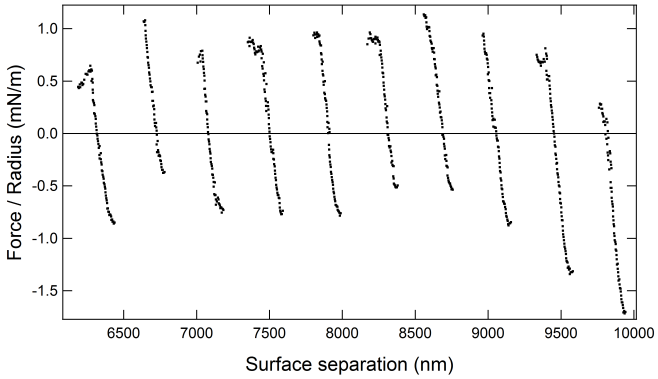

Figure 3.64: The same force profile, zoomed on the first ten oscillations and without unstable points.

3.4.3 Thermodynamic equilibrium

Here, as n is very large (n is equal to 460 at least), $n - 2 \sim n$. We plot for each oscillation the position of the minimum l_n against n (Figure 3.65) and the position of the inwards jump l_n^i against $\sqrt{n(n-b)}$ where $b \simeq 26$ in average (Figure 3.66).

The solid lines are the best fits to the data:

$$l_n = (4 \pm 6) + (14.59 \pm 0.01)n$$

$$l_n^i = (102 \pm 37) + (14.46 \pm 0.06)\sqrt{n(n-26)}.$$

The slopes give a reticular distance $d = 14.6$ nm and $d = 14.5$ nm respectively in agreement with the periodicity inferred from the SAXS measurement. The fact that the measured values are so close to the fitted line indicates that the forces were measured at thermodynamic equilibrium. Note that $\epsilon = 3.7$ nm for this measurement ($s_{piezo} = 25$

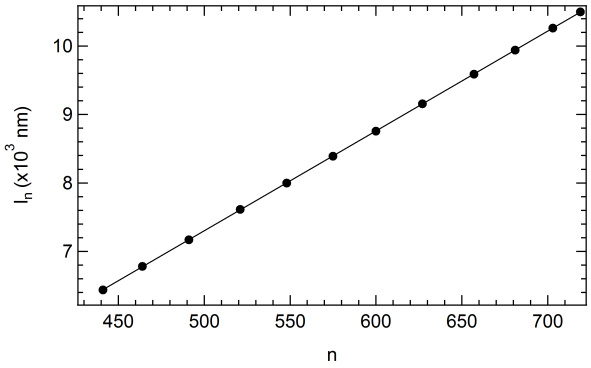

Figure 3.65: For each oscillation, the positions of the minima l_n are plotted against n. The solid line is the best fit to the data, giving a reticular distance 14.59 ± 0.01 nm in agreement with the X-ray measurement.

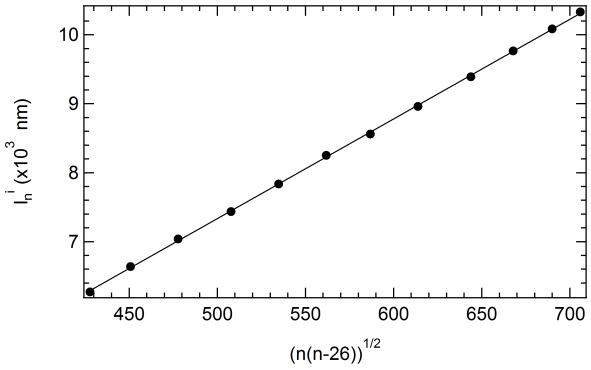

Figure 3.66: For each oscillation, the positions of the inwards jumps l_n^i are plotted against $\sqrt{n(n-26)}$. The solid line is the best fit to the data, giving a reticular distance 14.46 ± 0.06 nm in agreement with the X-ray measurement.

nm, $K_s \simeq 4.5 K_c$ and $C = 0.18$), which of course is higher than the values inferred in previous Chapters, but considering the large amplitude of the Burgers vectors, ϵ this very small.

3.4.4 Elastic compressibility modulus

In Figure 3.68, the quantity $(F - F_n)\frac{l_n}{\pi R}$ is plotted against $\Delta {l_n}^2$ for each oscillations, allowing us to deduce $\bar{B}$ from the slope.

For each oscillation the value obtained for $\bar{B}$ is plotted against n in figure 3.67. The average value $\bar{B} = (1.8 \pm 0.4)\, 10^5$ Pa is considered as the bulk value of the elastic compressibility modulus of that lamellar mesophase, for these range of separations. It is one order of magnitude larger than the value extracted in the previous analysis, for the same sample, at shorter separations (see section 3). Its magnitude will be discussed in the Chapter 5.

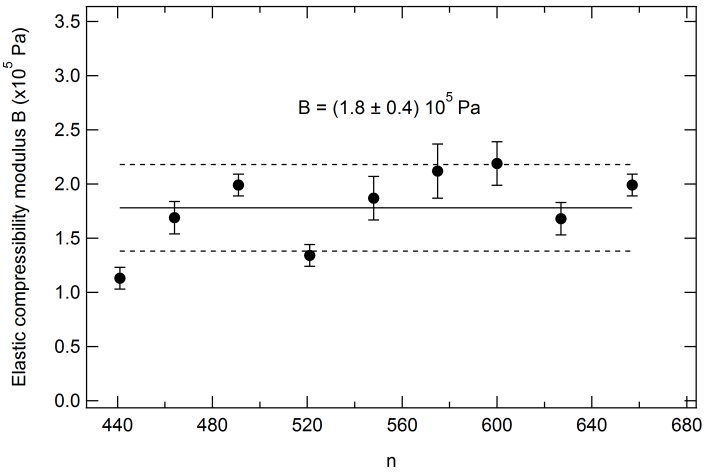

Figure 3.67: Plot of the elastic compressibility modulus obtained for each oscillation as a function of n.

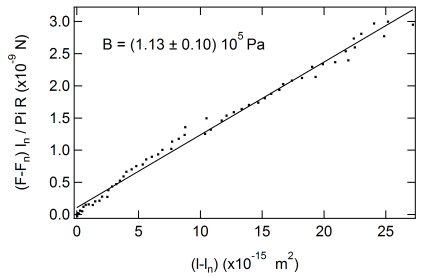

(a) first oscillation ($l_n \sim 6.5\ \mu m$)

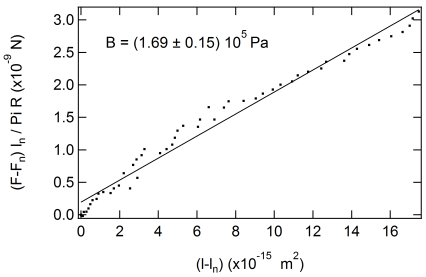

(b) second oscillation

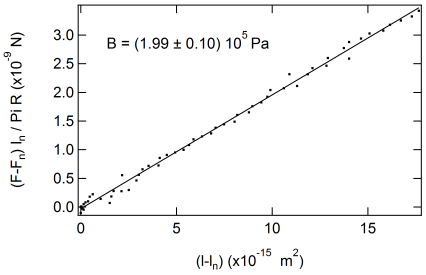

(c) third oscillation

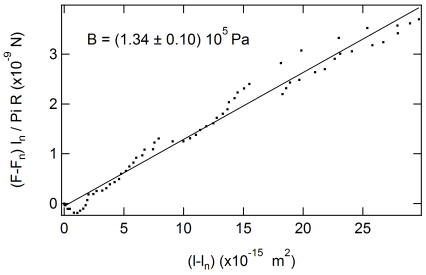

(d) fourth oscillation

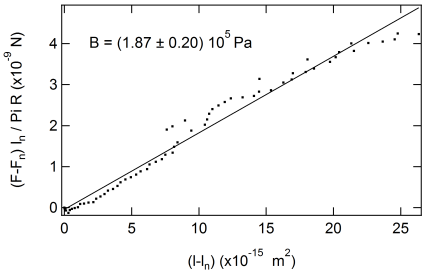

(e) fifth oscillation

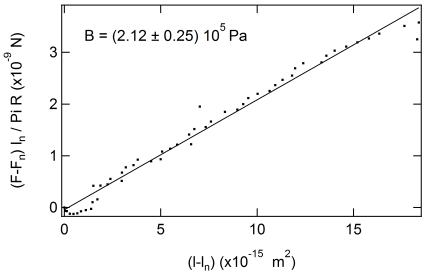

(f) sixth oscillation

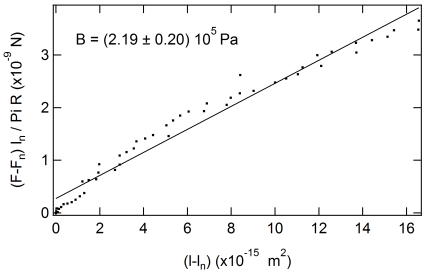

(g) seventh oscillation

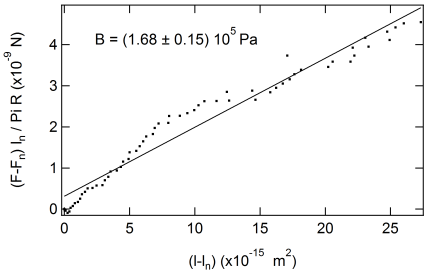

(h) eighth oscillation

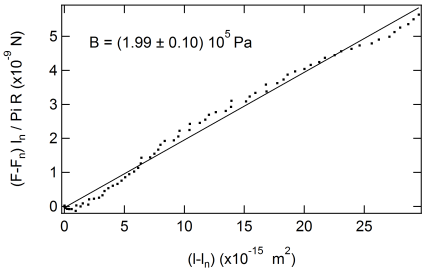

(i) ninth oscillation

Figure 3.68: $(F - F_n)\frac{l_n}{\pi R}$ plotted against $\Delta {l_n}^2$ for each parabola, allowing us to deduce $\bar{B}$ from the slope.

Chapter 4

Theoretical aspects

1 Theoretical aspects about the elastic compressibility modulus

In this part, the aim is to interpret the values of the elastic compressibility moduli measured. In a first part, we recall the existing models concerning the elastic compression modulus. In a second part, relying on the same models and calling upon other theories, we try to interpret the experimental results.

1.1 Existing models

1.1.1 Binary systems

In this section, we consider binary systems. Most of the time, there is also a cosurfactant in the lamellae so that the system is pseudo-binary.

Undulations

The undulation interaction comes from the significance of the thermally induced fluctuations of the membranes. A membrane undulating between its two neighbours is confined in a space that is restricted compared to the space it would occupy alone. Thus, the membrane cannot explore all the allowed configurations which is not advantageous and leads to a repulsion between the membranes. The origin is thus steric and entropic. In [47], Helfrich calculates the interaction potential per unit area:

$$V_{und}(d) = \frac{3\pi^2}{128}\frac{(k_BT)^2}{\kappa\bar{d}^2}$$

where κ is the normal bending elastic modulus and $\bar{d}$ the interlayer spacing. For a flexible membrane, κ is of the order of k_BT whereas κ is large compared to k_BT for rigid membranes. So the more flexible the membranes, the larger is the undulation interaction.

The elastic compressibility modulus is defined by $\bar{B} = d\frac{\partial^2 V}{\partial d^2}$ and thus given by

$$\bar{B}_{und} = \frac{9\pi^2 (k_B T)^2 d}{64\kappa \bar{d}^4} \tag{4.1}$$

The undulation interaction is long-range and may stabilize the lamellar phase when the periodicity is very large. In particular, when the membranes are not charged or if the electrostatic interaction is screened (intermembrane spacing filled with a salted solution), the undulation interaction stabilizes the lamellar phase.

Electrostatics

The lamellar phase is considered as a stack of parallel charged rigid planes (non-undulating) immersed in an electrolyte solution. To get the electrostatic interaction between two neighbouring planes, one can solve the unidimensional Poisson-Boltzmann equation (see [20]):

$$\frac{\mathrm{d}^2\Psi}{\mathrm{d}x^2} = -\frac{\rho(x)}{\epsilon_r \epsilon_0} = -\frac{\rho_0}{\epsilon_r \epsilon_0} \mathrm{e}^{-e\Psi/k_B T}$$

where Ψ is the electrostatic potential, ρ is the charge density (ρ_0 is the charge density at the midplane), e the elementary charge, ϵ_0 is the permittivity of free space and ϵ_r is the relative permittivity of the medium between the planes. We work with the International System of Units (SI). Depending on the boundary conditions, the interaction energy per unit surface can be calculated.

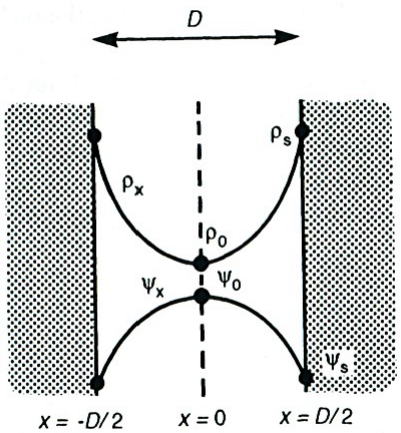

Figure 4.1: Two negatively charged surfaces of surface charge density σ, a distance D apart in water. The only ions in the space between them are counterions that have dissociated from the surfaces. The counterion density profile $\rho(x)$ and electrostatic potential $\Psi(x)$ are shown schematically. The values at the surfaces, called the "contact values" are denoted by the "s" index.

Simple analytical expressions for the electrostatic intermembrane potential V_{elec} are known in two asymptotic limits:

- the system consists of two uniformly charged planes separated by the counterions in water (no added salt) [86]:

$$V_{elec}^{\text{no salt}} = \frac{\pi k_B T}{4 L_B \bar{d}} \Big(1 - \frac{\Sigma}{\alpha \pi L_B \bar{d}} + \Big(\frac{\Sigma}{\alpha \pi L_B \bar{d}} \Big)^2 + ... \Big)$$

where $L_B = \frac{e^2}{4\pi\epsilon_r \epsilon_0 k_B T}$ is the Bjerrum length of the solvent at room temperature ($L_B \simeq 7$ Å for water), $\bar{d}$ is the thickness of the water layers between membranes, Σ is the surface area per charged polar head and α is the dissociation coefficient.

Finally $\bar{B}$ is given by:

$$\bar{B}_{elec}^{\text{no salt}} = \frac{\pi k_B T d}{2 L_B \bar{d}^3} \Big(1 - 3 \frac{\Sigma}{\alpha \pi L_B \bar{d}} + 6 \Big(\frac{\Sigma}{\alpha \pi L_B \bar{d}} \Big)^2 + ... \Big) \tag{4.2}$$

- for sufficiently large additions of salt, the Debye screening length λ_D is smaller than the interlayer spacing $\bar{d}$, and one obtains [53]:

$$V_{elec}^{\text{salt}} = \frac{4 k_B T}{\pi \lambda_D L_B} \gamma^2 e^{-\frac{\bar{d}}{\lambda_D}}$$

where $\gamma = \tanh\big(\frac{1}{2}\text{argsinh}(2\pi \frac{L_B \lambda_D}{\Sigma})\big)$, $\lambda_D = \frac{3.04}{\sqrt{c_s}}$ and c_s is the salt concentration expressed in mol/L and λ_D is expressed in Å.

Finally $\bar{B}$ is given by:

$$B_{elec}^{\text{salt}} = \frac{4 k_B T}{\pi \lambda_D L_B} \gamma^2 e^{-\frac{\bar{d}}{\lambda_D}} \tag{4.3}$$

However, in various experimental cases, the situation is in-between these two limits, as shown by Dubois et al. in [30]. They performed osmotic pressure measurements on lyotropic smectic mesophases (DDAB/water system, DDAB is the didodecyldimethylammonium bromide, a cationic surfactant). Their experimental results are not well described by these two asymptotic limits. In this work, Dubois et al. give a general calculation (Poisson-Boltzmann framework) of the electrostatic pressure between two charged membranes, whatever are the experimental conditions (added salt or not). They perform a numerical calculation in the grand canonical ensemble (the lamellar phase is in thermodynamical equilibrium with a reservoir of salinity c_s') and get:

$$\Pi_{elec} = 4 k_B T c_s' \sinh^2 \Big(\frac{\Psi(0)}{2} \Big) \tag{4.4}$$

where $\Psi(0)$ is the electrostatic potential at the midplane.

Porcar et al. [80] continued to work in the same framework:

- they solved numerically the Poisson-Boltzmann equation $\longrightarrow \Psi$

- they derived the elastic compressibility modulus from the expression of the pressure given in equation (4.4) $\longrightarrow \bar{B}(\Psi)$

They finally calculated the electrostatic layer compression modulus $\bar{B}$ as a function of the physical parameters of the lamellar phase Σ, d and c_s [80, 79].

For the case without salt, they present an interesting curve presented in Figure 4.2 which shows the variation of the layer compressional modulus in reduced units $\bar{b}$ versus the reduced surface area per charge of the membrane τ:

$$\bar{b} = \frac{2L_B\bar{d}^3}{\pi k_B T d}\bar{B}_{elec}$$

$$\tau = \frac{\Sigma}{\bar{d}L_B}$$

Thanks to this curve, one can estimate a correction to the elastic compressibility modulus usually calculated with the formula: $\bar{B} = \frac{\pi k_B T d}{2L_B\bar{d}^3}$. When the interlayer spacing $\bar{d}$ is large enough, the parameter τ approaches zero and the asymptotic limit described above (first term of equation (4.2)) becomes completely relevant: the membrane is seen as a continuous object.

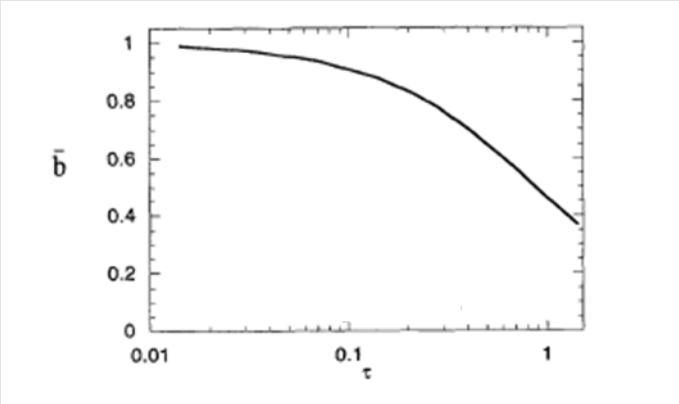

Figure 4.2: Figure extracted from [80]. Elastic compressibility modulus in reduced units $\bar{b} = \frac{2L_B\bar{d}^3}{\pi k_B T d}\bar{B}_{elec}$ as a function of the parameter $\tau = \frac{\Sigma}{\bar{d}L_B}$.

1.1.2 Ternary systems

In this section we consider ternary systems surfactant/water/polymer, where the polymer is located in the water layers and do not interact with the membranes.

Ligoure et al. approach

Most of works done about ternary systems [11, 71] assume additivity of the interactions that is the intermembrane potential is the sum of the contributions of the smectic and the polymer solution:

$$V_{total} = V_{smectic} + V_{polymer}$$

where $V_{smectic} = V_{elec}$ (resp. $V_{smectic} = V_{und}$) if the smectic is stabilized by electrostatic interactions (resp. undulations). This equation leads to the following one:

$$\bar{B}_{total} = \bar{B}_{smectic} + \bar{B}_{polymer}$$

To our knowledge, the only quantitative work providing a theory of the contribution of the polymer to the elastic compressibility modulus in various regimes of polymer confinement is the work of Ligoure et al. [71]. Daoud and de Gennes studied theoretically these regimes of polymer confinement [22] followed by Brooks and Cates [11].

In [71], the authors first present a general calculation of the elastic compressibility modulus at constant chemical potential. They start with the elastic compressibility modulus at constant surface fraction of guest components $\bar{B}_\sigma$

$$\bar{B}_\sigma = d\frac{\partial^2 V}{\partial \bar{d}^2}$$

with the geometric relation

$$\sigma = \bar{\Phi}\frac{\bar{d}}{2a}$$

where $\bar{\Phi}$ is the polymer volume fraction in the solvent, σ the surface fraction of polymer per unit area of bilayer ("projection" of $\bar{\Phi}$ on the membranes) and a the monomer length.

The authors then perform a canonical Legendre transform of V and get the elastic compressibility modulus at constant chemical potential μ (which is more relevant since σ is not a locally conserved quantity):

$$\bar{B}_\mu = \bar{B}_\sigma - d\Big(\frac{\partial^2 V}{\partial \bar{d}\partial\sigma}\Big)^2\Big(\frac{\partial^2 V}{\partial \sigma^2}\Big|_{\bar{d}}\Big)^{-1}$$

They present then the four different regimes of confinement for a non-adsorbing polymer found and studied by Daoud and de Gennes and revisited more recently by Brooks and Cates. Based on these previous studies, Ligoure et al. give the polymer free energy corresponding to each regime and derive the elastic compressibility modulus:

i. $\bar{d} >> R_F$ and $\bar{\Phi} << \Phi^*$

The chains do not overlap and retain their spherical coil conformation. The solvent is a three-dimensional dilute solution of polymer chains (3D-D regime). The polymer free energy density is the perfect gas term corrected for the depletion effect:

$$V_{pol} \simeq \frac{k_B T}{a^3}\bar{d}\frac{\bar{\Phi}}{N}\log(\bar{\Phi}_{eff})$$

where $\bar{\Phi}_{eff}$ is the effective volume fraction of polymers in the middle of the interlayer gap, a the monomer length, N the polymerization index. The elastic compressibility modulus is deduced:

$$\bar{B}_\mu^{pol} \simeq -4\frac{k_B T N^{1/5} d\bar{\Phi}}{a\bar{d}^3} \tag{4.5}$$

ii. $\bar{d} >> a\bar{\Phi}^{-\frac{3}{4}}$ and $\bar{\Phi} >> \Phi^*$

The chains overlap, but still remain unsqueezed. The solvent is a three-dimensional semi-dilute solution of polymer chains (3D-SD regime). The polymer free energy density is the sum of the "bulk" contribution (first term) and the depletion effect contribution (second term):

$$V_{pol} = \beta \frac{k_B T}{a^3} \bar{d} \bar{\Phi}^{9/4} + 2 \frac{k_B T}{a^2} \rho \bar{\Phi}^{3/2}$$

where β and ρ are universal prefactors calculated in [11]. The elastic compressibility modulus is deduced:

$$\bar{B}_{\mu}^{pol} \simeq -\frac{16 \rho^2 k_B T}{5 \beta a} \frac{d}{\bar{d}^3} \bar{\Phi}^{3/4} \tag{4.6}$$

iii. $\frac{a}{N\bar{\Phi}^2} << \bar{d} << a\bar{\Phi}^{-\frac{3}{4}}$ and $\bar{\Phi} >> \Phi^*$

The chains both overlap and are squeezed by the slits. Accordingly we call this regime the two-dimensional semi-dilute regime (2D-SD regime). The polymer free energy density is the sum of the two-dimensional osmotic contribution (first term) and the second term expresses the entropic confinement:

$$V_{pol} = \delta \frac{k_B T}{a^2} \Big(\frac{a}{\bar{d}} \Big)^{2/3} \bar{\Phi} + \eta \frac{k_B T}{a^2} \Big(\frac{\bar{d}}{a} \Big)^2 \bar{\Phi}^3$$

where $\delta \simeq 2.22$ and $\eta \simeq 1.72$ are numerical prefactors estimated in [11]. The elastic compressibility modulus is deduced:

$$\bar{B}_{\mu}^{pol} \simeq -\frac{25 \delta^2 k_B T}{54 \eta} \frac{d}{a^4} \Big(\frac{a}{\bar{d}} \Big)^{16/3} \bar{\Phi}^{-1} \tag{4.7}$$

iv. $\bar{d} << R_F$ and $\bar{\Phi} << \Phi^*$ or $\bar{d} << \frac{a}{N\bar{\Phi}^2}$ and $\bar{\Phi} >> \Phi^*$

The chains do not overlap, but are squeezed (flat pancakes of thickness $\bar{d}$). The solvent is a two-dimensional dilute solution of polymer chains (2D-D regime). The polymer free energy density is the sum of the two-dimensional gas contribution (first term) and the entropic confinement contribution (second term):

$$V_{pol} = \frac{k_B T}{a^2} \left(\frac{\bar{d}\bar{\Phi}}{Na} \log\Big(\frac{\bar{d}\bar{\Phi}}{Na} \Big) + \alpha \Big(\frac{a}{\bar{d}} \Big)^{2/3} \bar{\Phi} \right)$$

where α is an unknown numerical prefactor of the order of unity. The elastic compressibility modulus is deduced:

$$\bar{B}_{\mu}^{pol} \simeq -\frac{25 \alpha^2 k_B T}{9} N \bar{\Phi} \Big(\frac{a}{\bar{d}} \Big)^{1/3} \frac{d}{\bar{d}^4} \tag{4.8}$$

The analytical expressions obtained by Ligoure et al. show that the contribution of the non-adsorbing polymer to the smectic compressibility modulus is always negative, meaning that the effective intermembrane interaction mediated by the polymer is attractive. Note that these expressions are valid only far from the crossovers between these regimes.

In [9], Bouglet and Ligoure analyze the results of X-ray and neutron scattering experiments on lamellar phases of the system CPCl (cetylpyridiniumchloride)/hexanol/ water/PVP (polyvinylpyrrolidone). They are able to extract the elastic compressibility modulus in the four different regimes. Remarkably the experimental results meet theoretical predictions, with a quantitative agreement concerning the 3D-SD regime and qualitative agreements for the others regimes (because of the uncertainty of the numerical prefactors in expressions (4.5),(4.7),(4.8)). They also check that the assumption $V_{total} = V_{smectic} + V_{polymer}$ holds.

Polarisation effect

The presence of a dielectric polymer between charged membranes may affect electrostatic interactions by reducing the effective permittivity of the solution confined; but the electrostatics itself may affect the distribution of polymer segments. Indeed, the electrostatic field is stronger near the charged membranes than in the middle of the gap. Thus the water molecules, more polarizable than the polymer chains, are attracted to the walls. This results in a modification of the polymer concentration profile between the membranes, which in turn modifies the intermembrane interactions. Whereas the first effect is often taken into account, the second one is ignored most of the time.

The article of Croze and Cates [21] directly address the interdependence of the polymer physics and electrostatics when charged surfaces interact across solutions of neutral polymers. Considering a solution of neutral and non-adsorbing polymers confined between charged surfaces and contacting a reservoir with which it can exchange heat, polymers, and electrolyte, they adopt a mean-field approach and they calculate both ionic and polymeric contributions to the net pressure. They finally show that the coupling between polymer physics and electrostatics enhances polymer depletion from the surfaces and increases the screening of electrostatic interactions with respect to a model that treats polymeric and electrostatics effects as independent. These changes modify the total interaction in a non-additive manner.

In particular, they investigate the effect of this coupling on the phase behavior of polymer-doped smectics. They show that coupled and uncoupled predictions differ most under the following conditions: (i) moderately high surface charge densities (since strong polarization of the polymers requires high fields); (ii) marginal solvency, i.e. near-Θ conditions (where the response in polymer concentration to external energy shifts is maximized); and (iii) polymers containing a large volume of low-dielectric material.

1.2 Interpretation of experimental results

1.2.1 Sample L

In this section, we interpret the result $\bar{B} = 16.6 \pm 2.8$ kPa obtained for this sample. We recall the periodicity and the membrane thickness: $d = 22.8$ nm, $\delta = 2.4$ nm and we note the thickness of the water layers $\bar{d} = d - \delta$. As there is no added salt to the water, all the considerations done on electrostatics in the following are in the limit "no salt".

Ionization rate

We should check that the ionization rate is closer to 1 for this system [38]. This is assumed most of the time in similar studies, but calculations often demonstrates that this is not true, and if it is the case, some effective salt should be taken into account in the calculations.

Electrostatics versus undulations

One can calculate the theoretical values of the elastic compressibility modulus assuming pure undulation or pure electrostatic interaction:

- for electrostatics, one calculates: $\bar{B}_{elec} \simeq 25$ kPa (see equation (4.2))
- for undulations, assuming that $\kappa \simeq 2.2\ k_B T$ (see [6]), one calculates: $\bar{B}_{und} = 340$ Pa (see equation (4.1)).

There are almost two orders of magnitude separating both values, and one deduces that the steric Helfrich repulsion due to the undulations of the membranes is negligible compared to electrostatic repulsion. This result is not very surprising since the system studied is made of charged surfactant molecules (SDS) separated by water layers containing only the counterions.

Some corrections to electrostatics

The preceding result (Helfrich << electrostatics) is reexamined more in details here. Indeed, the electrostatic interaction has been calculated as if the membanes are rigid, flat and parallel. One must examine the effect of undulating membranes on the electrostatic interaction potential. Several effects may arise.

Porcar correction

As presented in the section 1.1.1, very often experimental situations are not well described by the classical Poisson-Boltzmann theory (analytical solution in the limit without salt). Porcar et al. in [80] give a more precise numerical solution, and finally one can estimate the elastic compressibility modulus resulting from this calculation depending on the value of the parameter τ thanks to the curve plotted in Figure 4.2.

We first calculate the parameter $\tau = \frac{\Sigma}{L_B \bar{d}}$ with:

$$\Sigma = 36 + 2.7 * 23 = 98\ \text{Å}^2$$

since we have 2.7 octanol molecules for one SDS molecule, and $\Sigma_{oct} = 23$ Å^2, $\Sigma_{SDS} = 36$ Å^2 (see [6]). This gives $\tau \simeq 0.07$ and thus the electrostatic compressibility modulus calculated with $\bar{B} = \frac{\pi k_B T d}{2 L_B \bar{d}^3}$ must be reduced from 6% of its value.

Counter-ions correlations

In this part, we investigate the weak organization of the counterions near the membranes. This effect should diminish the electrostatic interaction between the membranes (two neighbouring membranes see less each other) and we want to estimate this contribution to the elastic compressibility modulus. We suggest to follow the approach developed by Moreira and Netz in [72] to get the electrostatic inter-wall pressure.

In [72] Moreira and Netz investigate, using Monte Carlo simulations, the counterion distribution close to planar charged walls and particularly when the counterions are confined between two equally charged walls. Roughly, the aim of the authors is "to make the link" between the Poisson-Boltzmann theory, asymptotically exact in the limit of weak coupling (i.e. low surface charge, high temperature and low counterion valence) and the strong-coupling theory (valid in the opposite limit of high surface charge, low temperature and high counterion valence). Please refer to [72] for more details.

They use the simplest formulation of the double layer, consisting of a hard wall with smeared out charge density σ_s and neutralizing point-like counterions with charge valence q, immersed in a strutureless solvent characterized by a dielectric constant, which is assumed to be the same everywhere.

We recall here the main steps of [72] leading to the result that interests us, that is to say the inter-wall pressure. Please refer to [72] for more details.

The Hamiltonian for a system of N counterions of valence q between two charged walls of number density σ_s reads:

$$\frac{H}{k_B T} = \sum_{j=1}^{N-1} \sum_{k=j+1}^{N} \frac{q^2 L_B}{|\mathbf{r}_j - \mathbf{r}_k|} + 2\pi q L_B \sigma_s \Big(\sum_{j=1}^{N} x_j + \sum_{j=1}^{N} (\bar{d} - x_j) \Big) \tag{4.9}$$

where $L_= \frac{e^2}{4\pi\epsilon_0 \epsilon_r k_B T}$ is the Bjerrum length (e is the elementary charge, ϵ is the relative dielectric constant). The first term contains the Coulombic repulsion between the ions, the second term accounts for the electrostatic attraction to the walls. The counterions are confined between the two walls, with $0 < x < \bar{d}$.

The relevant length scale in the system is the Gouy-Chapman length μ, i.e. the distance from the charged wall at which the potential energy of one isolated counterion equals the thermal energy $k_B T$, which from equation (4.9) is found to be:

$$\mu = \frac{1}{2\pi q L_B \sigma_s} \tag{4.10}$$

If one expresses all lengths in units of the Gouy-Chapman length according to

$$\tilde{r} = \frac{r}{\mu} \tag{4.11}$$

the Hamiltonian equation (4.9) can be rewritten as

$$\frac{H}{k_BT} = \sum_{j=1}^{N-1} \sum_{k=j+1}^{N} \frac{\frac{q^2 L_B}{\mu}}{|\tilde{\mathbf{r}_j} - \tilde{\mathbf{r}_k}|} + \sum_{j=1}^{N} \tilde{x_j} + \sum_{j=1}^{N} (\tilde{d} - \tilde{x_j}) \tag{4.12}$$

where we recognise the interaction energy E_{int} between two ions a distance μ apart:

$$\frac{E_{int}}{k_BT} = \frac{q^2 L_B}{\mu} = 2\pi q^3 L_B^2 \sigma_s = \Xi \tag{4.13}$$

Ξ is called the coupling parameter, it includes the effects of varying temperature, surface charge density σ_s and the counterion valence q. The Hamiltonian finally depends only on this single parameter.

Thanks to this parameter, one can define different regimes of coupling:

- $\Xi << 1$: weak-coupling regime where Poisson-Boltzmann theory is valid

- $\Xi >> 1$: strong-coupling regime

- $\Xi \sim 1$: some corrections to the Poisson-Boltzmann theory are required

Let us calculate Ξ in our case:

$$\Xi = 2\pi 1^3 7^2 \frac{1}{98} = \pi$$

so we need to apply some corrections to the Poisson-Boltzmann theory.

The pressure between is extracted through the contact value theorem (the counterion distribution is given by the Poisson-Boltzmann theory to which a numerical correction is added)

$$\tilde{P} = \frac{P}{2\pi L_B \sigma_s^2} = \tilde{\rho}(0) - 1$$

which relates the pressure acting on one wall to the counterion density at that wall. $\tilde{P}$ is the rescaled pressure and $\tilde{\rho}(0) = \rho(0)/(2\pi L_B \sigma_s^2)$ is the rescaled counterion density at one of the walls. The pressure is then expressed as follows:

$$\tilde{P}(\tilde{d}) = \tilde{P}_{PB}(\tilde{d}) + \Xi \tilde{P}_{PB}^{(1)}(\tilde{d}) + O(\Xi^2) \tag{4.14}$$

where in the limit $\tilde{d} >> 1$ (in our case: $\mu = 2.23$ Å, $\tilde{d} = \frac{\bar{d}}{\mu} = \frac{204}{2.23} = 91.5 >> 1$)

$$\tilde{P}_{PB}(\tilde{d}) = \frac{\pi^2}{\tilde{d}^2}$$

$$\tilde{P}_{PB}^{(1)}(\tilde{d}) = -\frac{1}{\tilde{d}^3}\Big(\frac{\zeta(3)}{4} + \frac{\pi^3}{4} + \pi^2 \ln\Big(\frac{\tilde{d}}{\pi}\Big)\Big)$$

Starting from here we can deduce the elastic compressibility modulus. We can rewrite the equation (4.14):

$$P = P_{PB}\Big(1 + \Xi\frac{\tilde{P}^{(1)}_{PB}}{\tilde{P}_{PB}}\Big)$$

where P and P_{PB} are not rescaled pressures. We have then:

$$\frac{\tilde{P}^{(1)}_{PB}}{\tilde{P}_{PB}} = -\frac{1}{\tilde{d}}\Big(\frac{\zeta(3)}{4\pi^2} + \frac{\pi}{4} + \ln\Big(\frac{\tilde{d}}{\pi}\Big)\Big)$$

we deduce:

$$P = P_{PB}\Big(1 - \Xi\frac{1}{\tilde{d}}\Big(0.816 + \ln\Big(\frac{\tilde{d}}{\pi}\Big)\Big) \tag{4.15}$$

Assuming that $\ln(\tilde{d})$ is a slowly varying function compared to $\frac{1}{\tilde{d}}$

$$\frac{\partial P}{\partial \tilde{d}} = \frac{\partial P_{PB}}{\partial \tilde{d}} - \Xi\frac{\alpha}{\tilde{d}}\frac{\partial P_{PB}}{\partial \tilde{d}} + \Xi\frac{\alpha}{\tilde{d}^2}P_{PB}$$

where $\alpha = 0.816 + \ln\Big(\frac{\tilde{d}}{\pi}\Big) = 4.19$, and with

$$\frac{\partial P_{PB}}{\partial \tilde{d}} = -2\frac{\pi^2}{\tilde{d}^3} = -2\frac{P_{PB}}{\tilde{d}}$$

we get

$$\frac{\partial P}{\partial \tilde{d}} = \frac{\partial P_{PB}}{\partial \tilde{d}}(1 - \frac{3}{2}\Xi\frac{\alpha}{\tilde{d}})$$

that is to say

$$\bar{B} = \bar{B}_{elec}(1 - \frac{3}{2}\Xi\frac{\alpha}{\tilde{d}}) = \bar{B}_{elec}(1 - 0.216)$$

The contribution of the counterions correlations to the elastic compressibility modulus is negative and leads to a decrease of $\bar{B}_{elec}$ of ~ 22 %. If we would have derived the complete expression (4.15), we would have found a slightly smaller correction of ~ 20 %.

Conclusion

With both corrections, we find an electrostatic compressibility modulus decreased of ~ 30 %: $\bar{B}^{th}_{elec} \simeq 17.3$ kPa which is in very good agreement with the experimental value $\bar{B}^{exp} = (16.6 \pm 2.8)$ kPa.

Other electrostatic effects

Charged membranes separated by a solvent that does not contain any salt may interact also by electrostatic undulations. This effect has been estimated for two interacting lamellae, by taking into account the wave lengths of undulations that are larger than the gap between the membranes, and these undulations finally appear to be negligible.

We have taken into account the correlations of the counter-ions so we should also investigate the effect of the organization of the ions in the membrane and the coupling between both effects. According to [37], this coupling has also an effect on the dissociation coefficient. These calculations will be done in a near future.

Finally the significant correction is given by the counterions correlations, which appear to be a crucial effect. The electrostatic undulations are certainly negligible because of this dominant effect: the organized counterions prevent the membranes to completely see each other.

1.2.2 Sample M

In this section, we interpret the result $\bar{B} = (6.4 \pm 1.7)$ kPa obtained for this sample with 15 wt % polymer in water, thus the polymer volume fraction in water is $\bar{\Phi} = 0.13$. We recall the periodicity and the membrane thickness: $d = 18.5$ nm, $\delta = 2.1$ nm and as previously we note $\bar{d} = d - \delta$ the interlayer spacing.

First approach

When a macromolecule is dissolved in a solvent the resulting dielectric constant may be affected, depending on the concentration and the nature of the polymer. We have checked the value of the dielectric constant of a 15 wt % PEG solution in water, with a molecular weight of 20 000. Arnold et al. (see [5]) give a graph of the dielectric constant plotted as a function of the PEG wt % and for different molecular weight. We read $\epsilon \simeq 77.5$, which is very close to pure water ($\epsilon \simeq 80$).

The dielectric constant is not affected but there may be a coupling between the polymer and the electrostatic interaction as presented in Section **??**. Let us assume in this approach that the electrostatics does not affect the distribution of the polymer, we thus have:

$$V_{total} = V_{elec} + V_{pol}$$

which leads to the following equation

$$\bar{B}_{total} = \bar{B}_{elec} + \bar{B}_{pol}$$

where $\bar{B}_{elec}$ is given in the previous section: $\bar{B}^{th}_{elec} = 17.3$ kPa (electrostatics corrected from ~ 30 %) or by the experimental value $\bar{B}^{exp}_{elec} = 16.6 \pm 2.8$ kPa.

The aim of this section is thus to determine the polymer contribution to the elastic compressibility modulus.

Let us determine which regime (see section 1.1.2) is relevant for this sample. Note that there is an adsorption interaction between the polymer and the membranes (see [15], [60], [34]), let us assume that this does not modify drastically the bulk polymer fraction in the interlayer spacing. Since the polymer volume fraction in water is $\bar{\Phi} = 0.13$ and the overlapping volume fraction is $\bar{\Phi}^* \simeq 0.034$, the chains overlap and form a net of mesh $\xi \simeq 17$ Å. The interlaying spacing $\bar{d} = 185 - 21 = 164$ Å is well larger than ξ. So

the chains overlap but still remain unsqueezed and the solvent is a three-dimensional semi-dilute solution of polymer chains: we are in the 3D-SD regime.

In the following, we suggest to adapt the approach developed by Ligoure et al. to a situation where the polymer adsorbs on the membranes, in the 3D-SD regime. To our knowledge, the contribution of an adsorbing polymer to the elastic compressibility modulus is not addressed in the literature. We will then discuss the "bulk" contribution term to the free energy. Finally we will present the adsorption contribution.

Calculation

In the 3D-SD regime, the free energy of the polymer is the sum of two contributions:

$$V = \bar{d} f(\bar{\Phi}) + v\bar{\Phi}^{\alpha}$$

where f describes the "bulk" volumic contribution (osmotic pressure) and the second term either a depletion or an adsorption contribution. The parameters v and α will be determined in the following (see paragraph "Adsorption term"). Let us calculate the elastic compressibility modulus at constant chemical potential.

First step: elastic compressibility modulus at constant surface fraction of polymer

$$\frac{\partial V}{\partial \bar{d}}\Big|_{\sigma} = \frac{\partial(\bar{d} f(\bar{\Phi}))}{\partial \bar{d}}\Big|_{\sigma} + \frac{\partial v\bar{\Phi}^{\alpha}}{\partial \bar{d}}\Big|_{\sigma}$$

with $\bar{\Phi} = \frac{2a\sigma}{\bar{d}}$

$$\frac{\partial V}{\partial \bar{d}}\Big|_{\sigma} = f - \frac{2a\sigma}{\bar{d}^2} f' - \alpha v \frac{\bar{\Phi}^{\alpha}}{\bar{d}}$$

$$\bar{B}_{\sigma} = d\frac{\partial^2 V}{\partial \bar{d}^2}\Big|_{\sigma} = \frac{d}{\bar{d}}\Big(\bar{\Phi}^2 f'' + v\alpha(\alpha+1)\frac{\bar{\Phi}^{\alpha}}{\bar{d}}\Big)$$

Second step: calculation of the derivatives

i.

$$\frac{\partial V}{\partial \sigma}\Big|_{\bar{d}} = 2af' + 2av\alpha\frac{\bar{\Phi}^{\alpha-1}}{\bar{d}}$$

$$\frac{\partial^2 V}{\partial \sigma^2}\Big|_{\bar{d}} = \frac{4a^2}{\bar{d}}\Big(f'' + v\alpha(\alpha-1)\frac{\bar{\Phi}^{\alpha-2}}{\bar{d}}\Big)$$

ii.

$$\frac{\partial^2 V}{\partial \bar{d}\partial\sigma} = -\frac{2a}{\bar{d}}\Big(\bar{\Phi} f'' + v\alpha^2\frac{\bar{\Phi}^{\alpha-1}}{\bar{d}}\Big)$$

$$\Big(\frac{\partial^2 V}{\partial \bar{d}\partial\sigma}\Big)^2 = \frac{4a^2}{\bar{d}^2}\Big(\bar{\Phi}^2 f''^2 + v^2\alpha^4\frac{\bar{\Phi}^{2(\alpha-1)}}{\bar{d}^2} + 2\mu\alpha^2 f''\frac{\bar{\Phi}^{\alpha}}{\bar{d}}\Big)$$

Third step: calculation of $\bar{B}_\mu$

$$\bar{B}_\mu = \bar{B}_\sigma - d\Big(\frac{\partial^2 V}{\partial \bar{d}\partial\sigma}\Big)^2 \Big(\frac{\partial^2 V}{\partial \sigma^2}\Big|_{\bar{d}}\Big)^{-1}$$

$$\text{numerator}(\bar{B}_\mu) = \bar{B}_\sigma\Big(\frac{\partial^2 V}{\partial \sigma^2}\Big|_{\bar{d}}\Big) - d\Big(\frac{\partial^2 V}{\partial \bar{d}\partial\sigma}\Big)^2 = -\frac{4a^2 d}{\bar{d}^2} v^2\alpha^2 \frac{\bar{\Phi}^{2(\alpha-1)}}{\bar{d}^2}$$

Finally

$$\bar{B}_\mu = -\frac{\frac{4a^2 d}{\bar{d}^2} v^2\alpha^2 \frac{\bar{\Phi}^{2(\alpha-1)}}{\bar{d}^2}}{\frac{4a^2}{\bar{d}}(f'' + v\alpha(\alpha-1)\frac{\bar{\Phi}^{2(\alpha-1)}}{\bar{d}})}$$

$$\bar{B}_\mu = -\frac{d}{\bar{d}^3}\frac{v^2\alpha^2\bar{\Phi}^{2(\alpha-1)}}{f'' + v\alpha(\alpha-1)\frac{\bar{\Phi}^{\alpha-2}}{\bar{d}}} \tag{4.16}$$

We find an expression similar to the equation (11) of [71], which is negative. The numerator depends only on the second term of the free energy (depletion or adsorption). We discuss now the "bulk" contribution.

Osmotic pressure term

In this section, we suggest to recall two models concerning the osmotic pressure. The first (Cohen et al. approach) is supported by experimental results; the second (Brooks and Cates) is more theoretical. The aim is to obtain a good agreement between both models (that will help us finally to give a value of the monomer length with more confidence).

Phenomenological approach

In [19], the authors give a phenomenological one-parameter equation of state for osmotic pressures of PEG Π:

$$\Pi N^{9/5} = \frac{RT}{M_m \bar{V}}\left(\Big(\frac{\bar{\Phi}}{\bar{\Phi}^*_N}\Big) + \nu\Big(\frac{\bar{\Phi}}{\bar{\Phi}^*_N}\Big)^{9/4}\right) \tag{4.17}$$

where N is the number of monomers in a polymer chain, R is the universal constant, T the temperature, M_m is the monomer molecular weight, $\bar{V}$ is the partial specific volume, ν is an undetermined prefactor, and $\bar{\Phi}^*_N$ is a characteristic N-dependent polymer concentration associated with the crossover between the dilute and semi-dilute regimes ($\bar{\Phi}^*_N \equiv N^{-4/5}/\bar{V}$). The first term is the van't Hoff contribution which is significant in the dilute regime, the second term is the des Cloizeaux contribution, significant in the semidilute regime. The prefactor given in [19] is $\nu = 0.49$.

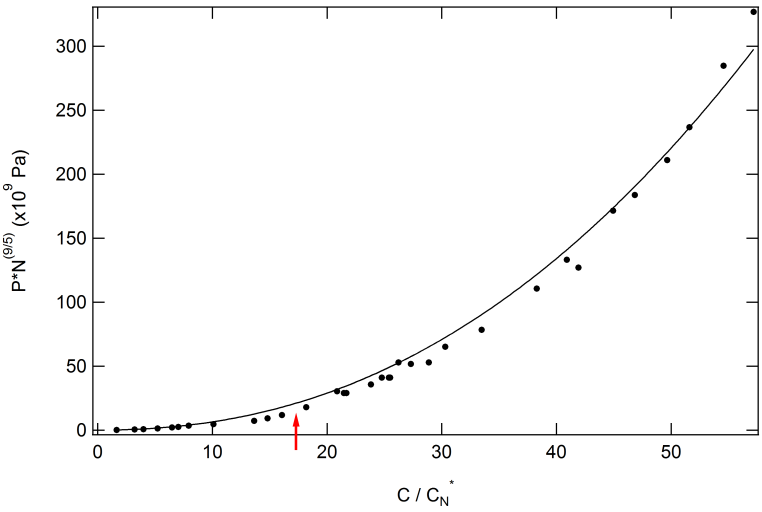

Figure 4.3: Osmotic pressure data of solutions of PEG 20 000 in water plotted according to equation (4.17). The fit gives $\nu = 0.48 \pm 0.01$. The data stem from [1]. The red arrow locates the solution corresponding to the studied sample.

In Figure 4.3, we present a fit performed on data of solutions of PEG 20 000. For the following, we will take the value $\nu = 0.49$, which has been extracted from a fit done on a more extensive set of data (see [19], different molecular weights).

This allows us to extract a value of the osmotic pressure for the volume fraction of polymer that interests us: $\Pi(\bar{\Phi} = 0.13) = 3.421 * 10^5$ Pa.

Theoretical approach

In [71], the "bulk" contribution is $f(\bar{\Phi}) = \beta \frac{k_B T}{a^3} \bar{\Phi}^{9/4}$. We can deduce the pressure:

$$\Pi = \bar{\Phi} \frac{\partial f}{\partial \bar{\Phi}} - f$$

which leads to:

$$\Pi = \frac{5}{4} \beta \frac{k_B T}{a^3} \bar{\Phi}^{9/4}$$

To calculate the pressure with this expression is not easy since we need to know precisely the monomer length a. The literature provides an important range of values: we find $a = 3.5$ $\mathring{A}$ in [45], $a = 4.4$ Å in [7], $a \sim [3.5 - 7.2]$ Å in [19], $a = 6.7$ Å in [44]... If we take $a = 3.5$ Å, we find $\Pi = 2.4 * 10^6$ Pa which is by a factor of 7 larger than the "experimental" value given above. But with $a = 6.7$ Å, we find $\Pi = 3.415 * 10^5$ Pa which is in excellent agreement with the above value. So we consider in all this thesis that $a = 6.7$ Å.

Conclusion

Finally the comparison between both models is constructive and we will take for the following

$$V_{pol}^{osm} = \beta \frac{k_B T}{a^3} d\bar{\Phi}^{9/4}$$

with the monomer length $a = 6.7$ Å (see [44]).

Adsorption term

Considering a semidilute solution of adsorbing polymer in contact with a wall, de Gennes gives in [24] an expression of the interfacial tension γ:

$$\gamma - \gamma_0 = -k_1 \frac{k_B T}{D^2} \left(1 + k_2 \left(\frac{D}{\xi_b} \right)^{5/3} \right) \tag{4.18}$$

where γ_0 is the surface tension of the pure solvent (e. g. water), k_1 and k_2 are unkown numerical prefactors, D is the extrapolation length and ξ_b is the mesh size in the bulk solution. We have $\xi_b = a\bar{\Phi}_b^{-3/4}$ where $\bar{\Phi}_b$ is the polymer volume fraction in the bulk solution far from the wall. In this model, the walls are characterised by a "free energy of sticking" and only flexible chains that repel each others are considered. The correlation length ξ is the only polymer length taken into account.

Since k_1 and k_2 are unkown prefactors, we take a equivalent approach given by the Gibbs relation:

$$\frac{\partial \gamma}{\partial \mu} = -\Gamma$$

where Γ is the surface excess of polymer. By integrating this relation ([31] equation (1.6)), we get

$$\gamma = -\int \Gamma \mathrm{d}\mu \simeq \text{constant} - \Gamma_\infty \mu + ... \tag{4.19}$$

where μ is the chemical potential of the polymer and is given by (c is the polymer concentration in water):

$$\mu = \frac{\partial f}{\partial c} = \frac{\partial f}{\partial \bar{\Phi}} \frac{\partial \bar{\Phi}}{\partial c}$$

and

$$f(\bar{\Phi}) = \beta \frac{k_B T}{a^3} \bar{\Phi}^{9/4}.$$

Thus,

$$\mu = \frac{9}{4} \beta \frac{k_B T}{a^3} \bar{\Phi}^{5/4} \frac{M_p}{\rho_p} \tag{4.20}$$

where M_p is the molar mass in weight of the polymer and ρ_p is the density of the polymer [4]. Identifiying equation 4.19 with 4.18, we deduce that $\Gamma_\infty \simeq \frac{n_{mono}}{a^2}$, where

n_{mono} is the number of moles of monomers in the excess surface corresponding to a surface of a^2. Finally we write

$$V_{pol}^{ads} = \text{constant} - 2\frac{n_{mono}}{a^2}\frac{M_p}{\rho_p}\frac{9}{4}\beta\frac{k_BT}{a^3}\bar{\Phi}^{5/4} \equiv -v\bar{\Phi}^{\alpha}.$$

since the constant has no influence when we derive to obtain $\bar{B}$. The factor 2 accounts for both interfaces. We can write:

$$\alpha = 5/4$$

$$v = 2\frac{n_{mono}}{a^2}\frac{M_p}{\rho_p}\frac{9}{4}\beta\frac{k_BT}{a^3}$$

Estimate

Let us estimate the contribution to the elastic compression modulus with the equation 4.16 which rewrites

$$\bar{B}_{\mu} = -\frac{d}{\bar{d}^3}\frac{v^2\alpha^2\bar{\Phi}^{2(\alpha-1)}}{f'' - v\alpha(\alpha-1)\frac{\bar{\Phi}^{\alpha-2}}{\bar{d}}}.$$

Assuming that the second term of the denominator is negligible [1],

$$\bar{B}_{\mu} \simeq -\frac{d}{\bar{d}^3}\frac{v^2\alpha^2\bar{\Phi}^{2(\alpha-1)}}{f''}.$$

which rewrites

$$\bar{B}_{\mu} \simeq -\frac{d}{\bar{d}^3}\frac{45}{16}\Big(\frac{M_p}{\rho_p}\Big)^2\beta\frac{k_BT}{a^3}\Big(\frac{n_{mono}}{a^2}\Big)^2\bar{\Phi}^{1/4}.$$

As we ignore the exact value of n_{mono}, we better estimate it by setting $\bar{B}_{\mu} = -10$ kPa, which is roughly what we expect regarding experimental results. Doing so, we obtain $n_{mono} \simeq 3.12 * 10^{-27}$ mol $\equiv 0.2 * 10^{-2}$ monomer which is small compared to the expected 1 monomer / a^2 in the semi-dilute regime. This indicates that we are in the concentrated regime and that this approach is not appropriate.

[1] With $n_{mono} \simeq 3.12 * 10^{-27}$ mol, the second term of the denominator in equation 4.16 is smaller than f'' by one order of magnitude, so the approximation holds.

Second approach

In [88, 87], Semenov et al. consider the interaction between two plates coated by adsorbed polymer layers and propose a mean-field approach that takes into account the effect of chain-ends. In particular, in the case of concentrated solutions, the potential of interaction between the plates writes (see [87], equations (78) and (84)):

$$V = 4a' \frac{8}{v^2 N R_g b^2 c} u_{int}(x) \qquad \text{with} \qquad x = \frac{2h}{R_G} \tag{4.21}$$

$$\text{where} \qquad u_{int}(x) = \frac{1}{x} \sum_{n=-\infty}^{\infty} g\Big(\frac{4\pi^2 n^2}{x^2}\Big) \tag{4.22}$$

$$\text{with} \qquad g(u) = \frac{1-(u+1)e-u}{u-1+e-u}. \tag{4.23}$$

$a' = a/\sqrt{6}$ (a is the monomer length), $v = 35$ Å^3 is the excluded volume of a monomer (deduced from a fit of osmotic pressure data $P = vN_ARTc'$, c' is the concentration of monomers in mol/L), $N \simeq 425$ is the number of monomers in a chain, $R_G = 56$ Å is the radius of gyration of the polymer chains, $b = D/a$ [(2)] where D is the extrapolation length and $c = 2.1\ 10^{27}$ m^{-3} is the monomer concentration. b is related to the strength of adsorption, we have $b = 1$ in the case of a strong adsorption and $b \sim 3-5$ in the case of weaker adsorption (PEG on SDS/octanol membranes). Note that $2h$ is equivalent to the interlayer spacing: $2h = \bar{d}$.

u_{int} has been calculated numerically and is presented in Figure 4.4. The interaction potential between two adsorbing plates is repulsive between 0 and R_G and proportional to $1/h$. This accounts for the repulsion between chain-ends that occurs in the middle of the gap, richer in chain-ends (see [87] page 70-71 for a rigourous demonstration). Then the potential becomes attractive between $\sim 3\ R_G$ and $\sim 4.5\ R_G$, and is finally weakly attractive beyond $4.5\ R_G$. Naively, this attraction results from the depletion of chain-ends near the membranes (chain-ends are in excess is the gap, see Figure 4.5).

We see from Figure 4.4, and by plotting the second derivative of u_{int}, that the region where the curvature is negative starts around $\sim 4R_G$ and goes until $\sim 4.5R_G$, beyond it is still negative but very weak. We do not know precisely the radius of gyration of the polymer in a concentrated solution. We have $R_G = 56$ Å in dilute solutions where the coils are swollen, thus we may expect a smaller radius of gyration in the concentrated regime and we may have $2h \simeq 4R_G$. Let us now estimate an order of magnitude of the polymer contribution to the elastic compressibility modulus in the region of negative curvature.

We first check that we are in the concentrated regime. The correlation length in the concentrated regime is given by $\xi = a'\sqrt{6/(12vc)} \simeq a$ which shows that the chains are gaussian and that the loops at the interfaces are larger enough. Since the crossover

[2]Here b denotes a parameter related to the adsorption strength, it is not the Burgers vector. This notation is temporarily used for this paragraph (to keep the same notation as in the literature).

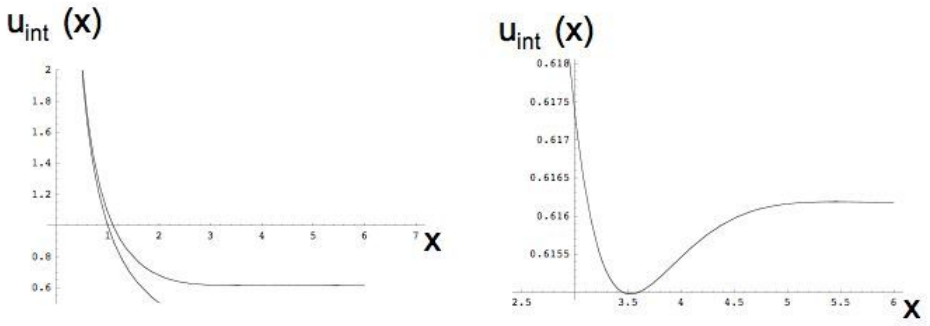

Figure 4.4: Interaction potential u_{int} between two adsorbing plates in equilibrium with a concentrated solution, as a function of the reduced separation $x = 2h/R_G$ between the plates. On the right, the curve that finishes at $x \simeq 2$ is the asymptote to the u_{int} curve for $x < 2$: this is a $1/h$ power law that takes into account the repulsion between chain-ends that occurs in the middle of the gap, richer in chain-ends. An enlargement of the curve between $x = 3$ and $x = 6$ is presented on the left. It shows an attractive minimum for a separation between the plates $2h \simeq 3.5\ R_G$. Note that the absolute zero is equivalent to the 0.616 tick approximately.

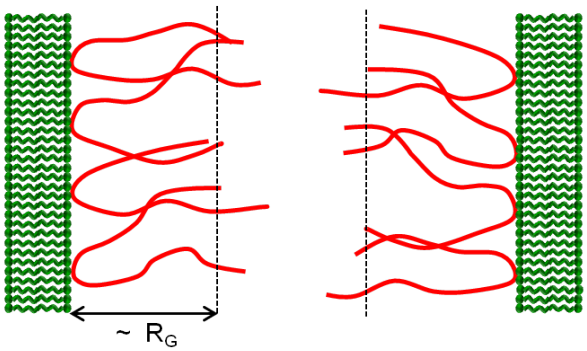

Figure 4.5: Representation of the spatial distribution of the adsorbing polymer between the membranes. Chain-ends are in excess in the gap whereas the solution is depleted in chain-ends near the membranes, which leads to an attraction between the membranes.

concentration $c_2 = 1/(v\sqrt{Nb^2}) \simeq 1.4\,10^{27}\mathrm{m}^{-3}$ (with $b = 1$) is inferior to the monomer concentration $c = 2.1\ 10^{27}\ \mathrm{m}^{-3}$ with $b = 1$, we can make sure that we are in the concentrated regime.

With $\bar{B} = d\frac{\partial^2(2V)}{\partial d^2}$, we get

$$\bar{B}_{pol} = -d * 2 * 4a' \frac{8}{v^2 N R_g b^2 c} * \frac{u''_{int}(x=4)}{4R_G^2}$$

thus

$$\bar{B}_{pol} \simeq -185 * 10^{-10} * 2 * \frac{10^{-6}}{4 * 56^2 * 10^{-20}} = -300 \text{ Pa}.$$

The value obtained is very low, there is roughly a factor 30 separating this calculated contribution and the expected value $\bar{B}_{pol}^{exp} \simeq -10$ kPa from experimental results. Note that we observe a similar discrepancy in the case of supported membranes (on mica surfaces) immerged in a PEG solution of the same concentration [59].

Charge dilution

As the polymer adsorbs on the membranes, some tails of polymer may slot into the membranes, between the charged polar heads, and thus produce an increase in the surface area per charged head. The electrostatic interaction would thus be modified and this is what we propose to estimate in this section.

Thanks to X-rays scattering measurements, we know the periodicity d and the membrane thicknesse δ of samples L and M (Chapters 3 and **??** and [34]). Based on simple geometric considerations, we can thus estimate the fraction of polymer in the membrane for sample M.

For sample L, we have:

$$\delta + \bar{d} = d \tag{4.24}$$

$$\frac{\delta}{\bar{d}} = \frac{\Phi_m}{\Phi_w} \tag{4.25}$$

$$\Sigma \frac{\delta}{2} = v_{SDS} + 2.7 v_{octanol} \tag{4.26}$$

where v_{SDS} and $v_{octanol}$ denote the volume occupied by one molecule of SDS and 2.7 molecules of octanol (since $A/S = 2.7$) in the membrane, corresponding to a surface area per charged head $\Sigma = 98$ Å^2. We have: $d = 228$ Å, $\delta = 24$ Å, $\Phi_m = 0.105$ (volumic fraction of membrane), $\Phi_w = 1 - \Phi_m = 0.895$ (volumic fraction of water).

From equation 4.24, we deduce $\bar{d} = 204$ Å. This allows to check that equation 4.25 is satisfied. Finally, from equation 4.26 we obtain $v_{SDS} + 2.7 v_{octanol} = 1176$ Å^3.

Similarly, for sample M, we have:

$$\delta_M + \bar{d}_M = d_M \tag{4.27}$$

$$\frac{\delta_M}{\bar{d}_M} = \frac{\Phi_m + \Phi_p^m}{1 - (\Phi_m + \Phi_p^m)} \tag{4.28}$$

$$\Sigma_M \frac{\delta_M}{2} = v_{SDS} + 2.7 v_{octanol} + v_p \tag{4.29}$$

where Φ_p^m denotes the volume fraction of polymer in the membrane, and v_p the volume of polymer in the membrane corresponding to a surface area per charged head Σ_M. We have: $d_M = 185$ Å, $\delta_M = 21$ Å, and $\Phi_m = 0.105$ as previously.

- From equation 4.27, we deduce $\bar{d}_M = 164$ Å.
- Then, from equation 4.28, since we know Φ_m, we are able to calculate the polymer volume fraction in the membrane, we obtain $\Phi_p^m = 8.5\,10^{-3}$. Thus, the total volume fraction of the membrane is $\Phi_m^{total} = \Phi_m + \Phi_p^m = 0.1135$ and there is 7.5 % of polymer (in volume) in the membrane, and 92.5 % of alcohol and surfactant.
- Knowing $v_{SDS} + 2.7 v_{octanol} = 1176$ Å^3 from sample L, we deduce $v_p = \frac{1176*7.5}{92.5} = 95$ Å^3.
- Finally, we obtain $\Sigma_M = \frac{2}{\delta_M}(v_{SDS} + 2.7 v_{octanol} + v_p) = 121$ Å^2 from equation 4.29.

So the surface area per charged head increases from 98 Å^2 to 121 Å^2 when the polymer concentration in water is increased from 0 to 15 wt.%.

Let us estimate the elastic compressibility modulus with the Poisson-Boltzmann theory given in equation 4.2 with $\Sigma_M = 121$ Å^2 instead of $\Sigma = 98$ Å^2, and with $d = 228$ Å: $\bar{B}_{elec} = 22.9$ kPa instead of 23.1 kPa. Consequently, the effect of the dilution of the charge due to polymer insertion in the membrane is very weak and can be neglected.

Conclusion

In this section, we have attempted to calculate the contribution of an adsorbing polymer to the elastic compressibility modulus. An adsorption theory for the semi-dilute regime is not appropriate, thus we should consider the concentrated regime. A mean-field equilibrium theory that takes into account the chain-ends effects, applied to the concentrated regime, fails to interpret the experimental result.

We should certainly in the future estimate the effect of the coupling between the electrostatics and the polymer, that might be non-negligible since we are in the situation of high charge density.

1.2.3 Samples N and O

Both samples are located in the phase diagram on the dilution line $C_p = 3.8$ leading to the critical point Pc2. So the polymer volume fraction in water is $\bar{\Phi} = 0.032$ which is very close to $\bar{\Phi}^* \simeq 0.034$.

For both samples, we are very close to crossovers and the theory of Ligoure *et al.* is not applicable. We discuss these results more in details in the Discussion (Chapter 5).

2 Theoretical aspects about dislocations: radius and energy of nucleation

Most of experimental studies done on lamellar mesophases with the SFA technique provide force-separation profiles that exhibit the same features: it is a set of parabolae which are periodically spaced, the amplitude of the oscillations and accordingly their slope, increases as the separation between the two surfaces decreases. The parabolae often lie on a baseline that forms a long-range attractive background.

The article that provides the most complete theory about the behavior of lamellar mesophases confined between the two SFA surfaces is the article of Richetti et al. [83]. In this article, the authors developed a model to account for the specific confining geometry of the SFA. This model is based on an array of concentric edge dislocation loops that allows an homeotropic alignment of the layers in a space of variable thickness. They calculate the energy of the confined sample and deduce the equilibrium dislocation loops radii as well as the elastic force, first by neglecting the line energies of the dislocations. Then, they take the line energies into account, which modifies the previous equations and in particular leads them to consider the energy barrier that the system needs to pass to nucleate a dislocation loop. All these developments are done considering that the Burgers vector is equal to unity $b = 1$.

In this section, we propose to adapt their approach to a situation where the Burgers vector b is unknown but constant. All the computations are presented in details (this is not the case in the original article) and we provide additional graphs, helpful for a better understanding of the processes studied. At the same time, the main ideas and conclusions, useful for interpreting the experimental results, are recalled.

2.1 Problem setting

2.1.1 Geometry of the system

In the SFA, the geometry of the two confining surfaces is that of two crossed cylinders (see Chapter 2). The vertical separation, h, between the two surfaces reads:

$$h(r,\theta) = e + \frac{r^2}{2R} + \mathcal{O}\left(\left(\frac{r}{R}\right)^4, \theta\right) \tag{4.30}$$

where (r, θ) are the cylindrical coordinates in the plane parallel to the axes of the two cylinders and e is the thickness at center (closest separation of the two cylinders). If terms of order higher than two in r/R are neglected (in the reported experiments $e/R < 10^{-4}$) the angular coordinate θ is irrelevant and the crossed-cylinder geometry is equivalent to a sphere of radius R near a flat surface.

The space into which the confined sample exists can be divided into N adjacent torus-like cells, Figure 4.6. Each cell of rank i is delimited by an inner radius, ρ_i, where the thickness, $h(\rho_i)$, is an integral multiple of the reticular distance: $h(\rho_i) = n_i d$, and

an outer radius, ρ_{i+b}, where the thickness is increased by b layers periods: $h(\rho_{i+b}) = (n_i + b)d$. In this picture every cell of rank $i > 0$ contains one edge dislocation loop of Burgers vector b located at a radius $\tilde{r_i}$ (Figure 4.6). For the central cell $i = 0$, the inner radius is zero. Whether it contains a dislocation loop or not depends on thickness at center e.

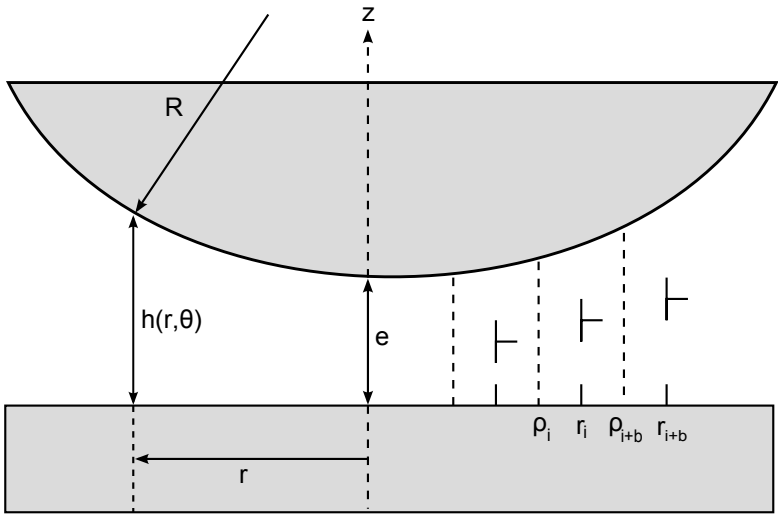

Figure 4.6: Schematic diagram showing a lamellar mesophase confined between a sphere of radius R and a flat plane. An array of concentric dislocation loops is introduced in order to fill up the confining space of varying thickness under homeotropic alignment. The sample is arbitrarily divided into N adjacent torus-like cells. Each cell is delimited by an inner radius, ρ_i, where the thickness, $h(\rho_i)$, is an integral multiple of the reticular distance: $h(\rho_i) = n_i d$, and an outer radius, ρ_{i+b}, where the thickness is increased by b layers periods: $h(\rho_{i+b}) = (n_i + b)d$. b is the Burgers vector of the dislocations. In this picture every cell of rank $i > 0$ contains one edge dislocation loop of radius $\tilde{r_i}$. For the central cell $i = 0$, the inner radius is zero. Whether it contains a dislocation loop or not depends on thickness at center e.

2.1.2 Energy

To good approximation, the cells are considered to be independent, i.e., two adjacent loops do not interact (the strain fields due to the presence of dislocations do not overlap, please refer to [83] for more details). Thus the energy of the array of dislocations, E_T, may be obtained by summing the contributions from each cell, E_{bi}: $E_T = \sum_{i=0}^{[N_{max}/b]} E_{bi}$, where the upper boundary N_{max}, is defined by the sample thickness at the edge of the mica surfaces (typically 1-2 mm).

Note: the index bi is only used in the sums over the whole cells. In other calculations, for simplicity, we use the indexes i and $i + b$ for two consecutive cells.

Following Nallet and Prost [74], the different elastic contributions in each cell are

now evaluated. The cell $i = 0$ plays a special role and will be treated separately. Three contributions should be retained for every cell $i > 0$:

i. The first one is the *wedge confinement energy*, E_{W_i}, due to the elastic distorsion of the smectic material [78]. Over the region spanning from the inner radius, ρ_i, to the dislocation loop radius, r_i, the smectic layers are stretched, whereas from the loop radius, r_i, to the outer radius, ρ_{i+b}, the layers are compressed. Hence:

$$E_{W_i} = \frac{\bar{B}}{2}\left(\int_{\rho_i}^{r_i} 2\pi r \mathrm{d}r \int_0^{h_i} \left(\frac{h(r) - h_i}{h_i} \right)^2 \mathrm{d}z + \int_{r_i}^{\rho_{i+b}} 2\pi r \mathrm{d}r \int_0^{h_{i+b}} \left(\frac{h(r) - h_{i+b}}{h_{i+b}} \right)^2 \mathrm{d}z \right) \tag{4.31}$$

where $\bar{B}$ is the compression modulus, $h_i = h(\rho_i) = n_i d$, $h_{i+b} = h(\rho_{i+b}) = (n_i + b)d$ are the thicknesses of the unstrained material for $\rho_i < r < r_i$ and $r_i < r < \rho_{i+1}$, respectively (z is the coordinate perpendicular to the layers).

ii. The second contribution arises from the distorsion field around the dislocation core, inside the parabola of strain [26]. According to Kléman, this *far-field energy*, E_{F_i}, reads [64]:

$$E_{F_i} = 2\pi r_i \gamma \tag{4.32}$$

$$\gamma = \frac{\bar{B}\lambda b d}{2} \tag{4.33}$$

where λ is the penetration length, $\lambda^2 = K/\bar{B}$ and K the bending elastic modulus.

iii. The third contribution originates from the core of the defect itself. For a dislocation of small Burgers vector, like a pore in a membrane, the core energy should not be described by a continuum theory and a microscopic approach is more appropriate [64]. To first approximation, the *core energy*, E_{C_i}, can be considered as a linear function of the pore radius:

$$E_{C_i} = 2\pi r_i \gamma' \tag{4.34}$$

where the phenomenological parameter γ' ($\gamma' > 0$) is an energy per unit length.

For the case of dislocations of large Burgers vectors, the core energy can still be described by a continuum theory [74] based on the fact that an edge dislocation of Burgers vector b can be viewed as a $+\pi, -\pi$ disclination pair of length bd, the energy of which is calculated in a nematic-like description [64]:

$$\gamma' = \frac{\pi}{2} K \ln \frac{b}{2} + e_\mu \tag{4.35}$$

where e_μ is a direct measure of the short-scale core energy (in our case, this scale is given by the thickness δ of the surfactant lamellae).

The net elastic energy, E_i, stored in each cell i is then:

$$E_i = E_{W_i} + E_{F_i} + E_{C_i} \tag{4.36}$$

Minimizing equation 4.36 with respect to r_i gives the equilibrium radius $\tilde{r_i}$ of the dislocation loop:

$$\tilde{r_i}\frac{\bar{B}}{2}\left(h_i\Big(\frac{h(\tilde{r_i})-h_i}{h_i}\Big)^2 - h_{i+b}\Big(\frac{h(\tilde{r_i})-h_{i+b}}{h_{i+b}}\Big)^2\right) + \gamma + \gamma' = 0 \tag{4.37}$$

Computation:
Let us compute the first term of the right-hand side of equation 4.31:

$$\begin{aligned}\int_{\rho_i}^{r_i} 2\pi r\mathrm{d}r \int_0^{h_i}\left(\frac{h(r)-h_i}{h_i}\right)^2 \mathrm{d}z &= \int_{\rho_i}^{r_i} 2\pi r\mathrm{d}r\left(\frac{h(r)-h_i}{h_i}\right)^2 h_i \\ &= 2\pi h_i\int_{\rho_i}^{r_i} r\Big(\frac{e+r^2/2R-h_i}{h_i}\Big)^2\mathrm{d}r \\ &= 2\pi h_i^2\frac{R}{3}\Big(\frac{h(r_i)-h_i}{h_i}\Big)^3.\end{aligned}$$

Whence

$$E_{W_i} = \frac{\bar{B}}{2}2\pi\frac{R}{3}\Big[\Big(\frac{h(r_i)-h_i}{h_i}\Big)^3 h_i^2 - \Big(\frac{h(r_i)-h_{i+b}}{h_{i+b}}\Big)^3 h_{i+b}^2\Big]$$

and

$$\Big(\frac{\mathrm{d}E_i}{\mathrm{d}r_i}\Big)_{\tilde{r_i}} = \bar{B}\pi\frac{R}{3}3\frac{\tilde{r_i}}{R}\Big[\Big(\frac{h(r_i)-h_i}{h_i}\Big)^2 h_i - \Big(\frac{h(r_i)-h_{i+b}}{h_{i+b}}\Big)^2 h_{i+b}\Big] + 2\pi(\gamma+\gamma') = 0$$

thus

$$\frac{\bar{B}}{2}\tilde{r_i}\Big[\Big(\frac{h(r_i)-h_i}{h_i}\Big)^2 h_i - \Big(\frac{h(r_i)-h_{i+b}}{h_{i+b}}\Big)^2 h_{i+b}\Big] + (\gamma+\gamma') = 0.$$

□

The next two steps are to calculate the energy of the whole array of dislocations, $E_T = E_0 + \sum_{i=1}^{[N_{max}/b]} E_{bi}(\tilde{r_{bi}})$, knowing $\tilde{r_{bi}}$ from equation 4.37, and then to determine the net interaction, F_T, between the plane and the sphere: $F_T(e) = -\frac{\mathrm{d}E_T}{\mathrm{d}e}$.

2.2 First computation: the line energies $\gamma+\gamma' = 0$ are neglected

2.2.1 Equilibrium radii

In order to understand the contribution of each term in equation 4.36, we shall first forget the two line energies E_{F_i} and E_{C_i} (i.e. set $\gamma + \gamma' = 0$ in equation 4.37). The equilibrium radius, noted $\bar{r_i}$ in this case, is then given by

$$\frac{\bar{r_i}^2}{2R} + e = \sqrt{n_i(n_i+b)}d. \tag{4.38}$$

Computation:
Let us compute the first term of the right-hand side of equation 4.31:

$$\begin{aligned}\int_{\rho_i}^{r_i} r\mathrm{d}r \int_0^{h_i} \left(\frac{h(r)-h_i}{h_i}\right)^2 \mathrm{d}z &= \int_{\rho_i}^{r_i} r\mathrm{d}r\Big(\frac{h(r)^2}{h_i} - 2h(r) + h_i\Big) \\ &= \int_{\rho_i}^{r_i} r\mathrm{d}r\Big(\frac{1}{h_i}\big(e+\frac{r^2}{2R}\big)^2 - 2\big(e+\frac{r^2}{2R}\big) + h_i\Big)\end{aligned}$$

using equation 4.30. Then

$$\begin{aligned}\int_{\rho_i}^{r_i} r\mathrm{d}r \int_0^{h_i} \left(\frac{h(r)-h_i}{h_i}\right)^2 \mathrm{d}z &= \int_{\rho_i}^{r_i} \mathrm{d}r\left[\frac{r^5}{4h_iR^2} + \frac{r^3}{R}\big(\frac{e}{h_i}-1\big) + r\big(\frac{e^2}{h_i} - 2e + h_i\big)\right] \\ &= \frac{r_i^6-\rho_i^6}{24h_iR^2} + \frac{r_i^4-\rho_i^4}{4R}\big(\frac{e}{h_i}-1\big) + \frac{r_i^2-\rho_i^2}{2h_i}(e-h_i)^2.\end{aligned}$$

Similarly, we find for the second term:

$$\int_{r_i}^{\rho_{i+b}} r\mathrm{d}r \int_0^{h_{i+b}} \left(\frac{h(r)-h_i}{h_i}\right)^2 \mathrm{d}z = \frac{\rho_{i+b}^6-r_i^6}{24h_{i+b}R^2} + \frac{\rho_{i+b}^4-r_i^4}{4R}\big(\frac{e}{h_{i+b}}-1\big) + \frac{\rho_{i+b}^2-r_i^2}{2h_{i+b}}(e-h_{i+b})^2.$$

Summing these two terms, we first gather the terms depending on ρ_i (T_i), then the terms depending on ρ_{i+b} (T_{i+b}) and finally the terms depending on r_i (S_i):

- $$\begin{aligned}T_i &= \pi\bar{B}\Big[\frac{\rho_i^6}{24h_iR^2} + \frac{\rho_i^4}{4R}\big(\frac{e}{h_i}-1\big) + \frac{\rho_i^2}{2h_i}(e-h_i)^2\Big] \\ &= \pi\bar{B}\frac{\rho_i^2}{2h_i}\Big(\frac{\rho_i^4}{12R^2} + \frac{\rho_i^2}{2R}(e-h_i) + (e-h_i)^2\Big)\end{aligned}$$

but $h_i = e + \frac{\rho_i^2}{2R}$, thus

$$T_i = \frac{\pi\bar{B}\rho_i^6}{24h_iR^2} = \frac{\pi\bar{B}R}{3}\frac{(n_id-e)^3}{n_id}$$

since $h_i = n_id$.

- Similarly we get

$$T_{i+b} = \frac{\pi \bar{B} \rho_{i+b}^6}{24 h_{i+b} R^2} = \frac{\pi \bar{B} R}{3} \frac{((n_i + b)d - e)^3}{(n_i + b)d}.$$

- Finally we gather the terms depending on r_i:

$$\begin{aligned} S_i &= \frac{\pi \bar{B} r_i^2}{2} \Big[\frac{r_i^4}{12R^2} \big(\frac{1}{h_i} - \frac{1}{h_{i+b}} \big) + \frac{r_i^2}{2R} \big(\frac{e}{h_i} - \frac{e}{h_{i+b}} \big) + \frac{(e - h_i)^2}{h_i} - \frac{(e - h_{i+b})^2}{h_{i+b}} \Big] \\ &= \frac{\pi \bar{B} r_i^2}{2 h_i h_{i+b}} \Big[\frac{r_i^4}{12R^2} (h_{i+b} - h_i) + \frac{e}{2R} r_i^2 (h_{i+b} - h_i) + h_{i+b}(e - h_i)^2 - h_i (e - h_{i+b})^2 \Big] \end{aligned}$$

where $h_{i+b} - h_i = bd$, thus

$$\begin{aligned} S_i &= \frac{\pi \bar{B} bd}{2 h_i h_{i+b}} r_i^2 \Big[\frac{r_i^4}{12R^2} + \frac{e}{2R} r_i^2 + (e^2 - h_i h_{i+b}) \Big] \\ &= \frac{\pi \bar{B} b}{2 n_i (n_i + b) d} r_i^2 \Big[\frac{r_i^4}{12R^2} + \frac{e}{2R} r_i^2 + (e^2 - n_i (n_i + b) d^2) \Big] \end{aligned}$$

Finally,

$$E_{W_i} = S_i - T_i + T_{i+b}. \tag{4.39}$$

To find the equilibrium radius $\bar{r_i}$, we have to minimize E_{W_i} with respect to r_i, that is to say minimize S_i with respect to r_i (b constant). Let us set [3]

$$S_i = \alpha (r_i^2)^3 + \beta (r_i^2)^2 + \gamma (r_i^2)$$

where $\alpha = \delta \frac{1}{12R^2}$, $\beta = \delta \frac{e}{2R}$, $\gamma = \delta (e^2 - n_i (n_i + b) d^2)$ and $\delta = \frac{\pi \bar{B} b}{2 n_i (n_i + b) d}$. We have

$$\frac{\partial S_i}{\partial r_i^2} = 3\alpha (r_i^2)^2 + 2\beta (r_i^2) + \gamma = 0 \qquad \Rightarrow \qquad r_i^2 = \frac{-\beta + \sqrt{\beta^2 - 3\alpha\gamma}}{3\alpha}$$

that is:

$$\bar{r_i}^2 = 2R(\sqrt{n_i (n_i + b)} d - e).$$

□

We emphasize the fact that all the cells are considered here as independent.

2.2.2 Elastic energy

The elastic energy of each cell, $E_i(\bar{r_i}) = E_{W_i}(\bar{r_i})$ is then computed:

$$E_{i>0} = \frac{\pi \bar{B} R b d^2}{3} \Big[2n_i + b - 2\sqrt{n_i (n_i + b)} \Big]. \tag{4.40}$$

[3] The coefficients α, β, γ, δ are used temporarily to simplify the notations. γ is not a line energy.

Computation:
We have $E_i(\bar{r_i}) = S_i(\bar{r_i}) - T_i + T_{i+b}$ and

$$\begin{aligned} S_i(\bar{r_i}) &= \frac{\pi\bar{B}Rb}{n_i(n_i+b)d}(\sqrt{n_i(n_i+b)}d - e)\Big[\frac{(\sqrt{n_i(n_i+b)}d-e)^2}{3} \\ &\qquad + e(\sqrt{n_i(n_i+b)}d - e) + (e^2 - n_i(n_i+b)d^2)\Big] \\ &= \frac{\pi\bar{B}Rb}{3n_i(n_i+b)d}(\sqrt{n_i(n_i+b)}d - e)(e^2 + e\sqrt{n_i(n_i+b)}d - 2n_i(n_i+b)d^2) \\ &= \frac{\pi\bar{B}Rbd}{3}\Big(3e - 2\sqrt{n_i(n_i+b)}d - \frac{e^3}{n_i(n_i+b)d^2}\Big). \end{aligned}$$

The elastic energy is

$$\begin{aligned} E_{i>0} &= \frac{\pi\bar{B}R}{3}\Big(\frac{((n_i+b)d-e)^3}{(n_i+b)d} - \frac{(n_id-e)^3}{n_id} + 3bde - 2bd^2\sqrt{n_i(n_i+b)} - \frac{be^3}{n_i(n_i+b)d}\Big) \\ &= \frac{\pi\bar{B}Rbd^2}{3}\Big(2n_i + b - 2\sqrt{n_i(n_i+b)}\Big). \end{aligned}$$

□

Remarkably the cells of rank $i > 0$ do not contribute to the interaction between the surfaces since the elastic energy $E_{i>0}$ does not depend on the separation at center e. In other words, the attraction of the stretched areas exactly cancels the repulsion due to the compressed areas.

We have now to consider the central cell $i = 0$ which extends from center $\rho_0 = 0$ (n_0 layers) up to a radius ρ_{0+b} where the thickness $h(\rho_b)$ equals $n_bd = (n_0 + b)d$, the lowest possible integral multiple of d. The free energy in this cell can be integrated either with or without a dislocation loop from equation 4.31. The excess elastic free energy reads

$$\Delta E_0 = E_{W_0}^{\text{with}} - E_{W_0}^{\text{without}} = \frac{\pi\bar{B}db}{24e_0^2R^2}r_0^2(r_0^4 + 6Rer_0^2 + 12R^2(e^2 - e_0^2)) \tag{4.41}$$

where $e_0 = \sqrt{n_0(n_0+b)}d$.

Computation:

- $E_{W_0}^{\text{without}} = \pi\bar{B}\displaystyle\int_0^{\rho_b} r\mathrm{d}r\int_0^{h_b}\left(\frac{h(r)-h_b}{h_b}\right)^2\mathrm{d}z = T_b$

  in this case, $h_b = (n_0 + b)d$ and we have $n_b = n_0$.

- $E_{W_0}^{\text{with}} = \pi\bar{B}\Big(\displaystyle\int_{\rho_0=0}^{r_0} r\mathrm{d}r\int_0^{e}\left(\frac{h(r)-e}{e}\right)^2\mathrm{d}z + \int_{r_0}^{\rho_b} r\mathrm{d}r\int_0^{h_b}\left(\frac{h(r)-h_b}{h_b}\right)^2\mathrm{d}z\Big)$
  $= S_0 - T_0 + T_b$

where $e = n_0 d$ and $h_b = (n_0 + b)d$ (in this case, $n_b \neq n_0$) and with

$$S_0 = \frac{\pi \bar{B} b}{2n_0(n_0+b)d}\Big(e^2 - n_0(n_0+b)d^2 + \frac{e}{2R}r_0^2 + \frac{r_0^4}{12R^2}\Big)$$
$$T_0 = 0 \qquad \text{(because } \rho_0 = 0\text{)}$$
$$T_b = \frac{\pi \bar{B} R}{3}\frac{(n_b d - e)^3}{n_b d} \qquad \text{(where } n_b = n_0 + b\text{)}$$

Finally, setting $e_0 = \sqrt{n_b(n_b - b)}d = \sqrt{n_0(n_0+b)}d$, we obtain

$$\Delta E_0 = S_0 = \frac{\pi \bar{B} b d}{2e_0^2} r_0^2 \Big(e^2 - e_0^2 + \frac{e}{2R}r_0^2 + \frac{r_0^4}{12R^2}\Big)$$

that is to say

$$\Delta E_0 = \frac{\pi \bar{B} b d}{24 e_0^2 R^2} r_0^2 (12R^2(e^2 - e_0^2) + 6Rer_0^2 + r_0^4).$$

□

Equation 4.41 indicates that a continuous transition occurs when the quadratic term changes sign. We have to consider two situations:

i. $e > e_0$

As long as the thickness at center e is larger than e_0, the quadratic term is positive, so all the terms are positive in equation 4.41 and the excess energy is minimum for $\bar{r_0} = 0$ (see Figure 4.7): no dislocation is present in the central cell ($n_b = n_0$). The layers are compressed over the whole cell and the net interaction is repulsive.

ii. $e < e_0$

In this case, equation 4.41 becomes

$$\Delta E_0 = \frac{\pi \bar{B} b d}{24 e_0^2 R^2} r_0^2 (r_0^4 + 6Rer_0^2 - 12R^2(e_0^2 - e^2)).$$

The reduced discriminant is given by

$$\Delta = 9R^2e^2 + 12R^2(e_0^2 - e^2) = 3R^2(4e_0^2 - e^2) \simeq 9R^2e_0^2 \qquad \text{(because } e \simeq e_0\text{)}$$

therefore

$$\bar{r_0}^2 \simeq -3Re + \sqrt{9R^2e_0^2} = 3R(e_0 - e).$$

Thus when the separation between the walls is reduced, as soon as $e < e_0$, the free energy exhibits a negative minimum at the equilibrium radius $\bar{r_0}$ (see Figure 4.7) given by:

$$\bar{r_0} \simeq \sqrt{3R(e_0 - e)} \tag{4.42}$$

and the excess elastic free energy is

$$\Delta E_0(\bar{r_0}) \simeq -\frac{3\pi R \bar{B} b d}{8e_0^2}(e_0 - e)^2(e + e_0) \simeq -\frac{3\pi R \bar{B} b d}{4e_0}(e_0 - e)^2. \tag{4.43}$$

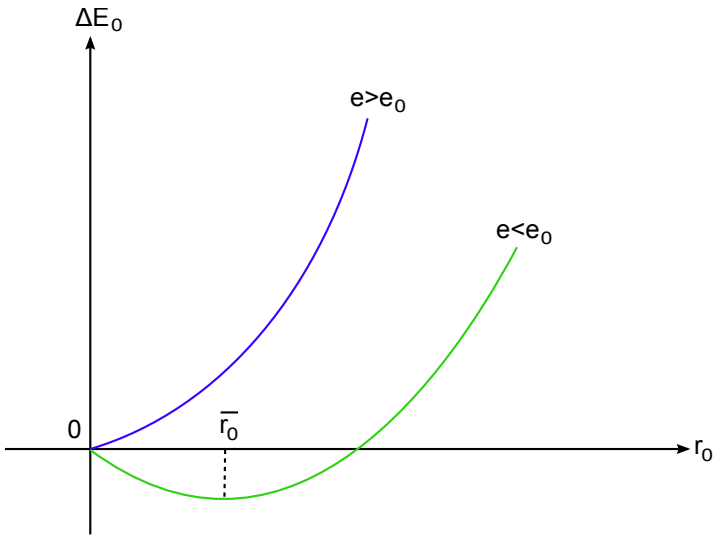

Figure 4.7: Scheme representing the excess energy of the central cell as a function of r_0, for two different sample thicknesses. When the sample thickness e is larger than the thickness $e_0 = \sqrt{n_0(n_0+b)}d$, the excess energy is minimum for $\bar{r_0} = 0$, thus no dislocation is present in the central cell. When the sample thickness e crosses $e_0 = \sqrt{n_0(n_0+b)}d$ and becomes smaller, the excess energy exhibit a negative minimum at the equilibrium radius $\bar{r_0} \simeq \sqrt{3R(e_0-e)}$ (equation (4.42)): a dislocation loop is nucleated.

Eventually, the loops expand continuously when the surfaces are approached. A new loop appears each time the thickness at center e crosses a value $e_0(n_b) = \sqrt{n_b(n_b-b)}d$ where n_b is an integer. Conversely, the dislocation loops shrink and disappear when the surfaces are pulled apart. That is application of an external strain, dilating the central cell (initially a perfect smectic slab with no dislocation) would cause dislocations to move into it from the sides in order to reduce the net external force on the surface to zero.

2.2.3 Elastic force

The elastic energy of the central cell depends explicitly on the sample thickness at center e, and remarkably the total elastic interaction between the two surfaces arises exclusively from this cell. The elastic force reads

$$F_T(e) = -\frac{\mathrm{d}E_T}{\mathrm{d}e}.$$

But $E_T = E_{W_0} + \sum_{i=1}^{[N_{max}/b]} E_{W_{bi}}$, where $E_{W_{bi}}$ is independent of e (see equation 4.40), thus

$$F_T(e) = -\frac{\mathrm{d}E_T}{\mathrm{d}e} = -\frac{\mathrm{d}E_0}{\mathrm{d}e} = -\frac{\mathrm{d}T_b}{\mathrm{d}e} = -\frac{\mathrm{d}\left(\frac{\pi\bar{B}R}{3}\frac{(n_b d-e)^3}{n_b d}\right)}{\mathrm{d}e} \equiv \pi R\bar{B}\frac{(e-n_0 d)^2}{n_0 d} = 2\pi R f_T \tag{4.44}$$

where we have taken $E_0 = E_{W_0} = E_{W_0}^{\text{without}}$ since the process to nucleate a dislocation loop is very quick and the loop rapidly expands to the following cell. So the energy of the central cell is in average represented by T_b.

f_T is the compression elastic energy per unit area of n_b layers of a smectic material homeotropically aligned between two flat plates a distance e apart. Equation 4.44 turns out to identify with the classical Derjaguin equivalence, which relates the force between a sphere against a plate scaled by the radius of curvature to the density of interaction free energy between two parallel plates [27]. The applicability of the Derjaguin approximation was not expected to hold as the elastic potential f_T is long-range. The reason lies obviously in the exact vanishing of the interaction for all cells of rank $i > 0$ resulting from the regular array of dislocation loops.

We first note that the elastic interaction $F_T(e)$ strictly vanishes each time the separation at center e is an integral multiple of d, the equilibrium layer thickness at zero stress. Moreover, the elastic contribution is always repulsive, whatever the sign of the applied strain. The force-distance profile is a set of parabolae, each one corresponding to a different number of layers n_0 at center. Two adjacent parabolae intercept at the critical thicknesses $e_0(n_0) = \sqrt{n_0(n_0-b)}d$ for which the first loop of the array is either nucleated or annihilated. At thermodynamic equilibrium the force profile is fairly periodic, the separation between two adjacent intersects rapidly approaching the reticular distance d as n_0 increases. The amplitude of the oscillations, and accordingly their slope, increases as the separation between the two surfaces decreases. The minima of the parabolae line up on a baseline $F_T = 0$.

Experimental data (see Chapter 3 for example, or [84, 83, 40]) actually exhibit a very similar oscillatory force profile except that the baseline (i.e. the envelope on which lie the minima of each oscillation) clearly forms a long-range attractive background. Before proceeding further in the comparison, we need to consider how the elastic force (equation (4.44)) is affected by the line energies, i.e., the far-field energy (equation (4.32)) and the core energy (equation (4.34)).

Note that the Burgers vector does not appear in this equation 4.44, so the elastic compressibility modulus is not modified by b.

2.3 Second computation: the line energies $\gamma+\gamma'$ are taken into account

2.3.1 Force

It is intuitive that the line tensions will reduce the equilibrium radius (equation 4.38) in each cell, i.e., $\tilde{r_i} < \bar{r_i}$. Consequently, all the elastic energies $E_i(\tilde{r_i})$ are expected to depend explicitly on e and every cell of rank i will now contribute to the net interaction between the two surfaces. The force (equation 4.44) can be rewritten as

$$F_T(e) = -\sum_{i=0}^{[N_{max}/b]} \left(\frac{\partial E_{bi}}{\partial e} + \frac{\partial E_{ib}}{\partial r_{bi}} \frac{\mathrm{d}r_{bi}}{\mathrm{d}e} \right). \tag{4.45}$$

The Euler-Lagrange condition imposes $\partial E_{bi}/\partial r_{bi} = \partial E_i/\partial r_i = 0$. With the definition of the wedge elastic energy (equation 4.31) and since $\partial E_i/\partial e = \partial E_{W_i}/\partial e$,

$$\frac{\partial E_i}{\partial e} = \pi R \bar{B} \Big[h_i \Big(\frac{h(\tilde{r_i}) - h_i}{h_i} \Big)^2 - h_{i+b} \Big(\frac{h(\tilde{r_i}) - h_{i+b}}{h_{i+b}} \Big)^2 \Big]. \tag{4.46}$$

Combining equations 4.37 and 4.46, the contribution of every loop is simply obtained:

$$\frac{\partial E_i}{\partial e} = -\frac{2\pi R}{\tilde{r_i}} (\gamma + \gamma'). \tag{4.47}$$

Finally the total elastic force between the surfaces is

$$F_T(e) = \pi R \bar{B} \frac{(e - n_0 d)^2}{n_0 d} + 2\pi R (\gamma + \gamma') \sum_{i=0}^{[N_{max}/b]} \frac{1}{\tilde{r_{bi}}}. \tag{4.48}$$

The new expression of the force deviates from the Derjaguin equivalence (equation 4.44): the fortunate cancellation of the interaction over the cells of rank $i > 0$ no longer occurs when the line energies are taken into account. An additional interaction proportional to the line energies $\gamma + \gamma'$ is now superimposed on the Derjaguin form. This new term is always positive i.e. repulsive at all separations.

Note that in this calculation one considers that the edge dislocations have a Burgers vector b independent of the rank of the cell i. This assumption is not valid for samples of large thicknesses [74]: b increases as the confinement thickness increases. In that case, in equation (4.48), the term $\gamma + \gamma'$ depends on b, that is on i and the supplementary term reads $2\pi R \sum_{i=0}^{[N_{max}/b]} \frac{1}{\tilde{r_{bi}}} (\gamma_{bi} + \gamma'_{bi})$ with γ_{bi} and γ'_{bi} given by equation (4.33) and (4.35).

2.3.2 Equilibrium radii $\tilde{r_i}$

In this case, the equilibrium radii $\tilde{r_i}$ reads

$$\tilde{r_i} = \Big(\frac{e_i \tilde{\lambda} R}{2b} \Big)^{1/3} \tag{4.49}$$

where $e_i = \sqrt{n_i(n_i+b)}d$.

Computation
Starting from equation (4.37), we have

$$\left(h_i\Big(\frac{h(\tilde{r_i})-h_i}{h_i}\Big)^2 - h_{i+b}\Big(\frac{h(\tilde{r_i})-h_{i+b}}{h_{i+b}}\Big)^2\right) = -2\frac{\gamma+\gamma'}{\tilde{r_i}\bar{B}} = -\frac{d\tilde{\lambda}}{\tilde{r_i}}$$

$$\begin{aligned}
&\frac{(h(\tilde{r_i})-h_i)^2}{h_i} - \frac{(h(\tilde{r_i})-h_{i+b})^2}{h_{i+b}} = -\frac{d\tilde{\lambda}}{\tilde{r_i}}\\
&h(\tilde{r_i})^2\Big(\frac{1}{h_i}-\frac{1}{h_{i+b}}\Big) + h_i - h_{i+b} = -\frac{d\tilde{\lambda}}{\tilde{r_i}}\\
&h(\tilde{r_i})^2\Big(\frac{bd}{h_i h_{i+b}}\Big) - bd = -\frac{d\tilde{\lambda}}{\tilde{r_i}}\\
&\frac{h(\tilde{r_i})^2}{e_i^2} = 1 - \frac{\tilde{\lambda}}{b\tilde{r_i}}.
\end{aligned}$$

Thus,

$$h(\tilde{r_i}) = e_i\sqrt{1-\frac{\tilde{\lambda}}{b\tilde{r_i}}} \simeq e_i\Big(1-\frac{\tilde{\lambda}}{2b\tilde{r_i}}\Big)$$

since $b \geq 1$, $\tilde{r_i}$ is of the order of a few tens of micrometers and $\tilde{\lambda}$ is of the order of a few tens of nanometers. We can rewrite

$$\frac{\tilde{r_i}^2}{2R} + e \simeq e_i\Big(1-\frac{\tilde{\lambda}}{2b\tilde{r_i}}\Big)$$

and finally we have to solve

$$\tilde{r_i}^3 + 2R(e-e_i)\tilde{r_i} + \frac{e_i\tilde{\lambda}R}{b} = 0.$$

When $e - e_i > 0$ no real solution exists (no dislocation is present in the central cell), so we consider $e - e_i < 0$. The physical solution is finally given by the double-root (discriminant $\Delta = 0$, two real solutions with one double-root)

$$\tilde{r_i} = \Big(\frac{e_i\tilde{\lambda}R}{2b}\Big)^{1/3} \tag{4.50}$$

where $e_i = \frac{\tilde{r_i}^2}{2R} + e = \sqrt{n_i(n_i+b)}$.

□

The exact magnitude of the second term of the right-hand side of equation (4.48) is hard to estimate as it results from the summation of a slowly decaying function $(1/\tilde{r_i})$ up to large values of i. For an estimation of this term with $b = 1$, please refer to the original article [83].

2.3.3 Energy, critical radius r_c and equilibrium radius $\tilde{r_0}$

From a dynamical point of view, the integration of line energies introduces a significant qualitative difference. Let us consider again the central cell and include the far-field and the core energy contributions into the excess elastic energy. Equation 4.41 now contains an additional positive linear term:

$$\Delta E_0 = \frac{\pi \bar{B} d b}{24 e_0^2 R^2}(r_0^6 + 6Re r_0^4 + 12R^2(e^2 - e_0^2)r_0^2 + \frac{24 e_0^2 R^2 \tilde{\lambda}}{b} r_0) \tag{4.51}$$

where $\tilde{\lambda} = 2(\gamma + \gamma')/\bar{B}d$ has the dimension of a length (it would be the penetration length if the core energy were ignored). The emergence of a new loop would still be driven by the applied strain but the nature of the transition is now first-order-like. Indeed, we have to consider two situations:

i. $e > e_0$

   All the terms in equation 4.51 are positive so ΔE_0 is minimum for $\tilde{r_0} = 0$ (no dislocation in the central cell, see Figure 4.8).

ii. $e < e_0$

   In this case, when r_0 increases, the linear term in r_0 first dominates, then the negative term in r_0^2 balances (totally or partially) the linear term, which produces a local maximum; finally the higher powers of r_0 (r_0^4 and r_0^6) dominates and ΔE_0 starts to increase again, which gives a minimum (see Figure 4.8).

   The critical thickness, e_0, is shifted towards a lower separation $e_c = e_0 - \epsilon$. When $e < e_c$, the excess free energy ΔE_0 exhibits two minima: a metastable minimum at $r_0 = 0$ and a negative one at $\tilde{r_0}$ separated by an activation barrier $\Delta E_0(r_c)$ (see Figure 4.9).

For the experimentally relevant limit $r^2 << Re$ the shift ϵ and the equilibrium radius $\tilde{r_0}$ can be estimated to first order as:

$$\epsilon = e_0 - e_c \simeq \frac{3}{2}\left(\frac{\tilde{\lambda}^2 e_0^2}{2Rb^2}\right)^{1/3} \tag{4.52}$$

and

$$\frac{\tilde{r_0}^2}{2R} \simeq \frac{2}{3}\epsilon. \tag{4.53}$$

Computation:
$\Delta E_0 = 0$ that is $r_0^6 + \alpha r_0^4 + \beta r_0^2 + \delta r_0 = 0$, with

$$\alpha = 6Re$$
$$\beta = 12R^2(e^2 - e_0^2)$$
$$\delta = \frac{24 e_0^2 R^2 \tilde{\lambda}}{b}.$$

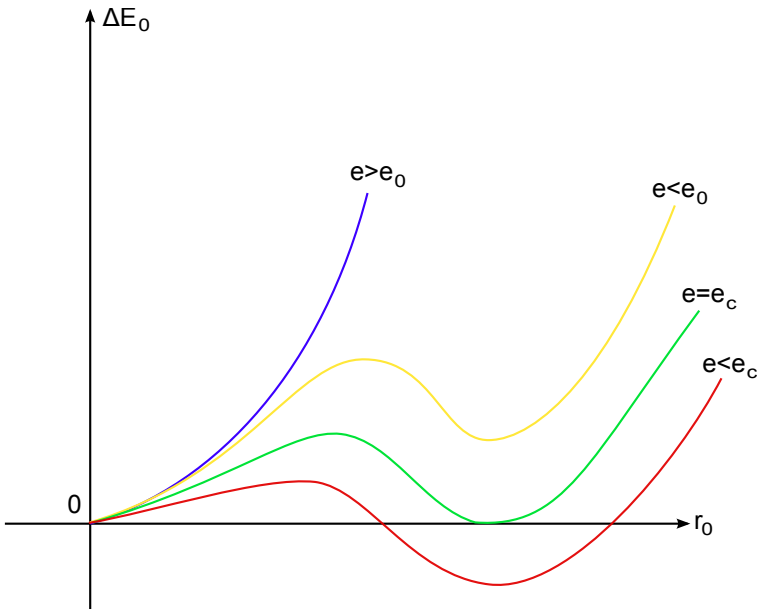

Figure 4.8: Excess energy of the central cell as a function of r_0, for several sample thicknesses. When the sample thickness e is larger than the thickness $e_0 = \sqrt{n_0(n_0+b)}d$, the excess energy is minimum for $\tilde{r_0} = 0$, thus no dislocation is present in the central cell. When the sample thickness e crosses $e_0 = \sqrt{n_0(n_0+b)}d$ and becomes smaller, the excess energy exhibit a minimum which becomes negative for a critical sample thickness e_c: a dislocation loop is nucleated.

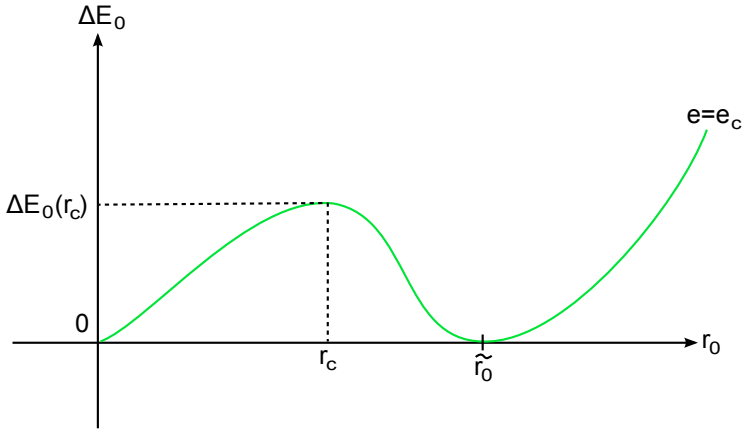

Figure 4.9: Excess energy of the central cell for a sample thickness e_c, showing that the system needs to pass an energy barrier $\Delta E_0(r_c)$ (equation (4.57)) before the nucleation of a dislocation is possible. The critical radius r_c, beyond which a thermally activated pore will grow spontaneously to reach the equilibrium radius $\tilde{r_0}$ is given in equation (4.54); the equilibrium radius $\tilde{r_0}$ is given by equations (4.53) and (4.52).

But $Re = R\sqrt{n_0(n_0+b)}d \simeq Rn_0d$, let us calculate its order of magnitude:

$$Rn_0d \simeq 2 * 10^{-2} * 10^{-8} * n_0 \ \text{m}^2$$

that is

$$6Re \simeq 12 * 10^2 * n_0 \ \ \mu\mathrm{m}^2,$$

thus we can consider that $r_0^2 << 6Re$ and neglect r_0^6 before αr_0^4. So $\tilde{r_0}$ should satisfy

$$\alpha r_0^4 + \beta r_0^2 + \delta r_0 = 0 \qquad \Leftrightarrow \qquad r_0(\alpha r_0^3 + \beta r_0 + \delta) = 0.$$

The solutions are $r_0 = 0$ and r_0 such that $r_0^3 - \frac{\beta}{\alpha} r_0 + \frac{\delta}{\alpha} = 0$. Here we want a double root (according to the appearance of the curve of ΔE_0 as a function of r_0), which imposes

$$4\Big(\frac{-\beta}{\alpha}\Big)^3 + 27\Big(\frac{\delta}{\alpha}\Big)^2 = 0$$

$$\iff \qquad (12)^3 R^6 (e_0^2 - e^2)^3 = \frac{27}{4} 6Re (24)^2 \frac{e_0^4 R^4 \tilde{\lambda}^2}{b^2}$$

$$\iff \qquad (e_0^2 - e^2)^3 = \frac{27}{2} \frac{e_0^4 e \tilde{\lambda}^2}{Rb^2}$$

With $e_0^2 - e^2 = (e_0 - e)(e_0 + e) \simeq 2e_0(e_0 - e)$ (since $e \simeq e_0$), we obtain

$$(e_0 - e)^3 = \frac{27}{16} \frac{e_0^2 \tilde{\lambda}^2}{Rb^2}.$$

Thus the shift ϵ is found to be

$$\epsilon = e_0 - e = \frac{3}{2}\Big(\frac{e_0^2 \tilde{\lambda}^2}{2Rb^2}\Big)^{1/3}.$$

With $e_0 \simeq e$, the double root is given by

$$\tilde{r_0} = \Big(\frac{\delta}{2\alpha}\Big)^{1/3} = \Big(\frac{2Re_0^2 \tilde{\lambda}}{eb}\Big)^{1/3} \simeq \Big(\frac{2Re_0 \tilde{\lambda}}{b}\Big)^{1/3}$$

and using the expression of ϵ to replace $e_0 \tilde{\lambda}$, the equilibrium radius rewrites finally

$$\tilde{r_0} \simeq 2\sqrt{\frac{R\epsilon}{3}} \qquad \text{that is to say} \qquad \frac{\tilde{r_0}^2}{2R} \simeq \frac{2}{3}\epsilon.$$

Note: this result is found again saying

i. $(\Delta E_0)_{\tilde{r_0}} = 0$ so $\tilde{r_0}(\tilde{r_0}^3 + (-\beta/\alpha)\tilde{r_0} + \delta/\alpha) = 0$

ii. ΔE_0 extremum at $\tilde{r_0}$ so $\Big(\frac{\partial \Delta E_0}{\partial r_0}\Big)_{\tilde{r_0}} = 0$ that is $4\alpha \tilde{r_0}^3 - 2\beta \tilde{r_0} + \delta = 0$

$$\text{i.} \quad \Rightarrow \quad \tilde{r_0}^3 + \frac{-\beta}{\alpha}\tilde{r_0} + \frac{\delta}{\alpha} = 0$$
$$\text{ii.} \quad \Rightarrow \quad \tilde{r_0}^3 + \frac{-\beta}{2\alpha}\tilde{r_0} + \frac{\delta}{4\alpha} = 0$$

so

$$\frac{-\beta}{2\alpha}\tilde{r_0} + \frac{3\delta}{4\alpha} = 0 \quad \text{that is} \quad \tilde{r_0} = \frac{3\delta}{2\beta} \quad \text{subtracting ii. to i.}$$

or

$$\tilde{r_0}(-3\tilde{r_0}^2 + \frac{\beta}{\alpha}) = 0 \quad \text{that is} \quad \tilde{r_0} = \Big(\frac{\beta}{3\alpha}\Big)^{1/2} \quad \text{subtracting 4ii. to i.}$$

that is to say $\frac{\tilde{r_0}^2}{2R} \simeq \frac{2}{3}\epsilon$. □

2.3.4 Critical radius

The critical radius r_c, beyond which a thermally activated pore will grow spontaneously to reach the equilibrium radius $\tilde{r_0}$, reads at first order

$$\frac{r_c^2}{2R} \simeq \frac{2-\sqrt{3}}{3}\epsilon. \tag{4.54}$$

Computation:
r_c is given by the maximum of ΔE_0 as a function of r_0, that is

$$\Big(\frac{\partial \Delta E_0}{\partial r_0}\Big)_{r=r_c} = 0 \qquad \Leftrightarrow \qquad 4\alpha r_c^3 - 2\beta r_c + \delta = 0.$$

In particular, the maximum r_c and minimum $\tilde{r_0}$ are given by

$$4\alpha r_0^3 - 2\beta r_0 + \delta = 0. \tag{4.55}$$

But $\tilde{r_0}$ satisfies also

$$\alpha\tilde{r_0}^4 - \beta\tilde{r_0}^2 + \delta\tilde{r_0} = 0 \qquad \text{since} \qquad \Delta E_0(\tilde{r_0}) = 0$$

$$\Rightarrow \qquad \alpha\tilde{r_0}^3 - \beta\tilde{r_0} + \delta = 0 \qquad \Rightarrow \qquad \delta = -\alpha\tilde{r_0}^3 + \beta\tilde{r_0}. \tag{4.56}$$

Injecting equation 4.56 in equation 4.55,

$$\alpha(4r_0^3 - \tilde{r_0}^3) + \beta(-2r_0 + \tilde{r_0}) = 0.$$

Let us take $r_0 = k\tilde{r_0}$, we have

$$\alpha(4k^3 - 1)\tilde{r_0}^3 + \beta(-2k+1)\tilde{r_0} = 0 \quad \text{that is} \quad \tilde{r_0}(\alpha(4k^3-1)\tilde{r_0}^2 + \beta(-2k+1)) = 0.$$

The solutions are $\tilde{r_0} = 0$ (trivial) and $\tilde{r_0} = \left(\frac{\beta}{3\alpha}\right)^{1/2}$ (refer to the *Note* above), so:

$$\alpha(4k^3 - 1)\frac{\beta}{3\alpha} + \beta(-2k + 1) = 0$$
$$\iff \beta\Big(\frac{4k^3 - 1}{3} - 2k + 1\Big) = 0.$$

Thus k satisfies

$$2k^3 - 3k + 1 = 0 \quad \text{i.e.} \quad (k - 1)(2k^2 + 2k - 1) = 0$$

and the solutions are $k = 1$, that is to say $r_0 = \tilde{r_0}$, or $k = \frac{-1\pm\sqrt{3}}{2}$, but $r_c < 0$ is impossible so $k = \frac{-1+\sqrt{3}}{2}$. Finally

$$r_c = \frac{\sqrt{3} - 1}{2}\tilde{r_0},$$

and with $\frac{\tilde{r_0}^2}{2R} \simeq \frac{2}{3}\epsilon$, we get

$$\frac{r_c^2}{2R} \simeq \Big(\frac{\sqrt{3} - 1}{3}\Big)^2 \frac{2}{3}\epsilon \simeq \frac{2 - \sqrt{3}}{3}\epsilon.$$

□

2.3.5 Activation barrier

The nucleation of the pore will occur at the critical separation e_c in a reasonable time, if the activation barrier $\Delta E_0(r_c)$ is not too large compared to $k_B T$. Otherwise, no dislocation can be initiated, and a metastable state will be built. The system will remain in this state even at separations lower than e_c until the height of the barrier is lowered enough in applying a further strain to allow the nucleation to be initiated. To first order, the energy barrier at e_c can be evaluated as

$$\Delta E_0(r_c) = \simeq \frac{2\sqrt{3} - 3}{3}\frac{\pi R\bar{B}bd}{e_0}\epsilon^2 \tag{4.57}$$

Computation:

$$\Delta E_0(r_0 = r_c) = \frac{\pi\bar{B}db}{24e_0^2R^2}(\alpha r_c^4 - \beta r_c^2 + \delta r_c) = \frac{\pi\bar{B}db}{24e_0^2R^2}(\alpha(k\tilde{r_0})^4 - \beta(k\tilde{r_0})^2 + \delta(k\tilde{r_0}))$$

But $\alpha\tilde{r_0}^4 - \beta\tilde{r_0}^2 + \delta\tilde{r_0} = 0$, thus eliminating δ in previous equation and using $\tilde{r_0} =$

$(\beta/3\alpha)^{1/2}$, we get

$$\begin{aligned}\Delta E_0(r_c)\Big(\frac{\pi\bar{B}db}{24e_0^2R^2}\Big)^{-1} &= \alpha(k^4-k)\frac{\beta^2}{9\alpha^2} - \beta(k^2-k)\frac{\beta}{3\alpha} \\ &= \frac{\beta^2}{3\alpha}k(k-1)\Big(\frac{k^2+k+1}{3}-1\Big) \\ &= \frac{\beta^2}{9\alpha}k(k-1)(k^2+k-2) \\ &= \frac{\beta^2}{9\alpha}\frac{3(2\sqrt{3}-3)}{4}.\end{aligned}$$

Since $k = \frac{\sqrt{3}-1}{2}$, and using $\frac{\beta}{3\alpha} = \tilde{r_0}^2 \simeq \frac{4}{3}\epsilon$ and $\beta = 12R^2(e_0^2 - e^2) \simeq 24R^2e_0\epsilon$, we obtain

$$\Delta E_0(r_c) = \frac{2\sqrt{3}-3}{3}\frac{\pi R\bar{B}db}{e_0}\epsilon^2.$$

□

Chapter 5

Discussion

1 Experimental aspects

1.1 SFA technique

1.1.1 Thermodynamic equilibrium

The SFA technique is non-model dependent since we obtain directly the elastic compressibility modulus. The analysis done to infer the elastic compression modulus relies only on a crucial assumption: the system must be at any time at the thermodynamic equilibrium. This is what we discuss now.

The lamellar mesophases of the system SDS/ octanol/ water/ PEG exhibit a significant viscosity. If we turn over vials that contain 2.5 g of sample, we have to wait from a few seconds to several minutes until the sample has flown, depending on the location of the sample in the phase diagram. In the dilute part of the phase diagram, the samples are less viscous, the viscosity increases then when the membrane concentration increases; very close to the critical point Pc2, it seems that the viscosity decreases again a little bit. It is difficult to quantify, by means of rheology measurements, these observations made on samples in vials since the structural organization of lamellar mesophases is perturbed when sheared [29, 85].

Nevertheless, we have tried, at very low shear rates, to get an order of magnitude of the viscosity of sample N. These measurements have been performed with a rheometer Haake MARS III (Thermo Scientific), the sample is sheared between a plate and a cone (radius=35 mm, angle=2°). In Figures 5.1 and 5.2, we present some measurements of the viscosity performed at controlled rate. We do not observe any Newtonian plateau, and the order of magnitude of the viscosity is huge: for a shear rate of 10^{-4} s^{-1}, we have approximately $\eta \sim 10^4 - 10^5$ Pa.s.

But these samples exhibit also elastic properties. In vials of 60 mL, we observe in samples submitted to gravity, that some filaments form and drag along the remaining matter. With the rheometer, we have performed creep-recovery measurements on sample N. This sample exhibits a quasi rubber-like behavior (Figure 5.3): we obtain almost

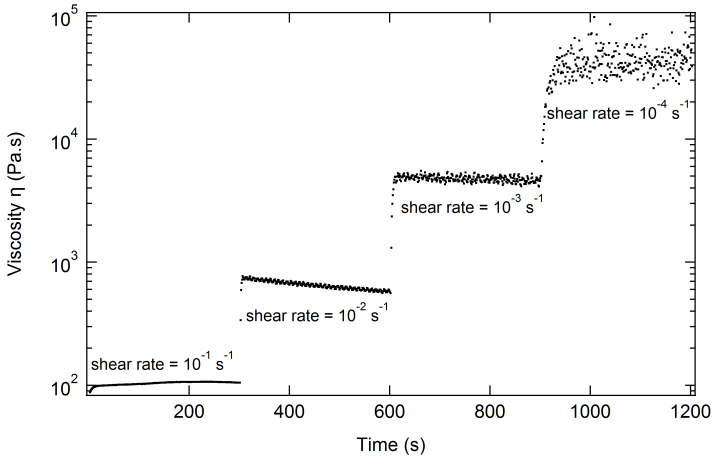

Figure 5.1: Measurement of the viscosity as a function of time, for different shear rates. Each step lasts 5 minutes, to let some time to the sample to reach an equilibrium, and a point is recorded every second (sample N). For the lowest shear rate, 10^{-4} s^{-1}, the measurement becomes imprecise: the points are scattered, a larger integration time would have improved this. For a shear rate of 10^{-4} s^{-1}, we have approximately $\eta \sim 5\,10^4$ Pa.s.

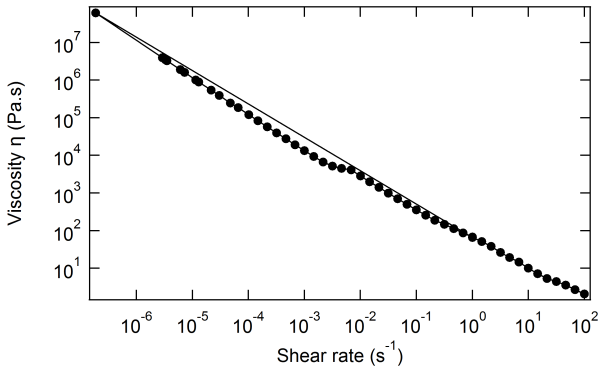

Figure 5.2: Measurement of the viscosity as a function of the shear rate, performed first from 1 to 10^{-7} s^{-1} and then from 1 to 100 s^{-1}. Each point is recorded every 70 s (sample N). 10^{-7} s^{-1} is the lowest shear rate that the rheometer is able to achieve. We still do not see a Newtonian plateau. For a shear rate of 10^{-7} s^{-1}, we have approximately $\eta \sim 10^8$ Pa.s.

a step equivalent to the excitation, this is why we cannot extract, from the creep curve, the viscosity with a good precision. The elasticity seems to dominate the viscosity. We have confirmed this observation by measuring the elastic and loss moduli (G' and G" resp.) as a function of the oscillation frequency (Figure 5.4). Both moduli appear to be parallel, the elastic modulus being larger than the loss modulus, showing that the elasticity dominates the viscosity.

Finally it is difficult to get a precise and reproducible order of magnitude of the

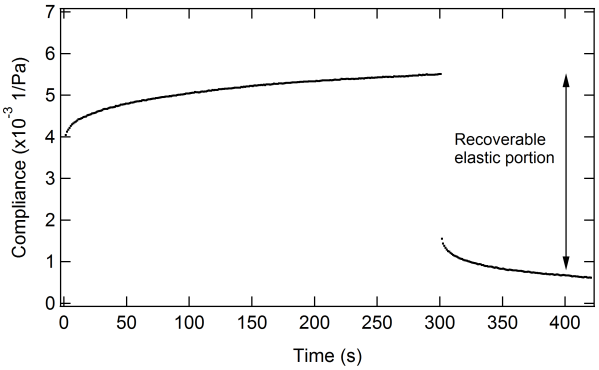

Figure 5.3: At time t=0, the sample is submitted to a stress of 2 Pa (creep), which is applied during 5 minutes. Then the stress is released (recovery) and measurement is recorded during 2 minutes. This measurement shows that the sample exhibit a quasi rubber-like behavior. The viscosity should be given by the inverse of the slope in the end of the creep phase. Here, the curve is almost flat in the second half of the creep phase, so the measurement that we obtain is not precise $\eta \sim 7\,10^5$ Pa.s.

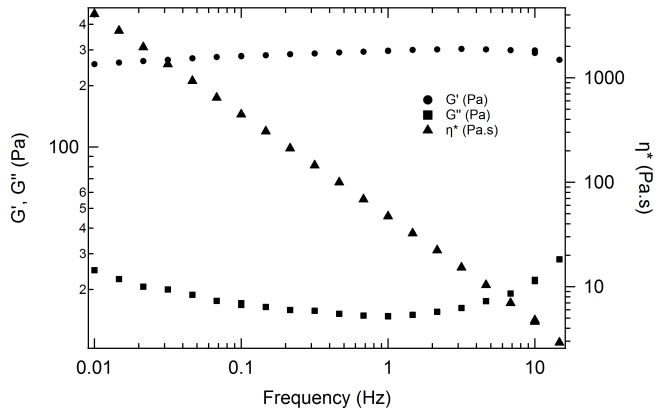

Figure 5.4: Measurements of the elastic modulus G', the loss modulus G" and the complex viscosity η^* by scanning in frequency (oscillatory regime). The linear regime has been determined first by doing scanning in stress at 0.1, 1 and 10 Hz. We finally performed this measurement at a stress of 2 Pa. The measurement lasts 25 minutes. The elastic and loss moduli are parallel and the elastic modulus is larger than the loss modulus, indicating that the elasticity "always" dominates the viscosity.

viscosity, even at very low shear rates: this may due to the strong elastic properties that exhibits the sample, but also to the intrinsic structure of the lamellar mesophase that may influence the measurements depending on the history it has undergone. The viscosity is always dominated by the elasticity. These observations may account for the long-range interactions (linear background) that we measure with the SFA "whatever" is the surface separation, even very large: because of its elasticity, we need to compress the sample a lot before the surfaces get closer.

Thus, SFA experiments are carried out very slowly, to allow the surfaces to reach an equilibrium position in this viscoelastic media before any further step. We have estimated, for each sample, the *maximum* deviation ϵ that we could expect if the separation was measured before the equilibrium. This maximum deviation is obtained assuming that the sample stiffness is vanishing, which is not physically reasonable. IN this way, we obtain an upper boundary of the order of ~ 1 nm in the worst cases, which is weak and in fact never reached.

Moreover, for each sample, the graph representing the l_n (resp. l_n^i) positions plotted as a function of $n-2$ (resp. $\sqrt{n(n-2)}$) shows that the experimental points perfectly align on a straight line, whose slope gives a periodicity very close to the periodicity inferred from SAXS. In particular, the procedure that we followed, consisting in subtracting the linear background and analysing the resulting force versus separation profiles does not affect the l_n and l_n^i positions. We have finally checked two criteria that show that the measurements are performed at the thermodynamic equilibrium. We are thus confident in the analysis of the parabolae, providing the elastic compressibility modulus, which is based on the assumption that the thermodynamic equilibrium is reached.

1.1.2 Outwards runs

We give now a few details about the outwards runs that have not been presented in this work. As mentioned in the experimental Chapters, we have worked only with runs that are performed upon the approach of the surfaces. Indeed, outwards runs exhibit a different behavior: oscillations superimpose on a curve which is not linear (Figure 5.5), and it appears that it is much more difficult to separate the surfaces than to bring them closer. Indeed, the outwards run is located above the inwards run. Nevertheless, the minima of the oscillations seem to be located at the same positions as the inwards runs, as shown in Figure 5.6.

Outwards runs often exhibit the same features whatever is the initial surface separation, whatever is the considered sample: it is difficult to operate the separation between the surfaces at the beginning of the measurement, as shown in Figure 5.8, especially when the starting position is close to the contact position. In this example, the surfaces try to separate and then come back to smaller separations twice before succeeding to initiate the separation. This could be attributed to an energy barrier that the system needs to pass to annihilate the first dislocation, then, once this barrier is reached, the further annihilations seem to occur more easily (once the separation is initiated). The fact that the background curve is not linear makes the treatment more delicate, we do not know how to subtract properly the contribution of the background. We have also observed that some outwards run exhibit larger Burgers vectors, as shown in Figure 5.7, where $b \simeq 5-6$ for example.

The difference between inwards/outwards runs may find its origin in:

- the flow of the lamellar phase between two surfaces that separate is not equivalent

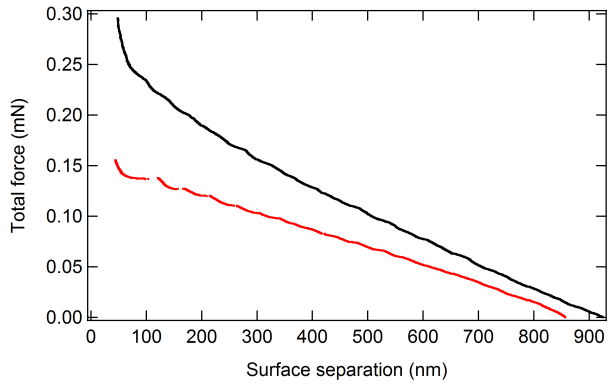

Figure 5.5: Total force as a function of separation for an inwards run (red curve), performed at +5 nm/15 s, and an outwards run (black curve), performed at -3 nm/15 s (sample L). Note that the outwards run is located above the inwards run: it is more difficult to separate the surfaces than to bring them closer. Oscillations superimpose on a non-linear background for the outwards run.

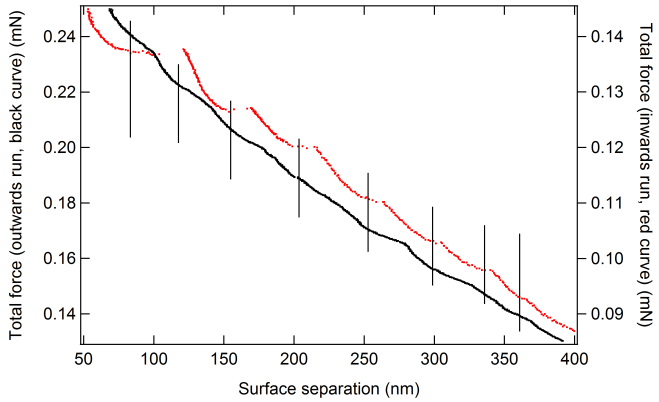

Figure 5.6: The minima of the oscillations of the outwards run seem to be located at the same positions than the minima of the inwards run. The left scale corresponds to the outwards run force measurement (black curve), whereas the right scale corresponds to the inwards run measurement (red curve). One oscillation is "missing" in the inwards run (the second starting from the left), the system expelled exceptionnally 4 layers at the same time.

to the flow of the lamellar phase when the two confining surfaces get closer;

- when the surfaces separate, the dislocation loops must annihilate, which is not equivalent to the creation of a dislocation loop. Regarding the measurements, it appears that it is more difficult to annihilate the dislocation loops than to creates them;

- finally, when the surfaces separate, the system may remain "longer" at constant

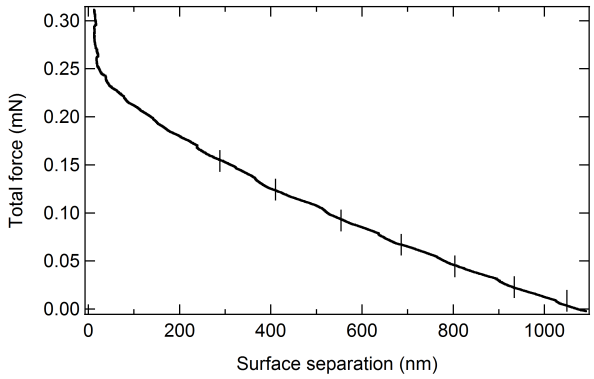

Figure 5.7: Force versus separation for an outwards run performed at -3 nm/15 s (sample L). The minima are separated by approximately 5 to 6 periodicities ($b = 5 - 6$).

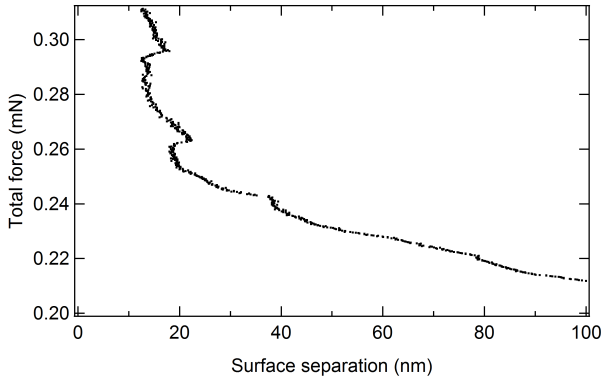

Figure 5.8: Enlargement of the force curve presented in Figure 5.7. At the beginning of the run, it is difficult for the system to operate the separation between the surfaces: the surfaces start to separate and finally come back to smaller separations twice before succeeding to initiate the separation.

number of layers: the membranes have thus more space to undulate.

Much effort needs to be done to understand these outwards runs, this is why we have focused until now on the inwards runs.

1.2 Comparison with other techniques

Ficheux *et al.* performed neutron scattering on samples that are lamellar mesophases of the same system [35]. They mapped the Caillé exponent $\eta \propto 1/\sqrt{K\bar{B}}$ in the dilute part of the lamellar region and onwards to the biphasic region, especially in the vicinity of the critical point Pc2. This exponent appears to increase when the polymer concentration in water increases, as well as when the critical point Pc2 is approached. The authors associate the increase of the Caillé exponent to a possible decrease of the elastic compressibility modulus. It has indeed been observed in a similar system [40]

(SDS/pentanol/water/PEG), with the SFA technique, that the elastic compressibility modulus decreases when the polymer concentration increases (the polymer induces a softening of the intermembranes interactions). Moreover, $\bar{B}$ is expected to vanish at the approach of the critical point. Our results go in the same direction since we observe a decrease of the elastic compressibility modulus when the concentration of the polymer increases. Towards Pc2, we will see in the following Section that our results are also consistent with a measurement performed by Ficheux *et al.* [34] by means of the Dynamic Light Scattering technique (DLS).

We have also performed DLS experiments in collaboration with Eric Freyssingeas in the laboratoire de Physique de l'ENS Lyon. The DLS technique is indeed a powerful technique that provides information on both $\bar{B}$ and K [75, 39]. Unfortunately we were not able to get satisfactory results, mainly because this technique requires the preparation of very well oriented samples (in rectangular capillaries of thickness $\sim 100 - 200$ μm) which proved to be extremely difficult to obtain, as already observed by Ficheux *et al.* [34, 33]: they have not been able to get results for more than one sample.

So several techniques have been attempted to improve the homeotropic alignment (membranes parallel to the capillary walls). First we tried with a thermal annealing treatment, that consists in heating progressively the sample until the lamellar to isotropic phase transition is reached, then the sample is cooled down very slowly by steps. This is done under the optical microscope thanks to a Mettler Toledo FP82HT hot stage. This usually yields oriented samples, with an anchoring of the membranes parallel to the walls. For the system considered, this technique was not efficient: most of the samples are still biphasic at temperatures above 65°C and when cooled down, defects reappear in the sample. Some surface treatments have also been tried (the capillaries VitroCom were first cleaned with a water plasma): hydrophilic surface treatment with nitric acid, and hydrophobic surface treatment with dichlorodimethylsilane (DCDMS). These treatments do not improve significantly the orientation. Finally, we have tried with thinner capillaries and spacers between two glass plates that allow to get 10 μm of sample thickness (which would be in fact too thin for the DLS experiments), but again no improvement was observed.

These serious problems in obtaining good quality oriented samples may arise partly from spherulites that are present in the sample, and that form certainly during the equilibration of the sample (the formation of spherulites is favoured by shearing [28, 29]). The spherulites were already observed by Auguste in the system SDS/ octanol/ water [6].

We discuss now theoretical aspects concerning the elastic compressibility modulus.

2 Elastic compressibility modulus: theory versus experimental results

In all the total force versus separation profiles measured, we observe a linear background on which oscillations superimpose. To our knowledge, such a linear background has never been observed before. By subtracting the linear background, the force-separation profiles obtained exhibit similar feature to those of the literature and we finally analyze them within the model developed by Richetti *et al.* [83] and recalled in section 2. Before going into this analysis, we discuss about the linear background.

2.1 The linear background

We have seen that the speed at which the experiment is carried out has an effect on the slope of the linear background (see Chapter 3, section 2): when the speed increases, the slope increases. This has been attributed to the rheology of the lamellar mesophases: when the speed is too high, the surfaces do not have the time to reach their equilibrium position in the viscoelastic media and thus the separation between the surfaces is overestimated, which leads to an overestimated total force. But we have seen that most of the measurements that are performed at thermodynamic equilibrium (see previous Section 1) still exhibit this linear background, which may thus not result from the viscosity of the media but rather from its elasticity (macroscopic approach). We interpret the existence of the linear background in the following from a "microscopic" point of view.

We have observed that the initial surface separation has an influence on the linear background: when l_0 increases, the slope decreases. One possible explanation of this phenomena is that the dislocations array contributes to this background, and it does not contribute "in the same manner" depending on the separation at which the measurement is started. We explain now in details what we mean.

Let us first consider one isolated total force profile. Being strictly linear, the background has been interpreted in terms of stiffness of the sample. Thus, what is remarkable, is that the stiffness is constant during the measurement. But some dislocations are nucleated in the course of the measurement, so some layers are ejected. So if we think about a model of membranes equivalent to a series of springs, the stiffness of the sample should increase when layers are ejected and this is not what we observe. What then comes into mind, is that one ejecting layer (or two or more depending on the Burgers vector of the dislocation) still contribute to the stiffness of the sample, and rigorously with the same weight as when it was in the stack, before the nucleation. In other words, the growing of the dislocation loop has a cost (its line energies must increase when the surfaces are getting closer) and finally this contribute to the stiffness of the sample.

Why do we have different slopes when the initial starting separation is different? One explanation that we propose is that the dislocation array to be moved is not the same, or more precisely, *seems* to be different. Indeed, at any initial surface separation

l_0, there is already a dislocation array that exists and a force is already experienced by the surfaces. But as explained in Chapters 2 and 3, with the SFA we do not have any access to the absolute force. The initial force experienced by the surfaces is arbitrarily set to zero ($F_0 = 0$). So we measure the relative force to the initial point. Again, if we think about a model of membranes equivalent to a series of springs, (or more accurately, in the light of the previous paragraph, a stack of membranes *and dislocations* equivalent to a series of spring) the stiffness of the sample is given by $K_s = k_m d/l_0$, where k_m is the equivalent membrane or dislocation stiffness, d the period of the mesophase. The slope is thus proportional to $1/l_0$ as observed in Chapter 3 section 2, except that we observe an asymtote different from zero.

The relation between K_s and l_0 may be more complex in reality. We finally want to highlight that there is a dependence between the slope and the initial number of layers, because of an effect of the dislocation array.

2.2 The electrostatic interaction

Once the linear background is subtracted, we obtain a force-separation profile similar to those of the literature (Chapter 3, Section 2, sample L). In particular, the line energies appear to be negligible: the l_n^i positions plotted against $\sqrt{n(n-2)}$, since $b = 2$, perfectly align.

The oscillations superimpose on an attractive background, also observed in others systems [61, 84] and whose origin has not been clearly identified yet. In [83], the authors propose two possible origins. The first possibility would be a Casimir-like effect where some orientational fluctuations of the structured phase are suppressed by confinement. The second possibility, closely related to the first idea, considers fluctuations over smaller scales: the attraction would be the consequence of the interaction between the walls and the structured sample (local enhancement of the smectic order parameter in the vicinity of the walls). Please refer to [83] for more details.

The elastic compressibility modulus extracted reads $\bar{B} = (16.6 \pm 2.8)$ kPa. As checked in Chapter 4, Section 2, the Burgers vector does not modify the elastic force equation (equation 4.44) and thus has no influence on $\bar{B}$.

This value has been interpreted within the Poisson-Boltzmann theory ($\bar{B} \simeq 25$ kPa), and taking into account i) a correction accounting for a more precise numerical solution to the Poisson-Boltzmann equation [80] ($\sim -6\%$) ; ii) the counterions correlations, calculated by deriving the pressure given in [72] ($\sim -22\%$). To our knowledge, this is the first time that the counterions correlations are taken into account in the study of lamellar mesophases. Finally the correction to apply is of about $\sim -30\%$, which leads to a good agreement between experiment and theory. To have a complete overview of the situation, we should check that the ionization rate is closer to 1 and we should calculate the effect of the organization of the ions in the membranes, and the coupling between the counterions and the ions organizations. This coupling may also influence the ionization rate [37].

2.3 The effect of the polymer concentration

As seen in Chapter 3 (Section 2, sample M) the force profile obtained once the linear background is subtracted does not exhibit clearly an attractive background. For this sample, the nucleation of the dislocations seems sometimes to influence the position in force of the parabolae (see Chapter 3, Section 2).

For this sample, we measure $\bar{B} = (6.4 \pm 1.7)$ kPa. Since the polymer does not modify the dielectric constant of water for the concentration considered, we try to interpret this value by adding up the contributions of the electrostatic interaction and of the polymer (ignoring the polarisation effect). Since samples L and M contain the same amount of membranes, the electrostatic contribution for both samples should be the same $\bar{B}_{elec} \simeq 17$ kPa and thus we expect $\bar{B}_{pol} \simeq -10$ kPa.

We attempt to interpret this value within the framework developed by Ligoure *et al.*, considering the 3-Dimensions - Semi-Dilute regime. Note that this model holds for a non-adsorbing polymer, but surprisingly seems to reproduce well the experiment since we obtain $\bar{B}_{pol} \simeq -9$ kPa. Since there is no physical reason to keep this model, we try to adapt this theory to a situation where the polymer adsorbs on the membranes. But this approach leads to a contradiction (see Chapter 4), showing that the semi-dilute regime is not adapted to describe the situation. This leads us to consider a mean-field approach, constructed by Semenov et al. [87], which takes into account the effect of the polymer chain-ends. In particular, this theory behaves well for concentrated solutions. But this does not give any satisfactory result: first, the region where the curvature of the potential is negative is very restricted in terms of interlayer spacing (we are not sure to be in this region); secondly, the order of magnitude of $\bar{B}_{pol}$ that we obtain is well below what we expect (factor $\sim$30). So this theory may account for a weak polymeric effect, whereas we measure a stronger polymeric effect. Note that some SFA experiment performed with supported membranes of SDS on the mica surfaces, immerged in a PEG ($M_w = 20000$ g/mol) solution of similar concentration, show that there is an attractive minimum at separations $\sim 4R_G$ [59]. But the amplitude of the minimum is too large by one order of magnitude to be interpreted with this theory.

We thus have to make efforts in the future to interpret this result. One possible way would be to examine the effect of the coupling between the polymer and electrostatics, since it may play a non-negligible role. Note that this effect cannot be taken into account in an additive manner and that it requires a more difficult approach than what has been attempted yet. We may also expect a coupling between the polarisation and the ionization rate.

2.4 Towards the critical point P_{s2}: avalanche phenomena

Once the linear background is subtracted, the force versus separation profiles obtained for both samples are very different from those of samples L and M and more generally from those of literature. This force profiles show that large strains exceeding several layers thicknesses must be applied before the nucleation of a dislocation occurs. For

these samples, the line energies obviously play a crucial role and thus must be taken into account.

As explained in Chapter 3 (Section 3), the elastic compression moduli are extracted by fitting the lower part of the experimental curves with a parabolae. For sample N, the value extracted reads $\bar{B}_N = (18.8 \pm 2.5)$ kPa and for sample O, it is $\bar{B}_O = (23.4 \pm 3.6)$ kPa.

First of all, these values appear very close to each other, and quite small compared to what is expected for this range of intermembrane spacing, especially for sample O (see below). This is why one may think about the effect of the critical point P_{s2}: since we expect $\bar{B}$ to vanish at P_{s2}, the elastic compressibility modulus could already diminish for these mesophases that are located not so far from P_{s2}.

In particular, we can discuss these results regarding the value of the elastic compressibility modulus measured by Ficheux et al. in [34]. They perform dynamic light scattering experiment on an oriented lamellar mesophase which contains $C_p = 5$ % and $\Phi_{memb} = 24$ %, located close to the critical point P_{s2} ($C_p = 3.8$ % and $\Phi_{memb} = 32$ %). The layer compression modulus measured is found to be $\bar{B} = 1.9$ kPa, which is also well below the expected value given by the electrostatic interaction. Regarding this value, our results do not seem incompatible, and the critical point may account for these low values measured.

For both samples, the polymer concentration is of the order of the overlap concentration, thus it is impossible to ascribe them a regime (3D-D, 3D-SD, 2D-D or 2D-SD): they are located in the crossovers. Let us compare naively these values with the pure electrostatic contribution expected, estimated with Poisson-Boltzmann and corrected like for sample L. For sample N, we get $\bar{B}^N_{elec} \simeq 70(1 - 0.4) = 40$ kPa; and for sample O we get $\bar{B}^O_{elec} \simeq 150(1 - 0.5) = 75$ kPa. We first note that the corrections become considerable, because of the counterions contribution mainly. The value of the parameter Ξ is reasonable ($\Xi \simeq 3.14$, same value as in Chapter 4, section 1, sample L), so we are still in the intermediate coupling regime and these corrections should remain valid (note that the effect of the organization of the ions in the membranes should also be taken in consideration).

Nevertheless, if we assume that this is correct, we thus find a polymer contribution of about $\bar{B}^N_{pol} \simeq -20$ kPa for sample N and $\bar{B}^O_{pol} \simeq -50$ kPa for sample O. This might be interpreted with the model that takes into account the effect of chain-ends [88, 87] applied in the semi-dilute regime. This effect might be more significant in the dilute regime than in the concentrated one: the more the solution is concentrated, the less it is "depleted" (see Chapter 4) and the less the resulting interaction is attractive. Of course this is a very simple explanation of what could be expected.

The polarisation effect should also be taken in consideration. We also expect that it is stronger than for sample M: since the adsorption concentration profile is more pronounced for a less concentrated solution, it is also more sensitive to any perturbation of the electric field. Thus the water molecules (and consequently the polymer molecules) are redistributed between the membranes and the resulting intermembrane interaction

is modified. Note that the polarisation effect is also coupled to the ionization rate, and that this subtle effect certainly requires a microscopic approach to be estimated.

Eventually, to better understand these results, we should estimate these contributions but also perform others SFA experiments, on the same dilution line, closer to Pc2 to confirm the decrease in $\bar{B}$.

2.5 General considerations on the effect of the polymer on the membranes

We observe directly that the polymer has an effect on the structure of the lamellar mesophases: the membrane thickness and the periodicity of the stack decrease when the amount of polymer in water increases. If we consider samples L and M, this effect is quite spectacular: the period decreases from $d = 22.8$ nm ($C_p = 0$) to $d = 18.5$ nm ($C_p = 15$ %), whereas the membrane thickness decreases from $\delta = 24$ Å to $\delta = 21$ Å (see also [34]). Concerning the membrane thickness, we may interpret this effect because of the adsorption of the polymer: when some polymer brands penetrate the membrane, the surface area per charged polar head Σ increases as seen in Chapter 4 (increase of 20 % of Σ when C_p increases from 0 to 15 %). This may result in a kind of stretching of the membranes: the volume of the tails is distributed a little bit differently; they have more space in the lateral directions, thanks to the polymer brands that does not penetrate completely the membranes, which results in thinner membranes.

The adsorption of the polymer on the membranes, which may account for these observations, has been investigated with the Fluorescence Recovery after Photobleaching technique (FRAP, see Figure 5.9). Some preliminary results of experiments, performed in the Institute in collaboration with Thierry Charitat, indeed show that there is a significant immobile polymer fraction. In Figure 5.10 we present a fluorescence decay performed on a lamellar mesophase close to the critical point P_{s2}. The data are fitted with a double-exponential function, but we see that the signal does not decrease down to zero, i.e. the fluorescence do not recover in the bleached volumes of the samples, that is to say there is a significant immobile fraction of polymer. This fraction is estimated with the ratio of the stable signal in the end of the decay to the maximum signal, we find up to 80 % of immobile polymer. This confirms the adsorption of the polymer on the membranes.

In Figure 5.11, we present a graph of the decay time as a function of the inverse squared wave vector, for a PEG solution with $C_p = 1$ wt % and for several lamellar mesophases. Concerning the polymer solution, the points align on a straight line whose inverse curve gives a diffusion coefficient $D = (4.2 \pm 0.1)\,10^{-11}\mathrm{m}^2/\mathrm{s}$ as expected ($D = \frac{k_B T}{6\pi\eta R_H} \simeq 3\,10^{-11}\mathrm{m}^2/\mathrm{s}$). Concerning lamellar mesophases, this graph exhibits several diffusing polymer populations: one population would diffuse as quickly as the free polymer; two others populations would diffuse more slowly: the diffusion coefficients are smaller from resp. one and two orders of magnitude. One may interpret these intermediate diffusing populations as exchanging populations between the free polymer

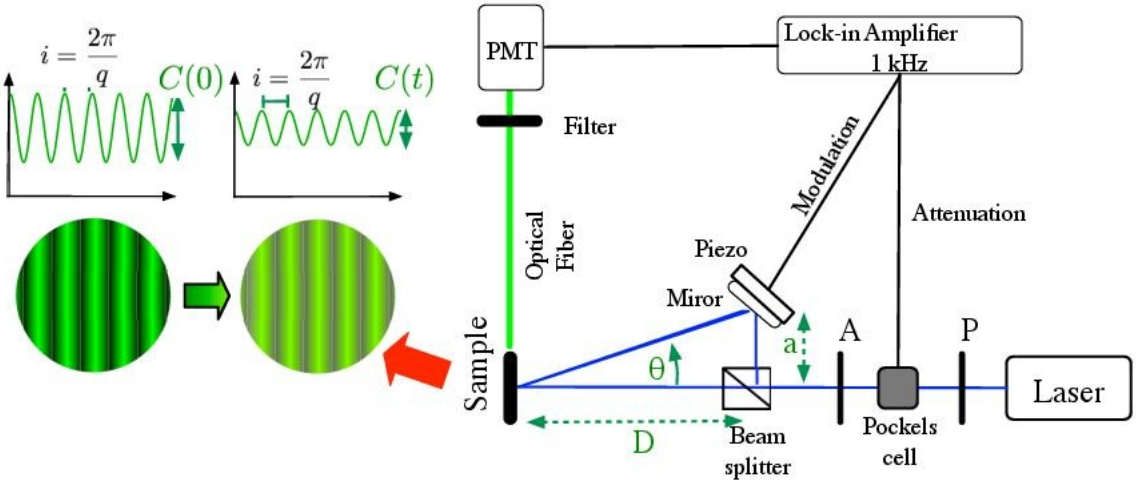

Figure 5.9: Scheme of principle of the FRAP experimental setup. The laser is an Argon laser whose wave length is $\lambda = 488$ nm. "P" and "A" denotes respectively a polarizer and an analyzer that are almost crossed. The polarisation of the beam turns thanks to the Pockels cell so as to bleach the sample. The beam splitter and the mirror allow to light the sample with an interference fringe pattern. At t=0, the sample is bleached with a fringe pattern of high intensity. The fluorescence signal emitted by the sample is then "read" thanks to a fringe pattern of lower intensity that vibrates (thanks to the piezoelectric device). The lock-in amplifier allows to detect the fluorescence signal of the sample that vibrates at the frequency of the piezo: we thus have an access to the contrast between the zones initially bleached and not. This contrast decreases with time. To perform these experiments, the sample have been prepared with 1 molecule of fluorescent PEG for 100 of polymer molecules. The fluorescent PEG is a mPEG Fluorescein (methyl-PEG-FITC) of brand Uptima and of molecular weight 20000. The absorption peak of the fluorescein is at 494 nm.

population (not adsorbed, in the middle of the interlayer spacing) and the adsorbed polymer population (immobile fraction).

We need to repeat these experiments to confirm confidently these trends. Nevertheless, these preliminary results give insights into the complexity of the polymer dynamics between the membranes.

One can wonder which is the effect of the polymer on the lamellar structure upon the approach of the critical point. Since it induces a destabilization of the smectic order, one may expect that the lamellar structure progressively undergoes structural modifications. Thus, one may expect also that the polymer diffusion exhibits specific features, compared to lamellar mesophases located in the dilute part of the phase diagram.

With the SFA technique, the experiments are performed in principle at constant chemical potential [58], in particular the chemical potential of the polymer should re-

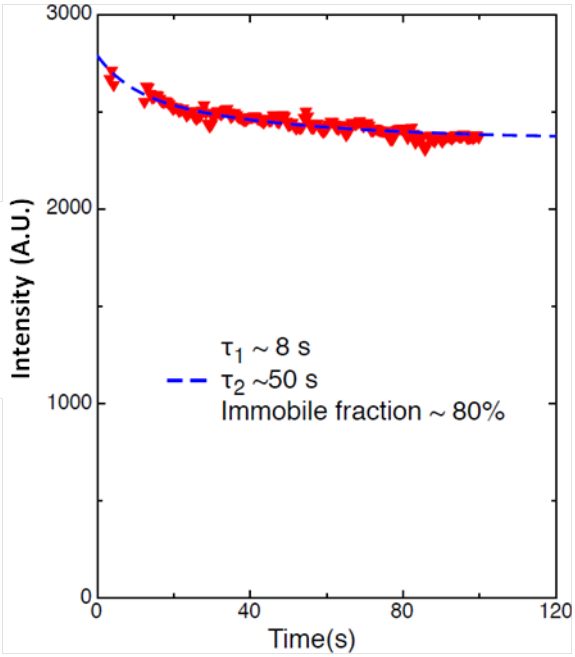

Figure 5.10: Fluorescence decay performed on a sample close to the critical point P_{s2}: $C_p = 3.8$ % and $\Phi_{memb} = 29$ %. The dashed blue line indicates a double-exponential fit giving the decay times $\tau_1 = 8$ s and $\tau_2 = 50$ s, note that the curve reaches an almost constant value showing that there is a significant immobile polymer fraction.

main constant during a force run measurement. Since the polymer adsorbs on the membranes, one may expect that the polymer is not completely expelled, and that its concentration is larger than what it should be during the course of a measurement. Since the measurement of the refractive index suffers from a lack of resolution, we do not have access to the polymer concentration between the bilayers, for the last confined bilayers.

In the Chapter 4, we have calculated the elastic compressibility modulus at constant surface fraction of polymer (Ligoure et al. framework), this does not give the expected sign to the polymer contribution to the elastic modulus. The calculation at constant chemical potential gives on contrary the expected sign. But this does not prove that the chemical potential of the polymer effectively remains constant...

2.6 Measurements at large separations

To our knowledge, this is the first time that SFA measurements are performed at such large surface separations, between 6 and 10 μm. Surprisingly, the behavior of the sample N at these separations is closer to the behavior of samples L and M than to the same sample at shorter separations (avalanches). Indeed, regular oscillations superimpose on a linear background, the slope of the linear background is of the same order of magnitude $C \sim 0.2$ (same for sample L). Once the linear background is subtracted,

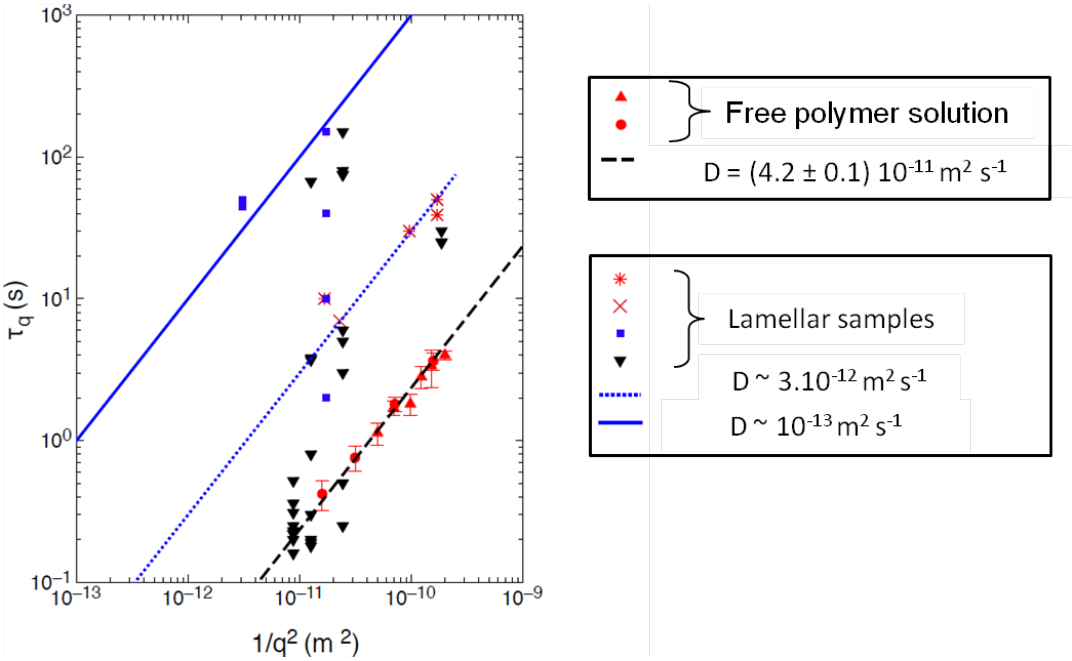

Figure 5.11: Decay time as a function of the inverse of the squared wave vector, for a PEG solution with $C_p = 1$ wt % (red full triangles and circles), and lamellar mesophases of different compositions (other symbols). For the polymer solution, the points align on a straight line whose inverse curve gives a diffusion coefficient $D = (4.2 \pm 0.1)\, 10^{-11} \mathrm{m}^2/\mathrm{s}$ as expected. For the lamellar mesophases, the experimental points seem to belong to several straight lines, meaning that there would be several diffusing populations (here, maybe three diffusing populations). One population would diffuse as quickly as the free polymer, and two others populations would diffuse more slowly: the diffusion coefficients are smaller from resp. one and two orders of magnitude.

the force profile exhibit surprisingly large oscillations of constant amplitudes, about 2 mN/m. The Burgers vector appears also large and constant, $b = 26$ in average. Compared to sample L, the separation between the surfaces is multiplied by a factor 10, the amplitude of the oscillations is multiplied by about a factor 20, and the Burgers vector is multiplied by a factor 13.

For this range of separations, the crossed cylinders geometry is still equivalent to a sphere against a plate. Moreover, the Burgers vector appears constant, and the l_n and l_n^i positions plotted as a function of n and $\sqrt{n(n-26)}$ respectively perfectly align on a straight line whose slope gives the reticular distance expected from SAXS measurement. This is why the results have been analyzed within the framework of Chapter 4, Section 2.2, where the line energies of the dislocations are neglected. The value of the elastic compression modulus measured is $\bar{B} = (1.8 \pm 0.4)\, 10^5$ Pa, which is one order of magnitude higher than the value measured at shorter separations, where we observe the avalanches phenomena ($\bar{B}_N = (18.8 \pm 2.5)$ kPa). This value is also

superior to the pure electrostatic contribution $\bar{B}_{elec} = 70$ kPa calculated without any correction.

We may thus wonder about a possible influence of the dislocations of large Burgers vectors on the elastic properties of the mesophase. The influence of dislocation loops on the elastic constants of lyotropic lamellar phases has been investigated by Freyssingeas *et al.* in [41]. They studied a lamellar phase made up of a mixture of $C_{12}E_5$ (non-ionic surfactant) and lecithin (DMPC) in water by means of Quasi-Elastic Light Scattering on oriented lamellar phases. By decreasing the temperature, they approached the lamellar to nematic phase transition that occurs at 19°C. Dislocations proliferate when the temperature is decreased below 30°C. They observed a strong and rapid increase in $\bar{B}$ and K as the transition is approached, and these increases are seen to start as soon as dislocations loops can be observed in the lamellar phase. Freyssingeas et al. finally showed that these elastic constants are proportional to the density of dislocations loops in the lamellar phase.

Of course, our problem here is not similar to the study of Freyssingeas *et al.*, where the proliferation of dislocations is due to pretransitional effects. In our case, even if the line energies appear to be negligible, they may play a significant role in the phenomena, favouring the "gathering" of bilayers in large edge dislocations, which then directly influence the elasticity of the stack. What we measure is thus an effective $\bar{B}$ which includes a contribution of the dislocations. In the next section, we discuss the nature of the dislocations of large Burgers vectors.

3 Dislocations

3.1 Large Burgers vectors

According to Kléman [64], edge dislocations are favourable to large Burgers vectors, whereas screw dislocations favoured small ones. A screw dislocation does not have any line energy and its core energy is proportional to b^4, this is why only screw dislocations of small b are stable. The energy per unit length of an edge dislocation is

$$W = \gamma + \gamma' = \frac{\bar{B}\lambda b d}{2} + \frac{\pi}{2} K \ln\left(\frac{b}{2}\right) + e_\mu$$

where e_μ is weakly dependent in b, and finally the last two terms are responsible for the stability of edge dislocations of large Burgers vectors.

Edge dislocations of large Burgers vectors have been observed in a geometry similar to the one of the SFA by Nallet and Prost in [74]. In this article, the authors show that there is a direct relationship between the thickness of the sample and the Burgers vector. Minimizing with respect to b the energy per unit length of the array of dislocations, they show that as long as the radius of the dislocation r is smaller than r^* a critical radius, the Burgers vector is a constant, equal to the minimum value allowed $b = b_{min}$.

For r larger than r^*, b becomes a function of r:

$$b = \frac{r}{d}\Big(3\pi\frac{\lambda^2}{R^2}\Big)^{1/3} L\big(\frac{r}{r_0}\big)$$

where λ is the penetration length of the smectic. Please refer to [74] for details about r_0 and $L(\frac{r}{r_0})$. The experimental data, obtained by measuring the distance between adjacent edge dislocations by means of optical microscopy (between crossed polarizers), are then fitted according to the model developed and allow them to infer the penetration length λ and other microscopic quantities. In the experimental conditions considered, the wedge-shaped cell allows them to investigate thicknesses ranging from about 20 μm to 100 μm, which corresponds to an increase of the Burgers vector from about ten to thirty for the system considered.

When SFA experiments are performed for a separation below 1 μm, we observe mainly dislocations of small Burgers vectors, often $b = 2$, but Burgers vectors up to $b = 4$ or 6 have been occasionally observed. For separations up to 15 μm, the Burgers vectors is of the order of $b \simeq 30$ (sometimes even more for outwards runs). We have also investigated intermediate separations and we present *preliminary results* in Figure 5.12. In this Figure, we present the evolution of the Burgers vector b with the surface separation at which the nucleation of the dislocation occurs. It seems clear that there is a link between the surface separation and b. Above 3 μm, the Burgers vector seems constant, $b \simeq 30$. Below 3 μm, the Burgers vector decreases with the surface separation, and below 1 μm the Burgers vector seems to reach its constant value $b_{min} \simeq 2$ observed in particular in the force profiles of samples L and M.

We think that this phenomenon of large Burgers vectors at large separations is due to a collective effect of the large number of layers confined in the gap. Note that a similar behavior has been noticed for sample O, but unfortunately very little data have been recorded (the mica surfaces broke when we started to perform such measurements).

3.2 Small Burgers vectors

In Chapter 3 Section 2, we have plotted the l_n^i positions against $\sqrt{n(n-2)}$ where n is an even integer $n = 2, 4, 6...$ Indeed, for a set of parabolae whose minima are separated by two times the period ($b = 2$), two consecutive parabolae intersect at the position $l_n^i = \sqrt{n(n-2)}d$. This result can be generalized to any Burgers vector b: $l_n^i = \sqrt{n(n-b)}d$.

For both samples L and M, a Burgers vector $b = 2$ is obviously more favourable for the system. For similar systems, Richetti et al. [84] and Freyssingeas et al. [40] observe $b = 1$ dislocation loops. Dislocation loops of Burgers vector equal to 2 have been observed in the system AOT in brine ($AOT/NaNO_3/H_2O$) stabilized by undulation forces, studied by Antelmi et al. in [3]. The authors performed SFA experiments on samples close to the sponge/lamellar transition: such a defect, topologically equivalent to a

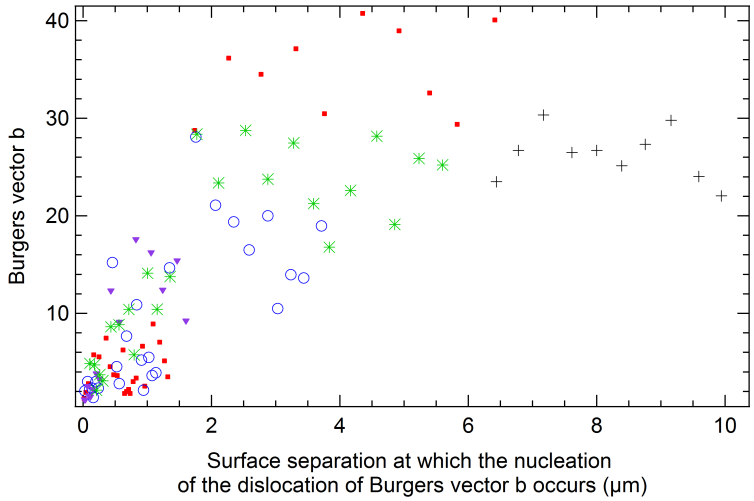

Figure 5.12: Burgers vector b as a function of the surface separation at which the dislocation nucleation occurs (*preliminary results*). The five types of symbols account for five different measurements, performed at similar speeds but at different initial surface separations.

handle joining two membranes, arises naturally from the topology of the neighbouring sponge phase.

Diffuse scattering on oriented samples would give insights into the topology of the membranes, and maybe would show the presence of defects in the lamellar phase (holes, connections between the membranes...) that may favour this configuration $b = 2$. But it may also arise from the electrical charges, that may rearrange better in membranes experiencing a $b = 2$ dislocation loop, which are thus less curved than a membrane experiencing a $b = 1$ dislocation loop. Finally, the alcohol may also play a role.

As already mentioned earlier in this Discussion, the outwards runs seem more favourable to larger Burgers vectors (see Figure 5.7) than the inwards runs. Concerning sample L, we observe in average $b = 2$, but some outwards runs exhibit $b = 3$ or even $b = 5 - 6$. Note that this observation has been also reported for measurements at large separations. It may be energetically more favourable for the system to remain a longer time at constant number of layers (to allow undulations of the membranes) upon the separation of the surfaces and then to brutally include more bilayers.

3.3 Avalanches and nucleation energies

The force versus separation profiles (once the linear background is subtracted) start with a long compressive step (more than a few layers), which appears to be longer when the initial surface separation is larger, and which leads to a larger critical force before the system is able to nucleate a "first" dislocation loop. For these samples N

and O, in this range of separations (below 500 nm), the line energies appear to play a crucial role.

Before nucleating a first dislocation loop, the system needs to pass a huge energy barrier, of the order of $10^7\ k_BT$ to $10^8\ k_BT$ (Chapter 3, section 3). Let us attempt to interpret this order of magnitude in the light of the model developed by Richetti *et al.* and presented in Section 2.3. The energy barrier reads:

$$\Delta E_0(r_c) \simeq \frac{2\sqrt{3}-3}{3}\frac{\pi R\bar{B}bd}{e_0}\epsilon^2 \tag{5.1}$$

where

$$\epsilon = e_0 - e_c \simeq \frac{3}{2}\left(\frac{\tilde{\lambda}^2 e_0^2}{2Rb^2}\right)^{1/3}. \tag{5.2}$$

We can estimate ϵ from the force curve, assuming $b = 2$. Let us take the force run measurement 2 performed on sample O (Chapter 3, Section 3). We have: $l_n = 288$ nm, $e_0 = 288 - 11 = 277$ nm and $e_c = 169$ nm. We deduce $\epsilon = 107$ nm. Attempting to deduce $\tilde{\lambda}$ from equation 5.2, we obtain a value which is huge: $\tilde{\lambda} = 28\ \mu$m! This is 3 orders of magnitude higher than the expected value, usually ranging from 10 to 100 nm for such systems. However, taking the value measured for ϵ, we deduce from equation 5.1, with $\bar{B} = 23.4$ kPa, $\Delta E_0(r_c) =\simeq 5\,10^7\ k_BT$, which is in fact in good agreement with experiment (Chapter 3, Section 3).

So the way the quantity ϵ is derived may not be adapted to our situation. Some approximations may be questionable, in particular the approximation $e \simeq e_0$, since $e_0 - e$ can go up to $\epsilon = e_0 - e_c = 107$ nm, which is of the order of 10 periodicities of the sample. The sample is compressed over a distance equivalent to approximately 12 periodicities, which leads us to wonder if the assumption of the independent cells is still valid. So in this model, the way the energy of the dislocations is taken into account certainly underestimates the role that the dislocations play. They may count for far more to what we expect, unless another unknown phenomena adds up (for instance topological defects connecting the membranes such as handles).

In Chapter 3 Section 3, we have plotted the total energy of nucleation E, integrated along the force curve with respect to the calculated set of parabolae, as a function of the square of the rank n^2. The law appears quadratic with a similar coefficient for both samples: $\alpha = \frac{E}{n^2} \simeq 10^6\ k_BT$. We do not know how to interpret this result, since the Burgers vectors of the dislocations cannot be identified with absolute confidences for each measurement. Indeed, let us consider the force profiles of sample O. In the course of the measurement 1, only one jump occurs. We do not know whether it accounts for a unique dislocation loop of Burgers vector $b = 32$, or several dislocations of smaller Burgers vectors which succeed to each other very quickly. We may also wonder about the nature of the dislocations: is it edge dislocations? Or screw dislocations? Herke *et al.* have reported [49, 50] that the elastic stress of a thermotropic liquid crystal confined in a thick spherical wedge (a few microns) and under strain could be released by an avalanche of helical instabilities of screw dislocations lines.

In [77], Oswald and Pieranski calculated the critical radius of an elementary dislocation loop as well as the activation barrier associated to this critical radius in free smectic films. They also present experimental results concerning the measurement of the critical radius of nucleation in free smectic films of 8CB (thermotropic smectic) [43]. They are able to deduce the activation barrier that the system needs to pass to nucleate an elementary dislocation loop. In the limit of thick films (where the attractive interactions between the free surfaces are negligible, the number of layers is superior to 30), $\Delta E \simeq 6\,10^5\ k_BT$. Our inferred value $\alpha = \frac{E}{n^2} \simeq 10^6\ k_BT$ is of the same order of magnitude.

These avalanches phenomena may find their origin in the confinement of the macromolecules. Indeed, for sample N, the size of the polymer coils is comparable to the gap between the membranes; for sample O, the coils are a little bit compressed. The layer of confined polymer between the membranes may thus induce a stiffening of the stack, by bridging two neighbouring membranes for example.

Conclusion and perspectives

In the course of this thesis, direct measurements of the elastic compressibility modulus have been performed on lamellar mesophases of the system SDS/octanol/water/PEG. Different compositions of this mixture have been prepared to allow an exploration of the phase diagram in its dilute part (in membrane). Thus by comparing three samples containing polymer to one sample without, insights into the effect of the macromolecules on the stability of the lamellar mesophase have been inferred. But this study has also been the opportunity to perform for the first time measurements at very large separations ($\simeq 15\mu$m), thanks to a very stable Surface Force Apparatus developped in the Institute and a home-made software that allows a very precise separation measurement (based on a simultaneous fringes detection). These measurements at large separations reveal nice regular oscillations of large amplitudes and dislocations of large Burgers vectors. Other measurements performed at shorter separations exhibit also unexpected phenomena: an avalanche process is revealed when the lamellar composition approaches the critical point Pc2 of the phase diagram. The system has to overcome a large energy barrier before it is able to nucleate a first dislocation loop, once this barrier is reached, the following dislocations occur in very quick events that succeed to each other. This new phenomena that we report unambigously open the way to very interesting physics.

From a theoretical point of view, it has been possible to find a quantitative agreement with the experimental results concerning the electrostatics of the system. When no macromolecules are added, the undulating membranes are stabilized by electrostatic interactions, and the counterions appear to play a significant role: their correlations allow to weaken the electrostatic interaction and the theoretical prediction finally meets nicely the experimental data. Concerning the samples containing polymer, we have not been able to satisfactorily interpret the measurements with a theoretical model. Additional theoretical investigations have to be done. Nevertheless, regarding the literature [34, 35], the experimental results seem reasonable: the polymer induces a priori a softening of the intermembranes interactions, as already observed on similar systems [40]. Concerning the avalanches phenomena, we have been able to extract the energy barrier that the system needs to pass to nucleate a dislocation. We have tried to interpret these results within the Richetti *et al.* framework [83], but the way the line energies of the dislocations are taken into account must be improved to get adapted to this system. Indeed the independance of the edge dislocations in that model seems questionable.

The approach of the critical point Pc2 is not complete. Indeed, this approach

turned out to be difficult experimentally, mainly for two reasons. First, the lamellar mesophases are viscoelastic media, which requires very slow records of the measurements to make sure that the equilibrium is reached at every step. We could have used a stiffer cantilever, but we would have lost in sensitivity, which is not desirable. Second, the mesophases exhibit a significant turbidity, which makes the optical measurement of the separation delicate. Nevertheless, the study of two samples on the dilution line leading the critical point Pc2 exhibit the unexpected avalanches phenomena, which may be a sign of crucial modifications of the interactions and/or the structure (defects connecting the membranes) in the mesophase, expected on the approach of a critical point.

These avalanches phenomena, as well as the measurements performed at large separations which allow to infer an enhanced value of the elastic compressibility modulus indicate that there exists a subtle interplay between dislocations and elastic properties of the system. It has already been observed that dislocations can affect the elastic properties [41] of a lamellar mesophase. But the elasticity of the mesophase may also strongly influence the conditions favourable to the nucleation or annihilation of a dislocation. The distinction between the elastic and plastic regime for lamellar mesophases of this system appears to be intricate. The ways of study opened thanks to the SFA technique bring us to consider other techniques, that may give some hints to enlighten these questions.

First, the Dynamic Light Scattering (DLS) technique is a powerful technique that give an access to the elastic constants $\bar{B}$ and K. As already mentionned, it requires very well oriented samples. Since a good homeotropic alignment is impossible to achieve with the system SDS/octanol/water/PEG, a possible way of study could consist in investigating the elastic compression modulus of spherulites [67, 68, 69]. Spherulites of controlled size can be obtained by shearing [28]. These investigations would provide precious informations on the elasticity of the lamellar mesophases, and eventually confirm the expected vanishing of $\bar{B}$ on the approach of P_{s2}. Secondly, structural investigations of the lamellar mesophases with X-rays scattering would provide complementary information. Diffuse scattering is expected on the approach of the critical point, and may even show up "before". Indeed, it would not be surprising to evidence some structural defects in the lamellar mesophases that exhibit the avalanches phenomena. These defects, if they exist, might strengthen the membranes by connecting neighbouring membranes (topological handles could be a possibility) and thus account for the difficulty to nucleate a dislocation loop. To lead such investigations, this technique also requires oriented samples. To bypass this problem, we have tried to perform measurements probing very small volumes of sample in a capillary thanks to a microfocus beam, in the Institute. By scanning along the capillary, we hoped to meet oriented microcrystals. But this procedure requires very long exposure times since the flux of the microfocus beam is weak. So the powerful synchrotron radiation would be of great help to complete successfully this study.

Polymer-doped lamellar phases are interesting objects of study, for fundamental issues as well as for practical applications. Inserting a polymer in a lamellar mesophase may induce modifications that can be "minor", like the thinning of the membranes, or

"major", like the destabilizing of the stack which leads to the coexistence of two lamellar phases of different periodicities. The reasons of these destabilizing effects are not fully understood and thus continue to interest the community. Lamellar mesophases offer also the possibility to confine polymer coils; and depending on the interactions between the polymer and the membranes, to modify the conformation of the chains near the interfaces. These studies are often the starting point of a more general one, which may concern the development of biomaterials for instance. From a practical point of view, confining macromolecules in 2-dimensional matrixes is exciting for the development of ultra-resistant and light materials of particular interest for aeronautics.

Bibliography

[1] www.brocku.ca/researchers/peter rand/osmotic/osfile.html.

[2] Y. Almog and J. Klein, *Interactions between mica surfaces in a polystyrene-cyclopentane solution near the theta-temperature*, Journal of Colloid and Interface Science, 106 (1985), pp. 33–44.

[3] D. Antelmi and P. Kékicheff, *Measurement of the compressibility modulus in a lyotropic lamellar phase stabilized by undulation forces*, Journal of Physical Chemistry B, 101 (1997), pp. 8169–8170.

[4] J. P. Arlie, PhD thesis, Université de Strasbourg, 1965.

[5] K. Arnold, A. Herrmann, L. Pratsch, and K. Gawrisch, *The dielectric properties of aqueous solutions of poly(ethylene glycol) and their influence on membrane structure*, Biochimica et Biophysica Acta, 815 (1985), pp. 515–518.

[6] F. Auguste, *Flexibilité et structure de deux phases lyotropes: phase lamellaire et phase de vésicules*, PhD thesis, Université de Bordeaux I, 1993.

[7] S. Barhoum and A. Yethiraj, *An NMR study of macromolecular aggregation in a model polymer-surfactant solution*, Journal of Chemical Physics, 132 (2010), pp. 1–9.

[8] G. Bouglet, *Confinement d'un polymère dans une phase lamellaire lyotrope: comportements de phase et constantes élastiques*, PhD thesis, Université de Montpellier, 1997.

[9] G. Bouglet and C. Ligoure, *Polymer-mediated interactions of fluid membranes in a lyotropic lamellar phase: a small-angle X-ray and neutron scattering study*, European Physical Journal E: Soft Matter, 9 (1999), pp. 137–147.

[10] G. Bouglet, C. Ligoure, A.-M. Bellocq, E. Dufourc, and G. Mosser, *Bending moduli of a nonadsorbing-polymer-containing lyotropic lamellar phase: An experimental study*, Physical Review E: Statistical, Nonlinear, and Soft Matter Physics, 57 (1998), pp. 834–842.

[11] J. T. Brooks and M. E. Cates, *The role of added polymer in dilute lamellar surfactant phases*, Journal of Chemical Physics, 99 (1993), pp. 5467–5480.

[12] J. T. Brooks, C. M. Marques, and M. E. Cates, *The effect of adsorbed polymer on the elastic moduli of surfactant bilayers*, Journal de Physique II France, 1 (1991), pp. 673–690.

[13] ——, *Role of adsorbed polymer in bilayer elasticity*, Europhysics Letters, 14 (1991), pp. 713–718.

[14] B. Cabane, *Structure of some polymer-detergent aggregates in water*, The Journal of Physical Chemistry, 81 (1977), pp. 1639–1645.

[15] B. Cabane and R. Duplessix, *Organization of surfactant micelles adsorbed on a polymer molecule in water: a neutron scattering study*, Journal de Physique France, 43 (1982), pp. 1529–1542.

[16] F. Castro-Roman, *Phase smectique de membranes fluides décorées par des copolymères amphiphiles*, PhD thesis, Université de Montpellier, 1999.

[17] F. Castro-Roman, G. Porte, and C. Ligoure, *Renormalization of helfrich's interactions between fluid membranes in a lyotropic lamellar phase by addition of amphiphilic copolymers*, Physical Review Letters, 82 (1999), pp. 109–112.

[18] F. Clement and J.-F. Joanny, *Curvature elasticity of an adsorbed polymer layer*, Journal de Physique II France, 7 (1997), pp. 973–980.

[19] J. A. Cohen, R. Podgornik, P. L. Hansen, and V. A. Parsegian, *A phenomenological one-parameter equation of state for osmotic pressures of peg and other neutral flexible polymers in good solvents*, Journal of Physical Chemistry B, 113 (2009), pp. 3709–3714.

[20] A. C. Cowley, N. L. Fuller, R. P. Rand, and V. A. Parsegian, *Measurement of repulsive forces between charged phospholipid bilayers*, Biochemistry, 17 (1978), pp. 3162–3168.

[21] O. A. Croze and M. E. Cates, *Nonadditivity of polymeric and charged surface interactions: Consequences for dopped lamellar phases*, Langmuir, 21 (2005), pp. 5627–5638.

[22] M. Daoud and P.-G. de Gennes, *Statistics of macromolecular solutions trapped in small pores*, Journal de Physique France, 38 (1977), pp. 85–93.

[23] P.-G. de Gennes, *The Physics of Liquid Crystals*, Clarendon Press Oxford, 1974.

[24] ——, *Polymer solutions near an interface. 1. adsorption and depletion layers*, Macromolecules, 14 (1981), pp. 1637–1644.

[25] ——, *Interactions between polymers and surfactants*, Journal of Physical Chemistry, 94 (1990), pp. 8407–8413.

[26] P.-G. de Gennes and J. Prost, *The Physics of Liquid Crystals*, Clarendon Press, Oxford, 1993.

[27] B. V. Derjaguin, *Theorie des anhaftens kleiner teilchen*, Kolloid Z., 69 (1934), pp. 155–164.

[28] O. Diat and D. Roux, *Preparation of monodisperse multilayer vesicles of controlled size and high encapsulation ratio*, Journal de Physique II France, 3 (1993), pp. 9–14.

[29] O. Diat, D. Roux, and F. Nallet, *Effect of shear on a lyotropic lamellar mesophase*, Journal de Physique II France, 3 (1993), pp. 1427–1452.

[30] M. Dubois, T. Zemb, and L. Belloni, *Osmotic pressure and salt exclusion in electrostatically swollen lamellar phases*, Journal of Chemical Physics, 96 (1992), pp. 2278–2286.

[31] E. Eisenriegler, *Universal amplitude ratios for the surface tension of polymer solutions*, Journal of Chemical Physics, 81 (1984), pp. 4666–4675.

[32] E. Evans and D. Needham, *Attraction between lipid bilayer-membranes in concentrated solutions of non-adsorbing polymer - comparison of mean-fiel theory with measurements of adhesion energy*, Macromolecules, 21 (1988), pp. 1822–1831.

[33] M.-F. Ficheux, *Etude de systèmes mixtes polymère/tensioactif en phases organisées: diagrammes de phases et interactions*, PhD thesis, Université Bordeaux I, 1995.

[34] M.-F. Ficheux, A.-M. Bellocq, and F. Nallet, *Experimental study of a lyotropic lamellar phase swollen with polymer solutions*, Journal de Physique II France, 5 (1995), pp. 823–834.

[35] ——, *Elastic properties of polymer-doped dilute lamellar pphase: A small-angle neutron scattering study*, European Physical Journal E: Soft Matter, 4 (2001), pp. 315–326.

[36] M.-F. Ficheux, T. Riley, A.-M. Bellocq, and F. Nallet, *Solubilization of an adsorbing polymer in a lyotropic lamellar phase: effect of polymer molecular weight*, Editions Frontières, 1995.

[37] C. C. Fleck and R. R. Netz, *Surfaces with quenched and annealed disordered charge distributions*, European Physical Journal E, 22 (2007), pp. 261–273.

[38] C. C. Fleck, R. R. Netz, and H. H. von Grnberg, *Poisson-boltzmann theory for membranes with mobile charged lipids and the ph-dependent interaction of a dna molecule with a membrane*, Biophysical Journal, 82 (2002), pp. 76–92.

[39] E. Freyssingeas, *Diffusion du rayonnement par des phases de membranes: phases lamellaires, phases éponges*, PhD thesis, Université Bordeaux I, 1994.

[40] E. Freyssingeas, D. Antelmi, P. Kékicheff, P. Richetti, and A.-M. Bellocq, *Softening of the interactions between surfactant bilayers in a lamellar phase due to the presence of a polymer*, European Physical Journal B, 9 (1999), pp. 123–136.

[41] E. Freyssingeas, A. Martin, and D. Roux, *Role of dislocation loops on the elastic constants of lyotropic lamellar phases*, The European Physical Journal E, 18 (2005), pp. 219–230.

[42] J. C. Froberg and T. Ederth, *On the possibility of glue contaminations in the surface force apparatus*, Journal of Colloid and Interface Science, 210 (1999), pp. 215–217.

[43] J.-C. Géminard, R. Holyst, and P. Oswald, Physical Review Letters, 78 (1994), p. 1924.

[44] B. Hammouda, *Probing Nanoscale Structures - the SANS Toolbox. Chapter 37 - SANS from polymer solutions.*

[45] P. L. Hansen, J. A. Cohen, R. Podgornik, and V. A. Parsegian, *Osmotic properties of poly(ethylene glycols): Quantitative features of brush and bulk scaling laws*, Biophysical Journal, 84 (2003), pp. 350–355.

[46] W. Helfrich, Naturforsch, 28c (1973), p. 693.

[47] ——, Naturforsch, 28c (1978), p. 305.

[48] C. A. Helm, J. N. Israelachvili, and P. M. McGuiggan, *Role of hydrophobic forces in bilayer adhesion and fusion*, Biochemistry, 31 (1992), pp. 1794–1805.

[49] R. A. Herke, N. A. Clark, and M. A. Handschy, *Stress-induced vortex line helixing avalanches in the plastic flow of a smectic a liquid crystal*, Science, 267 (1995), pp. 651–654.

[50] ——, *Dynamic behavior of oscillatory plastic flow in a smectic liquid crystal*, Physical Review E: Statistical, Nonlinear, and Soft Matter Physics, 56 (1997), pp. 3028–3043.

[51] J. N. Israelachvili, *Thin films studies using multiple-beam interferometry*, Journal of Colloid and Interface Science, 44 (1973), pp. 259–272.

[52] ——, *Measurement of forces between surfaces immersed in elctrolyte solutions*, Faraday Discussions, 65 (1978), pp. 20–24.

[53] ——, *Intermolecular and Surface Forces*, Academic Press, second ed., 1991.

[54] J. N. Israelachvili and G. E. Adams, *Measurement of forces between two mica surfaces in aqueous electrolyte solutions in the range 0-100 μm*, Journal of the Chemical Society - Faraday Trans. 1, 74 (1978), pp. 975–1001.

[55] W. Janke, H. Kleinert, and M. Meinhart, *Monte carlo study of a stack of self-avoiding surfaces with extrinsic curvature stiffness*, Physics Letters B, 217 (1989), pp. 525–529.

[56] I. Javierre, *Polymère confiné en phases de membranes: influences sur la stabilité, la structure et la dynamique*, PhD thesis, Université Bordeaux I, 1999.

[57] I. Javierre, A.-M. Bellocq, and F. Nallet, *Effect of confinement of a polymer on the phase behavior of ternary and quaternary lyotropic mixtures*, Langmuir, 17 (2001), pp. 5417–5425.

[58] P. Kékicheff, *Electrostatic Effects in Soft Matter and Biophysics*, C. Holm and P. Kékicheff and R. Podgornik, Eds., Kluwer Academic Publishers, Dordrecht, The Netherlands 2001, vol. 46, p. 205-282.

[59] P. Kékicheff, *Unpublished results; private communication.*

[60] P. Kékicheff, B. Cabane, and M. Rawiso, *Macromolecules dissolved in a lamellar lyotropic mesophase*, Journal of Colloid and Interface Science, 102 (1984), pp. 51–70.

[61] P. Kékicheff and H. K. Christenson, *Forces measured in a swollen lyotropic lamellar mesophase confined between solid surfaces*, Physical Review Letters, 63 (1989), pp. 2823–2826.

[62] P. Kékicheff, C. Grabielle-Madelmont, and M. Ollivon, *Phase diagram of sodium dodecyl sulfate-water system*, Journal of Colloid and Interface Science, 131 (1989), pp. 112–132.

[63] P. Kékicheff, P. Richetti, and H. K. Christenson, *Structure and elastic properties of lamellar mesophases from direct force measurements*, Langmuir, 7 (1991), pp. 1874–1879.

[64] M. Kléman, *Points, Lines and Walls: in Liquid Crystals, Magnetic Systems, and Various Ordered Media*, Wiley, New-York, 1983.

[65] J. L. Kurz, Journal of Physical Chemistry, 66 (1962), p. 2239.

[66] F. Lachampt and R. M. Vila, *Textures des phases paracristallines rencontrées dans les diagrammes d'équilibre: agents de surface, lilipid, eau*, Revue Francaise des Corps Gras, 16 (1969), pp. 87–111.

[67] J. Leng, *Structure et dynamique de la texture ognon des phases lamellaires lyotropes*, PhD thesis, Université Bordeaux I, 1999.

[68] J. Leng, F. Nallet, and D. Roux, *Anomalous elasticity of an ordered lamellar liquid foam*, European Physical Journal E, 4 (2001), pp. 337–341.

[69] ——, *Swelling kinetics of a compressed lamellar phase*, Eurpean Physical Journal E, 4 (2001), pp. 77–83.

[70] C. Ligoure, G. Bouglet, and G. Porte, *Polymer induced phase separation in lyotropic smectics*, Physical Review Letters, 71 (1993), pp. 3600–3603.

[71] C. Ligoure, G. Bouglet, G. Porte, and O. Diat, *Smectic compressibility of polymer-containing lyotropic lamellar phases: An experimental tool to study the thermodynamics of polymer confinement*, Journal de Physique II France, 7 (1997), pp. 473–491.

[72] A. G. Moreira and R. R. Netz, *Simulations of counterions at charged plates*, European Physical Journal E: Soft Matter, 8 (2002), pp. 33–58.

[73] M. Muramatsu and M. Inoue, Journal of Colloid and Interface Science, 55 (1976), p. 80.

[74] F. Nallet and J. Prost, *Edge dislocation arrays in swollen lamellar phases*, Europhysics Letters, 4 (1987), pp. 307–313.

[75] F. Nallet., D. Roux, and J. Prost, *Hydrodynamics of lyotropic smectics: a dynamic light scattering study of dilute lamellar phases*, Journal de Physique II France, 50 (1989), pp. 3147–3165.

[76] F. Nallet, D. Roux, C. Quilliet, P. Fabre, and S. T. Milner, *Elasticity and hydrodynamic properties of "doped solvent" dilute lamellar phases*, Journal de Physique II France, 4 (1994), pp. 1477–1499.

[77] P. Oswald and P. Pieranski, *Les cristaux liquides - Concepts et propriétés physiques illustrés par des expériences (tome 2)*, GB Science Publishers, 2002.

[78] P. S. Pershan, Journal of Applied Physics, 45 (1974), p. 1590.

[79] L. Porcar, *Incorporation de Polymères Organiques ou Inorganiques dans une phase lamellaire lyotrope: Structures et Comportements de Phases*, PhD thesis, Université Montpellier II, 1997.

[80] L. Porcar, C. Ligoure, and J. Marignan, *Layer compression modulus of electrostatically stabilized lyotropic lamellar phases revisited: Application to the quantitative analysis of a polymer induced critical sma-sma phase separation*, Journal de Physique II France, 7 (1997), pp. 493–501.

[81] L. Porcar, J. Marignan, and C. Ligoure, *Effect of a nonadsorbing polymer on the stability of a two-solvent lamellar phase: Experimental and theoretical study of critical points of lamellar/lamellar phase separations*, Langmuir, 16 (2000), pp. 2581–2594.

[82] G. Porte, J. Appell, P. Bassereau, and J. Marignan, *L_α to L_3: a topology driven transition in phases of infinite fluid membranes*, Journal de Physique France, 50 (1989), pp. 1335–1347.

[83] P. Richetti, P. Kékicheff, and P. Barois, *Measurement of the layer compressibility modulus of a lamellar mesophase with a surface force apparatus*, Journal de Physique II France, 5 (1995), pp. 1129–1154.

[84] P. Richetti, P. Kékicheff, J. L. Parker, and B. W. Ninham, *Measurement of the interactions between membranes in a stack*, Nature, 346 (1990), pp. 252–254.

[85] D. Roux, F. Nallet, and O. Diat, *Rheology of lyotropic lamellar phases*, Europhysics Letters, 24 (1993), pp. 53–58.

[86] D. Roux and C. R. Safinya, *A synchrotron X-ray study of competing undulation and electrostatic interlayer interactions in fluid multimembrane lyotropic phases*, Journal de Physique France, 49 (1988), pp. 307–318.

[87] A. N. Semenov, J.-F. Joanny, and A. Johner, *Theoretical and Mathematical Models in Polymer Research - Modern Methods in Research and Technology - Chapter 2*, Academic Press, 1998.

[88] A. N. Semenov, J.-F. Joanny, A. Johner, and J. Bonet-Avalos, *Interactions between two adsorbing plates: The effect of polymer chain ends*, Macromolecules, 30 (1997), pp. 1479–1489.

[89] S. Tolansky, *Multiple-beam interferometry of surfaces and films*, Clarendon Press, 1948.

Laure HERRMANN

Polymères confinés dans des mésophases lamellaires lyotropes

Ce travail porte sur l'étude de mésophases lamellaires lyotropes qui contiennent des polymères hydrosolubles confinés dans les lamelles d'eau de l'empilement. L'effet du polymère confiné sur la stabilité de la structure lamellaire est en particulier étudié grâce à une mesure directe des interactions entre les membranes de tensioactif grâce la technique du Surface Force Apparatus (SFA). Les systèmes étudiés sont des fluides complexes et très visqueux ce qui a donné lieu au développement d'une nouvelle méthode pour analyser les données collectées. En l'absence de polymère dissous dans l'empilement lamellaire, la valeur du module de compressibilité élastique mesurée est remarquablement interprétée avec la théorie électrostatique corrigée des corrélations des contre-ions. En présence de polymère, au fur et à mesure que les macromolécules remplacent le contenu en eau, le module élastique de compressibilité de l'empilement lamellaire chute, signature d'une interaction attractive due à la présence des macromolécules. Néanmoins, les développements théoriques proposés ne parviennent pas à interpréter quantitativement cette décroissance. De plus, des comportements très intéressants et inattendus ont été mis en évidence lors de l'approche d'un point critique : la présence de dislocations de très grands vecteurs de Burgers à grande séparation ainsi que des phénomènes d'avalanches. En particulier, des énergies de nucléation de dislocation ont pu être extraites.

Mots clés : phases lamellaires – interactions intermembranaires – interaction électrostatique – dislocation – énergie de nucléation – vecteur de Burgers - polymères

Polymers confined in lyotropic lamellar mesophases

This work deals with lyotropic lamellar mesophases which contain confined hydrosoluble polymers in the water layers of the stack. In particular the effect of confined polymers on the stability of the lamellar structure is investigated through a direct measurement of the interactions between the surfactant membranes thanks to the Surface Force Apparatus (SFA) technique. The investigated systems are complex fluids and samples are extremely viscous, this is why a new procedure for analyzing the collected data has been developed. In the absence of dissolved polymer in the lamellar stack, the measured value of the elastic compressibility modulus is remarkably interpreted with the electrostatic interaction corrected from the counterions correlations. In the presence of polymer, as long as the macromolecules replace the water content the elastic compressibility modulus of the lamellar stack decreases, evidencing an attractive interaction due to the macromolecules. Nevertheless, the proposed theoretical developments fail to quantitatively interpret this drop. Moreover, very interesting and unexpected phenomena have been evidenced on the approach of one critical point: dislocations of large Burgers vectors at large separations and avalanche phenomena. In particular dislocation nucleation energies have been extracted.

Keywords: lamellar phases – intermembrane interactions – electrostatic interaction – dislocation – nucleation energy – Burgers vector - polymers